DISSERTATION

MAGNETIC IMAGING OF FLUXOID BEHAVIOR IN SUPERCONDUCTORS AND SPIN-POLARIZATION EFFECTS IN CHIRAL MATERIALS

Submitted by
Evan Folk
Department of Physics

In partial fulfillment of the requirements
For the Degree of Doctor of Philosophy
Colorado State University
Fort Collins, Colorado
Fall 2025

Doctoral Committee:

Advisor: Stuart Field

Martin Gelfand
Kristen Buchanan
Justin Sambur

ABSTRACT

MAGNETIC IMAGING OF FLUXOID BEHAVIOR IN SUPERCONDUCTORS AND SPIN-POLARIZATION EFFECTS IN CHIRAL MATERIALS

This dissertation details the utilization of a custom-built scanning Hall-probe microscopy system to image a range of superconducting and magnetic phenomena. Our system offers approximately 1 μm^2 spatial and 10 mG field resolution (depending greatly on the conditions of the scan), serving as a powerful tool for measuring local magnetic fields. This section provides an extensive overview of scanning Hall-probe microscopy; Hall-probe fabrication; and the scanning, positioning, and cryogenic systems.

Much of the work presented will focus on imaging magnetic signatures of exotic superconductivity. An introduction to superconductivity will be presented as necessary background to understand the systems described in later chapters. We will start with the most well-known characteristics such as the transition to zero resistance and the Meissner effect, introduce various theoretical descriptions, and eventually delve into the subtle properties that underlie unconventional superconductivity. A point of emphasis will be the behavior of superconducting vortices—material-penetrating magnetic fibers circulated by supercurrent. The importance of London's fluxoid and its quantization will be discussed at length.

An imaging study of a thin-film type II superconducting ring will be presented, focusing on the evolution of fluxoids in applied magnetic field along the axis of the ring. The interplay between fluxoids hosted in the ring's geometrical hole, and those associated with nucleated superconducting vortices in the bulk of the ring will be examined using complementary techniques. A theoretical and numerical project aimed at understanding and predicting the equilibrium behavior of this system will be presented. This experiment serves as a basis for later imaging studies of exotic fluxoid quantization conditions.

Superconducting vortices capable of supporting half-quantized fluxoids (HQFs) hold promise in topological quantum computing in addition to fundamental scientific interest. HQFs have been experimentally verified in geometric holes, however those associated with superconducting vortices (HQVs) have not been observed. Certain type II superconductors with spin-triplet electron pairing have been theorized to host vortices with HQFs. Our work on detecting HQVs in one such material will be detailed.

The chirality-induced spin-selectivity effect is a property of certain chiral materials that exhibit a spin-dependent resistance along their chiral axis, leading to spin-filtering. These materials have garnered interest in the spintronics community as a platform for manipulating spin without the need for an external magnetic field or cryogenic temperatures. A novel CISS detection method and preliminary experimental results will be presented. A proposal for a device geometry that allows for more sensitive detection will be discussed.

ACKNOWLEDGEMENTS

My doctoral studies were marked by struggles that extended well beyond the classroom and lab and I am eternally grateful for the support system that guided me. Particularly my parents Terry and Maria, my sister Emily, and my wife Demi. Mom and dad, you're the best parents a person could ask for and you've given a great example for how to raise a family. You're the most thoughtful, collected, and loving people that I know. You're the first place I look when I need comfort, encouragement, or advice. My biggest goal continues to be following in your footsteps. Emily, you're an amazing big sister. I cherish our relationship and look up to you more than you know. I love you and your family and look forward to more time spent together. Demi, words can't express what you mean to me and what you've done for me. There's no one I'd rather wander through life with and I can't wait for what lies ahead. This achievement is as much ours as it is mine.

I'd also like to recognize the mentors I've had throughout my education. Especially Stuart Field, whose professional and personal guidance will be carried with me for the rest of my life. I was Stuart's only student for five years which led to a great opportunity to learn from him as well develop a cheerful and friendly working relationship. Additionally I want to thank August DeMann and Weston Maughan for their patience and generosity in sharing lab knowledge. They played a huge role into developing me into someone who can turn a wrench. I also want to mention the brilliant Jennifer Jones, power couple Kesston and Kendra Fink, Robert Price, and Katherine Kime.

I want to acknowledge my grad school cohort with a special shout out to my friends Andrew, Lane, Back Out Byron, Tarky (no malarkey), John, Brutus, and Big Tex. I cherish the memories of ripping lips, skiing, backpacking, the party office, and horse racing. Time spent in the lab and classroom should be balanced with time spent being stupid—there was no shortage of either.

Lastly, a big thank you to my closest friends Seth, Brad, Jackson, Pat, Jake, and Luke. GGs my brothers, I've loved our adventures and nightly escape of firing up discord. To a lifetime of friendship.

DEDICATION

To Demi, the source of my joy

TABLE OF CONTENTS

LIST OF TABLES

LIST OF FIGURES

Chapter 1

Introduction to Superconductivity

"Things don't turn up in this world until

somebody turns them up."

—Frank Lloyd Wright

1.1 Origins

The inception of superconductivity lies in the early 1900s efforts of Kamerlingh Onnes to probe the low-temperature properties of metals. At the time, there was a debate concerning the conductivity of metals as their temperature approached absolute zero. Lord Kelvin thought that electrons would be "frozen" in place, leading to an infinite resistivity, while Drude believed that conductivity should increase as the temperature decreases, tending toward perfect conductivity [9]. In 1906, Onnes characterized the resistivity of thin gold and platinum wires and found that the linear decrease in resistance with decreasing temperature flattened at very low temperatures [10]. He noted a supposed minimum resistivity, consistent with Kelvin's theory [9].

In 1906 the lowest achievable cryogenic temperature was 14 K using liquefied hydrogen. This temperature threshold was overcome in 1908 as Onnes utilized the Hampson–Linde cycle and became the first to liquefy helium, a remarkable feat since helium had only recently been discovered on Earth in American mines in the 1890s [11]. This breakthrough gave access to 4.2 K at standard pressure or 1.5 K after lowering the pressure of the helium. Onnes investigated the electrical properties of metals in this ultra-low temperature regime. He measured the resistivity of various materials—lead, mercury, tin, etc.—submerged in a bath of liquid helium. Interestingly, it was found that the resistance of mercury abruptly fell to zero (see Fig. 1.1) at 4.2 K.

Although Onnes believed that the metals would behave as perfect conductors at absolute zero, this stark change at a few kelvins was a surprise. This behavior indicated a new state of matter,

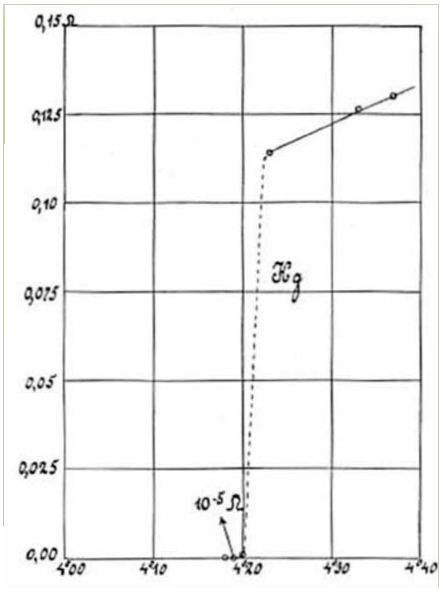

Figure 1.1: Original plot reproduced from Onnes' 1911 publication demonstrating the disappearance of mercury's electrical resistance at low temperature [1]. Notably, there is a sharp drop to zero resistance at 4.2 K.

superconductivity , described at the time as an abrupt change to perfect conductivity below a material-specific critical temperature T_c. Onnes' liquefication of helium and subsequent experimentation on the low-temperature characteristics of metals were rewarded with a Nobel prize in 1913.

1.2 Meissner Effect

From 1908 to 1933 the superconducting state was entirely described by a drop to zero resistance upon cooling through a material's critical temperature. In 1933, Meissner and Oschenfeld studied the response of the superconducting state to applied magnetic fields [12]. They first cooled a metal through T_c in the absence of a magnetic field. Below T_c, an external field was applied and this field was screened from the interior of the superconductor, as is predicted by applying Lenz's law to a perfect conductor. In a subsequent experiment, however, it was unexpectedly found that a metal cooled through T_c in a static magnetic field expelled that applied field as it transitioned into the superconducting state (see Fig. 1.2) [13]. This demonstrated that superconductors are not only perfect conductors, they are *perfect diamagnets*. This behavior was termed the *Meissner*

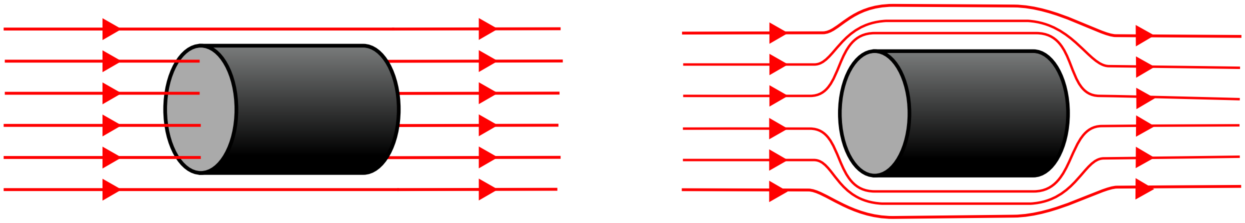
(a) Above critical temperature (b) Below critical temperature

Figure 1.2: A superconducting cylinder in the presence of an applied magnetic field (red lines). In (a) $T > T_\mathrm{c}$, the applied field is uniformly penetrating the sample. In (b) $T < T_\mathrm{c}$, screening currents are generated on the exterior of the superconductor, expelling the applied field from its interior.

Effect [14]. The Meissner Effect, along with the sharp drop to zero resistance, are the hallmarks of conventional superconductivity.

1.3 London Theory

The first major development in the theoretical description of superconductivity came in the form of a phenomenological theory published by brothers Fritz and Heinz London in 1935 [15] and further developed by Fritz London [16]. This theory introduced a set of equations that described the macroscopic electric and magnetic fields of superconductors. Additionally, their work led to a parameter that is useful in classifying superconductors. The London equations are

$$\mathbf{E} = \frac{\partial}{\partial t}\Lambda \mathbf{J}_\mathrm{s} \tag{1.1}$$

$$\mathbf{h} = \boldsymbol{\nabla} \times (\Lambda \mathbf{J}_\mathrm{s}), \tag{1.2}$$

where $\Lambda = 4\pi\lambda^2/c^2 = m/n_\mathrm{s}e^2$. Here, $\mathbf{E}$ is the electric field, $\mathbf{J}_\mathrm{s}$ is the supercurrent density, $\mathbf{h}$ is the magnetic field, λ is a material-specific length scale soon to be introduced, n_s is the number density of superconducting electrons, and m is the mass of an electron. The first equation is consistent with perfect conductivity, as it implies that electric fields cause accelerating currents. The second equation shows that magnetic fields generate superconducting currents—a reversal of our classical view of magnetism.

Combining Eq. 1.2 with Ampere's law and appealing to a vector identity reveals a particularly interesting relationship. Maxwell demonstrated that [17]

$$\boldsymbol{\nabla} \times \mathbf{h} = \frac{4\pi \mathbf{J}}{c}. \tag{1.3}$$

Taking the curl of both sides gives

$$\boldsymbol{\nabla} \times (\boldsymbol{\nabla} \times \mathbf{h}) = \boldsymbol{\nabla} \times \frac{4\pi \mathbf{J}}{c} = \frac{4\pi}{c} (\boldsymbol{\nabla} \times \mathbf{J}).$$

Applying a vector identity to the left side and substituting Eq. 1.2 on the right side,

$$\boldsymbol{\nabla} \cdot (\boldsymbol{\nabla} \cdot \mathbf{h}) - \nabla^2 \mathbf{h} = \frac{4\pi}{c} \left(\frac{-\mathbf{h}}{c\Lambda} \right).$$

Another of Maxwell's Laws states that $\boldsymbol{\nabla} \cdot \mathbf{h} = 0$ leaving us with

$$\nabla^2 \mathbf{h} = \frac{4\pi}{c^2 \Lambda} \mathbf{h}.$$

Finally, substituting the definition of Λ yields a powerful result,

$$\nabla^2 \mathbf{h} = \frac{\mathbf{h}}{\lambda^2}. \tag{1.4}$$

This relationship gives a theoretical description of the Meissner effect and indicates an exponential screening of magnetic fields with characteristic length scale λ (see Fig. 1.3). This is the *penetration depth* and describes the depth for which an applied magnetic field penetrates a superconductor. London's penetration depth λ_{L} has temperature dependence and is well-approximated by [18]

$$\lambda_{\mathrm{L}}(T) \approx \frac{\lambda_{\mathrm{L}}(0)}{\left[1 - (T/T_{\mathrm{c}})^4\right]^{1/2}}.$$

Typical values for London's penetration depth are 20 – 100 nm for elemental superconductors.

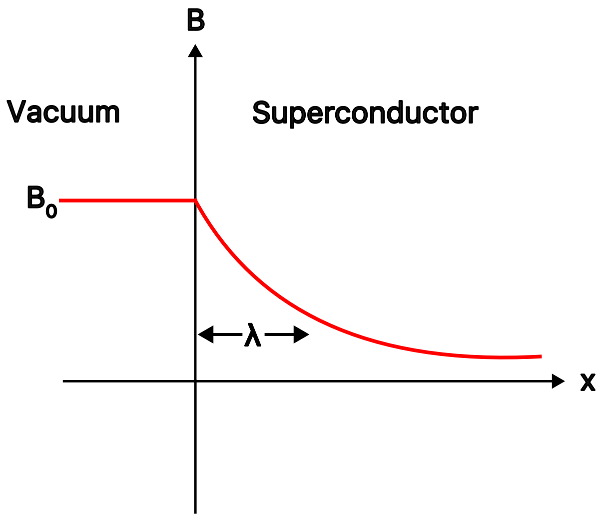

Figure 1.3: The magnetic field (red) drops off exponentially with characteristic length λ in the interior of the superconductor. The two regions, vacuum and superconductor, are separated by the vertical axis. Here, x represents the depth into the superconductor.

1.4 Pippard's Coherence Length

Chambers defined a nonlocalized extension of Ohm's law [19,20], ($\mathbf{J}(\mathbf{r}) = \sigma \mathbf{E}(\mathbf{r})$), as

$$\mathbf{J}(\mathbf{r}) = \frac{3\sigma}{4\pi l} \int \frac{\mathbf{R}\left[\mathbf{R} \cdot \mathbf{E}\left(\mathbf{r}'\right)\right] e^{-R/l}}{R^4} d\mathbf{r}', \tag{1.5}$$

where $\mathbf{r}$ is the field point, $\mathbf{r}'$ is the source point, $\mathbf{R} = \mathbf{r} - \mathbf{r}'$ is the displacement vector, and l is the mean free path of an electron. Chambers argued that the current density at some point $\mathbf{r}$ depends on the electric field within a spherical volume of radius l about $\mathbf{r}$ [19,20]. Analogously, Pippard posited that only certain electrons can take part in a process that occurs at temperature T_c [14,21]. That is, only electrons approximately within kT_c of the Fermi energy participate in superconductivity. These electrons have a momentum range $\Delta p \approx kT_c/v_F$, where v_F is the Fermi velocity. Δp can be derived by considering the relationship between energy, momentum, and velocity. Applying this momentum range to Heisenberg's uncertainty principle yields

$$\Delta x \geq \hbar/\Delta p \approx \hbar v_F/kT_c$$

which defines a characteristic length, *Pippard's coherence length*, $\xi_0 = a\hbar v_\mathrm{F}/kT_\mathrm{c}$ where $a \sim 1$. For conventional superconductors $\xi_0 \gg \lambda_\mathrm{L}(0)$.

This led to a nonlocalized expression for current density that is clearly analogous to Eq. 1.5, with ξ_0 taking the place of l:

$$\mathbf{J}_\mathrm{s}(\mathbf{r}) = -\frac{3}{4\pi\xi_0\Lambda c}\int \frac{\mathbf{R}\left[\mathbf{R}\cdot\mathbf{A}\left(\mathbf{r}'\right)\right]e^{-R/\xi}}{R^4}d\mathbf{r}'. \tag{1.6}$$

Here $1/\xi = 1/\xi_0 + 1/l$. Pippard's coherence length, ξ_0, will show up as a limiting value of a new coherence length to be defined in the following section. After carefully choosing a, Pippard's theory successfully fit data on aluminum and tin [22], lending credence to this nonlocalized approach.

1.5 Ginzburg and Landau

1.5.1 Energy Considerations and Critical Field

The work of Meissner and Oschenfeld inspired consideration of the energetics underlying the superconducting state. These materials naturally superconduct below T_c, so the superconducting state must be energetically favorable. However, maintaining this state in the presence of an applied field has an energetic cost associated with setting up screening currents.

The *condensation energy* is the difference in free energy between the normal state $F_\mathrm{n}(T)$ and the superconducting state $F_\mathrm{s}(T)$ at a given temperature in zero field [23]. As the magnitude of the applied field increases, so does the energy needed to expel that field. This points to the existence of a *critical field* H_c, at which the condensation energy goes to zero and superconductivity is destroyed. That is, at H_c it becomes energetically favorable to allow the applied field to penetrate the material, terminating the superconducting state. To formalize this idea, consider the Helmholtz free energy densities of the normal and superconducting states f_n, f_s, in zero field and how they relate to the energy density associated with screening the applied field ($H_\mathrm{c}^2/8\pi$). If the screening energy density exceeds the condensation energy density ($f_\mathrm{n} - f_\mathrm{s}$), superconductivity is destroyed. Thus, to find H_c, we simply set the energy per unit volume of the screening field equal to the condensation energy density [14]

$$\frac{H_{\rm c}(T)^2}{8\pi} = f_{\rm n}(T) - f_{\rm s}(T).$$

It has been found empirically that $H_{\rm c}(T) \approx H_{\rm c}(0)[1 - (\frac{T}{T_{\rm c}})^2]$; thus the critical field decreases quadratically with T and reaches zero at $T_{\rm c}$ [24].

1.5.2 The Ginzburg-Landau Theory

The Ginzburg-Landau (GL) theory is a phenomenological framework that describes a superconductor's behavior near its critical temperature. It introduces a complex function ψ, called the *order parameter*, which is analogous to the wavefunction used in quantum mechanics. It can be used to find the probability density of superconducting electrons through the relationship $n_{\rm s} = |\psi^2|$. The order parameter can be expressed in polar form as

$$\psi(\vec{r}) = |\psi(\vec{r})| e^{i\phi(\vec{r})}, \tag{1.7}$$

where ϕ is the superconducting phase. It's worth noting that $|\psi(\vec{r})|$ is also written as $\Delta(\mathbf{r})$, and that formalism will be used in our later discussion of London's fluxoid. Ginzburg and Landau postulated that for small ψ that varies slowly in space, the free energy can be expanded as

$$f = f_{n0} + \alpha|\psi|^2 + \frac{\beta}{2}|\psi|^4 + \frac{1}{2m}\left|\left(\frac{\hbar}{i}\boldsymbol{\nabla} - \frac{e^*}{c}\mathbf{A}\right)\psi\right|^2 + \frac{h^2}{8\pi}.$$

Here, f_{n0} is the free energy of the normal state, m^* is the effective mass of a supercurrent carrier, e^* is the effective charge of a supercurrent carrier, α and β are phenomenological parameters, and $\mathbf{A}$ is the magnetic vector potential [23]. Minimizing this free energy with respect to ψ and A leads to the fundamental differential equations of the theory:

$$-\alpha(T) = \frac{1}{2m}\left(\frac{\hbar}{i}\boldsymbol{\nabla} - \frac{e^*}{c}\mathbf{A}\right)^2 \psi + \beta|\psi|^2\psi \tag{1.8}$$

$$\vec{J}_{\rm s} = \frac{e^*\hbar}{i2m^*}(\psi^*\boldsymbol{\nabla}\psi - \psi\boldsymbol{\nabla}\psi^*) - \frac{(e^*)^2}{m^*c}|\psi|^2\mathbf{A}. \tag{1.9}$$

Eq. 1.9 will be utilized in the upcoming discussion of fluxoid quantization.

A key feature of GL theory is a new characteristic length

$$\xi(T) = \frac{\hbar}{|2m^*\alpha(T)|^{\frac{1}{2}}},$$

called the GL coherence length. This parameter describes the minimum distance over which ψ (and therefore n_s) can vary significantly. As the temperature approaches 0 K, $\xi(T) \approx \xi_0$, the Pippard coherence length. Combining this new coherence length with the previously established penetration depth from London theory, we can define the Ginzburg-Landau parameter, $\kappa = \lambda/\xi$. The significance of κ will be illuminated during the discussion of different classes of superconductors.

1.6 London's Fluxoid and Fluxoid Quantization

The *fluxoid*

$$\Phi' = \Phi + \frac{4\pi}{c} \oint \lambda^2 \mathbf{J}_s \cdot d\mathbf{s} \tag{1.10}$$

is a quantity introduced by London that includes the familiar magnetic flux ($\Phi = \iint \mathbf{h} \cdot d\boldsymbol{\sigma}$), in addition to a contribution associated with the induced supercurrent in a superconductor [16, 25]. Here, the integral is taken along a closed path entirely within the superconducting material. Let us analyze this fluxoid for two scenarios: a contour that encircles a singly connected superconductor and one that encircles a topological hole.

1.6.1 Singly connected Superconducting Material

When encircling singly connected superconductor, London's equations (specifically $\mathbf{h} = -c\boldsymbol{\nabla} \times \Lambda\mathbf{J}_s$) hold throughout the surface defined by the contour of integration so the flux term can be rewritten as

$$\Phi = \iint \mathbf{h} \cdot d\boldsymbol{\sigma} = \iint (-c\boldsymbol{\nabla} \times \Lambda\mathbf{J}_s) \cdot d\boldsymbol{\sigma}. \tag{1.11}$$

Stokes' theorem can be applied to arrive at

$$\Phi = -c\Lambda \oint \mathbf{J}_{\mathrm{s}} \cdot d\mathbf{s}. \tag{1.12}$$

Substituting this equation for flux into the definition of the fluxoid and remembering the earlier definition, $\Lambda = 4\pi\lambda^2/c^2$, yields

$$\begin{aligned}
\Phi' &= -c\Lambda \oint \mathbf{J}_{\mathrm{s}} \cdot d\mathbf{s} + \frac{4\pi}{c} \oint \lambda^2 \mathbf{J}_{\mathrm{s}} \cdot d\mathbf{s} \\
&= -c\frac{4\pi\lambda^2}{c^2} \oint \mathbf{J}_{\mathrm{s}} \cdot d\mathbf{s} + \frac{4\pi}{c}\lambda^2 \oint \mathbf{J}_{\mathrm{s}} \cdot d\mathbf{s} \\
&= -\frac{4\pi}{c}\lambda^2 \oint \mathbf{J}_{\mathrm{s}} \cdot d\mathbf{s} + \frac{4\pi}{c}\lambda^2 \oint \mathbf{J}_{\mathrm{s}} \cdot d\mathbf{s} \\
&= 0.
\end{aligned}$$

Thus, the fluxoid is zero for any contour composed entirely of superconducting material and not encircling a topological hole.

1.6.2 Encircling a Hole

If a contour encircles a hole—a geometric hole in the material or the normal core of the soon-to-be-discussed type II superconducting vortices—the behavior of the fluxoid is quite different. By applying Stokes' Theorem and invoking the definition of magnetic vector potential ($\mathbf{B} = \nabla \times \mathbf{A}$), the flux term can be rewritten as

$$\iint \mathbf{B} \cdot d\boldsymbol{\sigma} = \oint \mathbf{A} \cdot d\mathbf{s}.$$

Again, the starting point will be the definition of the fluxoid. We can use the fact that $\Lambda = 4\pi\lambda^2/c^2 = m/n_{\mathrm{s}}e^2$ and $\mathbf{J}_{\mathrm{s}} = n_{\mathrm{s}}e\mathbf{v}_{\mathrm{s}}$, to rewrite the supercurrent contribution. Here, $\mathbf{v}_{\mathrm{s}}$ is the *drift velocity*, the average velocity of a superconducting charge carrier due to the presence of an electric field. Then a common term can be pulled out to represent the fluxoid in a suggestive way,

$$\begin{aligned}
\Phi' &= \oint \mathbf{A} \cdot d\mathbf{s} + \frac{4\pi\lambda^2}{c} \oint \mathbf{J}_{\mathrm{s}} \cdot d\mathbf{s} \\
&= \oint \mathbf{A} \cdot d\mathbf{s} + \frac{m^* c}{n_{\mathrm{s}}(e^*)^2} n_{\mathrm{s}} e^* \oint \mathbf{v}_{\mathrm{s}} \cdot d\mathbf{s} \\
&= \oint \mathbf{A} \cdot d\mathbf{s} + \frac{m^* c}{e^*} \oint \mathbf{v}_{\mathrm{s}} \cdot d\mathbf{s} \\
&= \frac{c}{e^*} \oint \left(\frac{e^*}{c}\right) \mathbf{A} \cdot d\mathbf{s} + \frac{m^* c}{e^*} \oint \mathbf{v}_{\mathrm{s}} \cdot d\mathbf{s} \\
&= \frac{c}{e^*} \oint \left[m^* \mathbf{v}_{\mathrm{s}} + \frac{e^* \mathbf{A}}{c} \right] \cdot d\mathbf{s}.
\end{aligned}$$

The term in brackets is the canonical momenta allowing us to reformulate the fluxoid as

$$\Phi' = \frac{c}{e^*} \oint \mathbf{p} \cdot d\mathbf{s}. \tag{1.13}$$

Appealing to the Bohr-Sommerfeld quantum condition [26] (the phase change around a closed loop must be an integer multiple of 2π) we arrive at

$$\Phi' = \frac{c}{e^*}(nh) = n\left(\frac{hc}{2e}\right) = n\Phi_0, \tag{1.14}$$

where $\Phi_0 \approx \left(20.7\,\mathrm{G\mu m^2}\right)$ is the flux quantum. Thus we have shown that London's fluxoid is quantized in units of $hc/2e$ for contours that encircle a topological hole. Note that we have expressed the effective charge of a supercurrent carrier as $e^* = 2e$, a decision that will be justified during our later discussion of Bardeen-Cooper-Schreiffer theory.

1.6.3 General Behavior

Now that fluxoid quantization has been established, physics that mediate this quantization will be detailed. The flux term in Eq. 1.10 is fixed by the applied field, penetration depth, and coherence length. The supercurrent circulating the topological hole then reacts (as described by the supercurrent term in the fluxoid) in a way that keeps the overall fluxoid quantized. As the applied field increases from zero, the induced supercurrent scales linearly to create a field that cancels out the incoming flux, maintaining a fluxoid of zero. Once the applied field is such that the flux is half of the quantized fluxoid value ($\Phi = \frac{1}{2}\Phi_0$), the supercurrent abruptly switches direction, generating a field in the same direction as the applied field to give a total fluxoid equal to the first flux quanta. After the supercurrent reverses directions, its magnitude falls linearly with increasing applied field, reaching zero when the ordinary flux term is Φ_0. This mechanism persists as more and more fluxoids are hosted in a physical hole in a superconductor. However, the fluxoid associated with a single superconducing vortex (introduced in Sec. 1.8) has a maximum value of Φ_0. Thus, in the bulk of a type II material hosting vortices, after the flux for a vortex becomes equal to one fluxoid quanta, increasing the applied field will cause another vortex to nucleate, and the process repeats itself. This behavior persists until the condensation energy reaches zero, destroying superconductivity.

1.7 Pairing Theory Basics

The Bardeen-Cooper-Schreiffer or BCS theory is a remarkably successful microscopic pairing theory of superconductivity. A full treatment of this theory is beyond the scope of this dissertation; instead, the focus will be on its foundational concepts, particularly its pairing theory, which can be used to construct a pseudowavefunction to describe the macroscopic quantum state of superconductors.

This theory relies on basic principles of condensed matter physics. At zero temperature, electrons in a metal fill energy levels up to the Fermi level. At nonzero temperature, the system gains thermal excitation $k_\mathrm{B}T$, where k_B is Boltzmann's constant. The Pauli exclusion principle dictates that no two fermions can occupy the same quantum state; thus the only candidates for excitation are electrons whose energy is within $k_\mathrm{B}T$ of the Fermi level. These will be excited to a narrow energy band ($k_\mathrm{B}T$) above the Fermi level [27].

Cooper considered an attractive potential between the electrons [28, 29]. He showed that if two electrons have an attractive interaction—no matter how weak—they can form a bound state with lower energy than that of two noninteracting electrons. These pairs of electrons are known as

Cooper pairs. This is surprising, because it is well known that in three dimensions, two particles cannot form a bound state if the attractive interaction is too weak. The distinction is that the two electrons are interacting near the Fermi surface, where the number of available states is highly restricted by the Pauli exclusion principle. The only available states for the electrons that compose these pairs are those within $k_{\mathrm{B}}T$ of the Fermi level that were evacuated by thermally excited electrons. As Cooper pairs begin to fill these vacant states, the overall energy of the system is reduced, leading to a stable superconducting state [28, 29].

How can two negatively charged electrons attract? The answer lies in their interaction with the material's underlying crystal lattice. As an electron travels through a solid, it passes many ionic cores. The Coulombic attraction between the electron and an ion distorts the lattice in the form of a phonon. This phonon is a lattice vibration that carries some momentum transferred to it by the first electron. A second electron with opposite momenta (with respect to the first electron) passing by the phonon can absorb its momenta, relaxing the phonon. This leads to an indirect attraction between the two electrons, mediated by the phonon. This interaction is the basis for a Cooper pair [28]. This is a semi-classical simplification of the quantum field theory effects that lead to an attractive potential between the electrons, mediated by a virtual phonon. However, this abstraction gives a sufficient flavor for the true mechanism.

Since electrons are fermions, they have antisymmetric exchange statistics. A wavefunction describing a cooper pair contains both spin and orbital contributions. For spin-singlet pairing, the orbital part is symmetric, implying an antisymmetric spin component. For spin-triplet pairing, the orbital part is antisymmetric, implying a symmetric spin component. Let us introduce a Ginzburg-Landau order parameter for spin-singlet pairing symmetry which can be written,

$$|\Psi\rangle_{\mathrm{s}} = \Delta_{\mathrm{s}} \left(|\uparrow\downarrow\rangle - |\downarrow\uparrow\rangle\right). \tag{1.15}$$

Orbital information is contained in the gap function Δ, which can have spin and/or momentum dependence. The magnitude of the gap function is the condensation energy. The spin portion shows the familiar antisymmetric states associated with spin-singlet pairing. Assuming a position-dependent gap function, we can write $\Delta(r,\theta) = \Delta(r)e^{in\theta}$, where n is the charge-winding number associated with fluxoids. Next we can force the condition of single-valuedness on the wavefunction by ensuring that the wavefunction remains unchanged upon rotations of 2π,

$$|\Psi(\theta)\rangle = |\Psi(\theta + 2\pi)\rangle \tag{1.16}$$

$$\Delta(r)e^{in\theta}\left(|\uparrow\downarrow\rangle - |\downarrow\uparrow\rangle\right) = \Delta(r)e^{in(\theta+2\pi)}\left(|\uparrow\downarrow\rangle - |\downarrow\uparrow\rangle\right) \tag{1.17}$$

Thus

$$e^{in\theta} = e^{in(\theta+2\pi)}, \tag{1.18}$$

which holds true for any integer, n. Then the phase winding is satisfied solely by the contribution of the charge current leading to quantization in units of $hc/2e$ as described in Sec. 1.6.2.

Consider next the case of spin-triplet pairing;which is anisotropic and has spatially varying contributions from the various spin configurations. The triplet state is typically represented in the so-called d-vector formalism,

$$|\Psi\rangle_{\mathrm{p}} = \Delta_{\mathrm{p}}\left(d_x(|\uparrow\uparrow\rangle - |\downarrow\downarrow\rangle) + id_y(|\uparrow\uparrow\rangle + |\downarrow\downarrow\rangle) + d_{\mathrm{z}}(|\downarrow\uparrow\rangle + |\uparrow\downarrow\rangle)\right). \tag{1.19}$$

The d-vector (d_x, d_y, d_z) describes the spin configuration for unconventional superconductors. To make our analysis tractable, let us examine a relatively simple case in which $d_{\mathrm{z}} = 0$. Again, we will introduce a position-dependent gap function,

$$|\Psi\rangle_{\mathrm{p}} = \Delta(r)e^{in\theta}\left((d_x + id_y)\,|\uparrow\uparrow\rangle - (d_x - id_y)\,|\downarrow\downarrow\rangle\right). \tag{1.20}$$

If d_x, d_y are constant, we will arrive at the same fluxoid quantization condition as for spin-singlet pairing. A more interesting example is one for which $d_x = \cos(m\theta)$ and $d_y = \sin(m\theta)$. Then,

$$|\Psi\rangle_{\mathrm{p}} = \Delta(r)e^{in\theta}\left(e^{im\theta}\,|\uparrow\uparrow\rangle - e^{-im\theta}\,|\downarrow\downarrow\rangle\right). \tag{1.21}$$

Combining spin and charge phase contributions gives

$$|\Psi\rangle_{\mathrm{p}} = \Delta(r)\left(e^{i(m+n)\theta}\,|\uparrow\uparrow\rangle - e^{-i(m-n)\theta}\,|\downarrow\downarrow\rangle\right). \tag{1.22}$$

Again, invoking single-valuedness

$$|\Psi(\theta)\rangle = |\Psi(\theta + 2\pi)\rangle\,,$$

requires $m + n$, $m - n$ to be integers. The simplest non-integer solution is $m = n = \frac{1}{2}$. Here, the charge contributes half of the phase, and the spin contributes the other half. Although it does not guarantee that half-quantized fluxoids exist in nature, this construction demonstrates that they are mathematically consistent with the pairing theory. This quantization condition has been predicted in certain unconventional superconductors [28,30–32]. The properties of superconductors capable of hosting half-quantized fluxoids will be detailed in further detailed in Chap. 4.

1.8 Flavors of Superconductivity

In this section, we examine the Ginzburg Landau parameter ($\kappa = \lambda/\xi$), and consider the consequences of different regimes of κ as first described by Abrikosov [33].

1.8.1 Type I Superconductors

For ordinary superconductors, $\kappa \ll 1$ (thus $\lambda \ll \xi$). This means that the distance ξ by which the number density of superconducting charge carriers n_{s} can vary is quite large with respect to the penetration depth λ. In this regime, magnetic flux is expelled from the sample and nearly the entire material is superconducting (aside from the outermost layer with length scale λ). The behavior of these superconductors is well described by the Meissner effect and is appropriately named the Meissner state. Most elemental superconductors fall into this category, and they are known to have relatively low critical fields and temperatures.

1.8.2 Type II Superconductors

The second class of superconductors is those for which $\kappa \geq \frac{1}{\sqrt{2}}$. Their behavior is interesting from the perspective of magnetic imaging. For these Type II superconductors, ξ can vary rapidly with respect to λ, meaning that the order parameter can vary appreciably over small length scales. This leads to a negative surface energy associated with the interface between normal and superconducting states [14, 33]. These materials can superconduct with coexisting normal and superconducting domains. They start in the Meissner state at low applied fields. As the field increases above the *first critical field* H_{c1}, they enter the *mixed state* in which magnetic flux is allowed to penetrate the sample in discrete filaments, leading to small normal (non-superconducting) cores in an otherwise bulk superconductor. This state is characterized by normal cores sprinkled across a superconducting landscape.

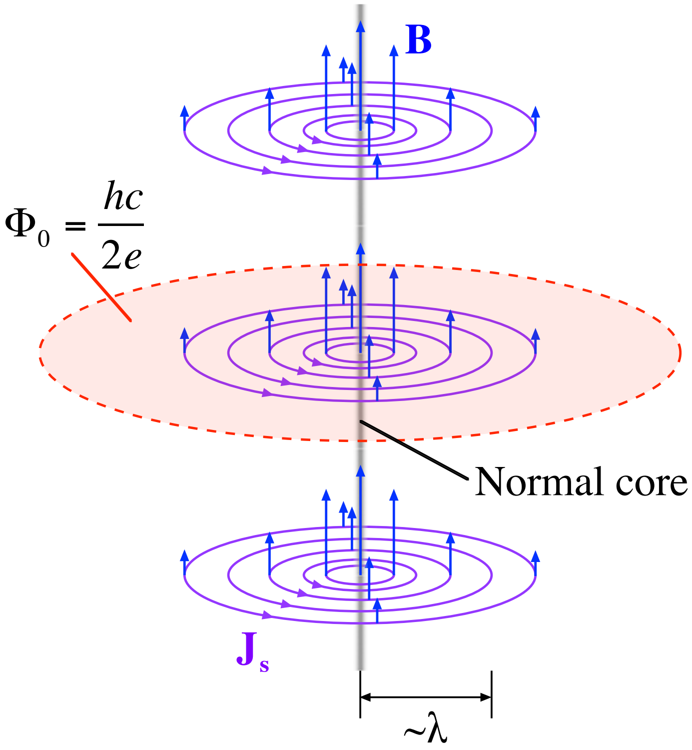

Figure 1.4: Superconducting vortex with normal core (shaded gray region), superconducting currents (purple contours), magnetic field (blue arrows), and integration contour (dashed red line). Note that the field falls off in magnitude (height of arrow) as it deviates from the center of the core.

The normal cores are surrounded by *supercurrents* (superconducting currents) to keep the fluxoid quantized, as seen in Fig. 1.4. The core-current systems are called *vortices*. When the applied field exceeds H_{c1}, it becomes energetically favorable to allow flux to penetrate the superconductor in the form of vortices. As the field increases further, more vortices nucleate to lower the free energy. Mutual magnetic repulsion eventually forces them into a regular array. This process continues until the vortex spacing is similar to the Ginzburg-Landau coherence length causing their cores to overlap. This *upper critical field* H_{c2} suppresses the order parameter, rendering the condensation energy zero and destroying superconductivity. The energy associated with screening currents is greatly reduced by the partial penetration of magnetic flux associated with the mixed state, allowing type II superconductors to persist at temperatures and fields much higher than those of type I superconductors.

Chapter 2

Scanning Hall-Probe Microscopy

> “Cleanliness is next to godliness”
>
> –John Wesley

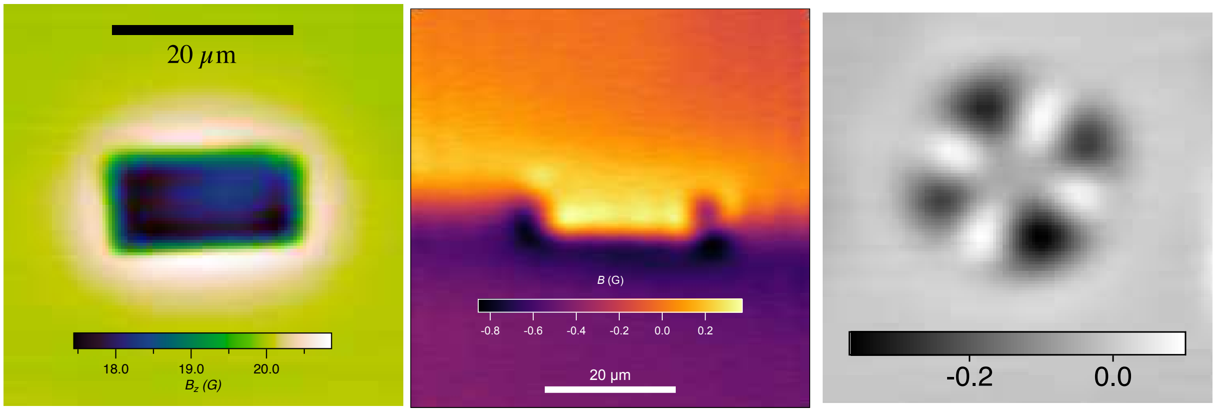

Figure 2.1: A variety of magnetic images produced by our scanning Hall-probe microscope. Each image will be detailed in later chapters.

2.1 Introduction

Magnetic imaging is a powerful means to probe fundamental physics and visualize magnetic structure. Magnetic imaging via scanning Hall probe microscopy is the predominant experimental technique in this work. Figure 2.1 contains a series of representative images that highlight magnetic signatures associated with superconductivity and the spatial distribution of charge-currents. This chapter will provide an overview of SHPM, the probe fabrication process, and our cryogenic, positioning, and scanning systems that facilitate SHPM. To measure a local magnetic field, Hall probes rely on the *Hall Effect*, a specific expression of the Lorentz force. The Lorentz force, $\mathbf{F} = q\mathbf{v} \times \mathbf{B}$, acts on charged particles that are moving in the presence of a magnetic field. In the case of a Hall probe, the charged particles are electrons flowing through a planar conducting channel, and the Lorentz force deflects them laterally. Figure 2.2, an optical microscope image of a Hall probe, shows how this interaction is utilized in Hall-probe microscopy. The image shows three regions. The lightest spans from the bottom right corner to bottom left and top right, a series of four dark branches form a cross with an opening in its center, and an intermediate shade fills the space between the dark cross. The probe-wafer materials used to fabricate Hall probes have a thin conducting layer—in both the darkest and lightest orange regions, the conducting layer has been etched through, rendering them insulators. The intermediate orange geometry defined by the etched features provides a conducting path that connects the four contacts (labeled $\mathrm{I}^+, \mathrm{I}^-, \mathrm{V}^+, \mathrm{V}^-$) to the *active area* (center of the cross) where the Hall measurement takes place.

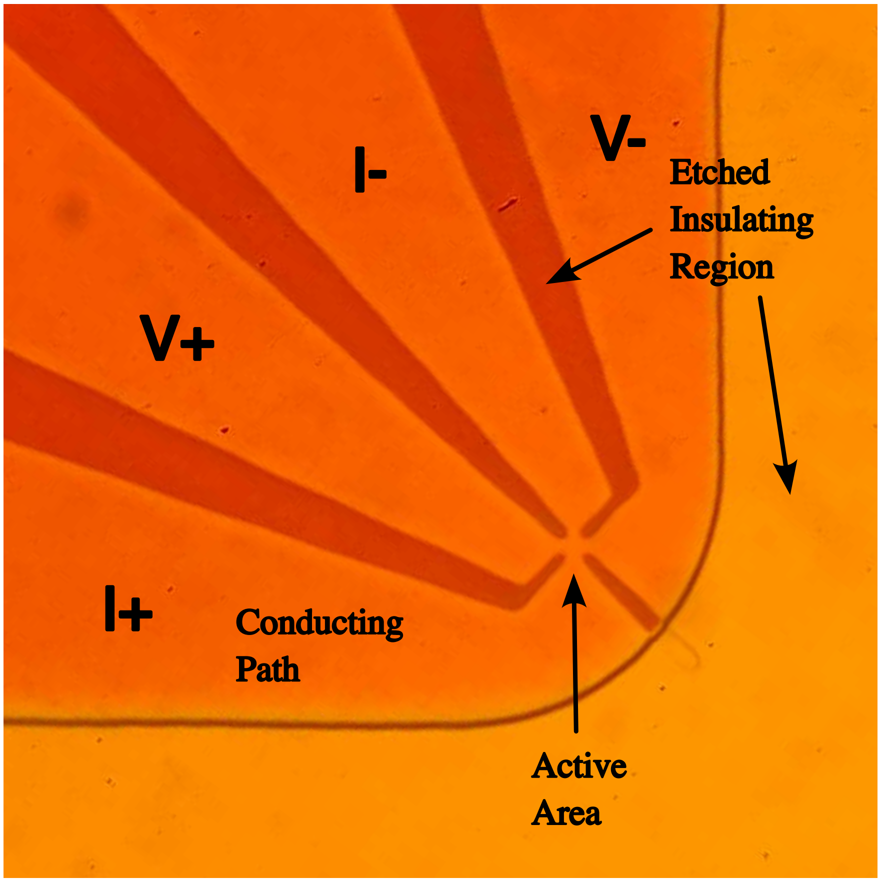

Figure 2.2: An optical photo of the active area of a Hall probe. Lightest and darkest shaded regions have been etched through conducting plane, forcing current to pass between leads labeled I^+/I^-. The probe is sensitive only to magnetic fields in the approximately 1 $\mu\mathrm{m}^2$ active area.

An AC current is passed between the leads labeled $\mathrm{I}^+, \mathrm{I}^-$, while the voltage is simultaneously measured across the leads labeled $\mathrm{V}^+, \mathrm{V}^-$. In the presence of a magnetic field with a component perpendicular to the plane of the Hall probe, the electrons composing the current will be deflected, causing them to accumulate on one transverse side of the active area. This leads to a measurable voltage difference that is proportional to the applied field, the *Hall voltage*, which is the signature of the Hall measurement. A schematic of an idealized 2D Hall probe is shown in Fig. 2.3 [34] to illustrate the relative orientations of the applied current, voltage leads, and magnetic field. During a measurement, this voltage is calibrated with a well-known magnetic field to quantify field strength. The Hall voltage can be approximated as

$$V_{\mathrm{H}} = \frac{IB}{n_{2\mathrm{D}}e} = IB\frac{\mu}{\sigma}, \tag{2.1}$$

where I is the applied current, B is the magnetic field, $n_{2\mathrm{D}}$ is the two dimensional charge-carrier density in the conducting channel, and e is the charge of the carrier (electron in this case), respectively. In the second equality, μ and σ are the mobility and conductivity of the conducting channel. This approximation informs Hall probe design—the Hall voltage is inversely proportional to charge-carrier density, conductivity, and thickness of the conducting channel—highlighting why Hall probes are typically made from semiconductors rather than metals.

Our system implements two-dimensional raster scanning (to be detailed in Sec. 2.3.3) to produce planar magnetic images. Example images are shown in Fig. 2.1. The spatial resolution (SR) for these images is limited by the size of the active area (a) and the scan height (h), approximated by [35]

$$\mathrm{SR} = \sqrt{a^2 + h^2}. \tag{2.2}$$

The active area of our probes is approximately 1 $\mu\mathrm{m}^2$; precise values depend on sidewall electron depletion during fabrication, which we have no method to accurately measure (but will be commented on in Sec. 2.2). Typical scan heights for our system are 0.5 – 1 μm, giving a spatial resolution on the order of 1 $\mu\mathrm{m}^2$. The magnetic field resolution is limited by probe sensitivity and

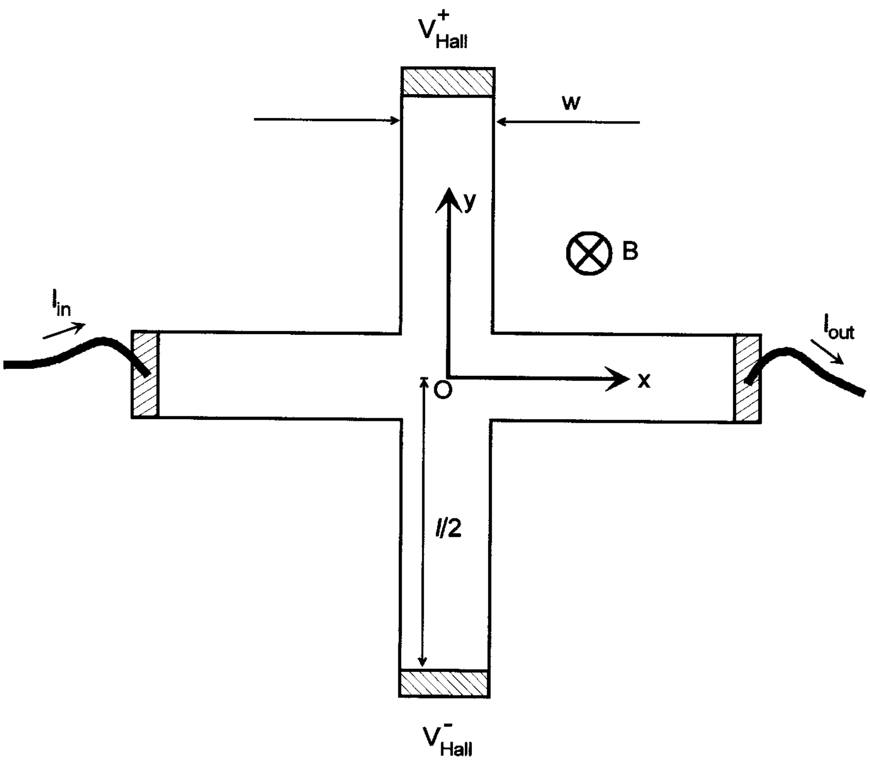

Figure 2.3: A schematic representation of the Hall effect in an idealized 2D Hall probe. Current passes from I_{in} to I_{out}. The magnetic field passing through the plane of the Hall geometry will deflect electrons in the y-direction, leading to a voltage difference across V^{+}_{Hall}, V^{-}_{Hall}. Reprinted from: *Local magnetic probes of superconductors*, by S. J. Bending, *Advances in Physics*, 48(4), 449–535 (1999), © 1999 Informa UK Limited, trading as Taylor & Francis Group. Reprinted by permission from https://www.tandfonline.com

various sources of noise. In our system, probes have a field resolution of approximately 10 mG and a noise spectral density of around 2.5 $\mathrm{mG}/\sqrt{\mathrm{Hz}}$.

The advent of modulation-doped tunable semiconductors allows high mobility and low carrier density, providing an optimal platform for Hall sensing [36, 37]. The layered semiconducting structures used for probe fabrication are commonly composed of gallium arsenide (GaAs) and aluminum gallium arsenide ($\mathrm{Al}_x\mathrm{Ga}_{1-x}\mathrm{As}$). The thin conducting plane that forms at the interface between these two materials, referred to as *two-dimensional electron gas* or 2DEG, arises from the difference in the conduction band energy ΔE_c between GaAs and AlGaAs [38,39]. GaAs has a fixed conduction band energy of 1.42 eV, while that of $\mathrm{Al}_x\mathrm{Ga}_{1-x}\mathrm{As}$ varies with aluminum concentration x. Our heterostructures have an aluminum concentration of $x \lesssim 0.44$. There is an approximately linear relationship in x for the difference in conduction band energy $\Delta E_\mathrm{c} = 0.88x$ [38].

While the precise heterostructure varies by wafer, a typical sequence for AlGaAs-GaAs heterostructures exists for Hall probe fabrication. The surface layer is a thin GaAs cap that serves to passivate the wafer, preventing oxidation [40]. Beneath the cap lies a relatively thick undoped AlGaAs layer, which separates the 2DEG from surface effects. This is followed by a silicon-doped layer of AlGaAs which acts as a source of donor electrons. A thick AlGaAs spacer layer is grown under the doped region to spatially separate the donors from the 2DEG. As donors become ionized, they produce an irregular potential that can cause scattering in the conduction plane—the spacer layer minimizes these affects. The last layer is a macroscopic GaAs substrate. The 2DEG forms at the interface between the AlGaAs spacer and GaAs substrate, where electrons from the doped layer tunnel through the spacer layer and into the lower energy conduction band of GaAs [41]. These conducting planes have high carrier mobility and low carrier density at cryogenic temperatures. The electrons in the conducting channel are confined to a narrow well, typically around 10 nm [35]. This thin layer is ideal, as the Hall signal is inversely proportional to the two-dimensional number density of the conducting channel as shown in Eq. 2.1. 2DEGs are approximately 50 – 120 nm below the surface of the heterostructure for our wafer materials. The layer structure of a specific GaAs/$Al_{0.3}Ga_{0.7}As$ heterostructure and its conduction band energy as a function of wafer depth are shown in Fig. 2.4 to emphasize the formation and location of the 2DEG [34]. Note that in this wafer, the doping is confined to a thin quasiplane. The conduction-band energy diagrams are sketched by self-consistently solving the 1D Poisson equation and Schrodinger equation while considering the charge density associated with each layer [42].

2.2 Probe Fabrication

Fabricating a Hall probe is a delicate process in microfabrication. A successful device depends on a carefully optimized sequence, each step of which is critical to a functioning probe. Much of my graduate work was dedicated to refining this procedure to minimize device noise and improve yield. Fabrication can be divided into the following steps: scribing and cleaving a small square, cleaning and thinning the square, etching a *mesa* to encourage electrical contact with the conducting channel,

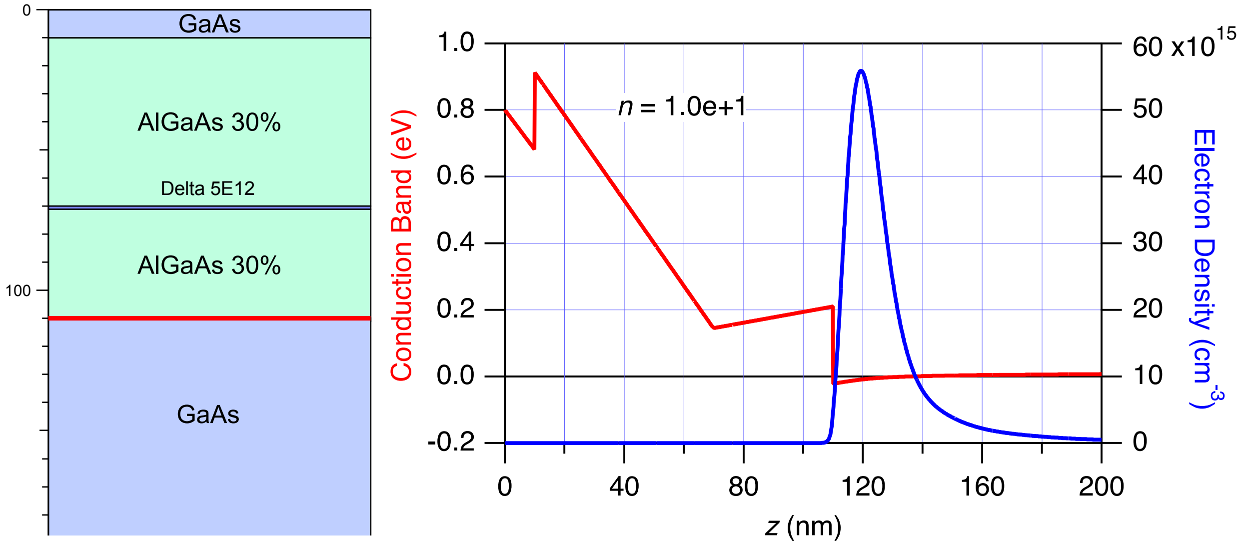

Figure 2.4: Layer structure of a GaAs/Al$_{0.3}$Ga$_{0.7}$As heterostructure (left). The 2DEG is represented with the red line at the AlGaAs/GaAs interface. Sketch of the corresponding conduction-band energy as a function of wafer depth (right). Note the spike in number density at the 2DEG location.

evaporating and annealing gold-germanium-nickel contacts, defining and etching insulating regions that form the conducting channel, etching the *deep crosses* that delineate individual Hall probes, and finally scribing and separating the completed devices. The fabrication process is described below in great detail to support future efforts in producing probes.

2.2.1 Scribing and Cleaning a Square

The scribing is executed on a Karl-Suss diamond scriber, shown in Fig. 2.5. We have a specific diamond tip in our lab that is dedicated to the material so that it remains sharp. We often scribe silicon which is very hard and could potentially dull the tip over time. The wafer is scribed into 4.8 mm × 4.8 mm squares—each of which will become four Hall probes. Typically, a long strip is scribed that spans the length of the wafer. That strip is cleaved before being loaded back onto the scriber to be scribed and cleaved into a series of smaller squares.

The scribing process is carried out by a pyramid-shaped diamond tip, and the scribes are sensitive to the angle between the tip and the wafer. To ensure a proper angle, a camera and light source are positioned on opposite sides of the vacuum chuck, giving a two-dimensional profile of

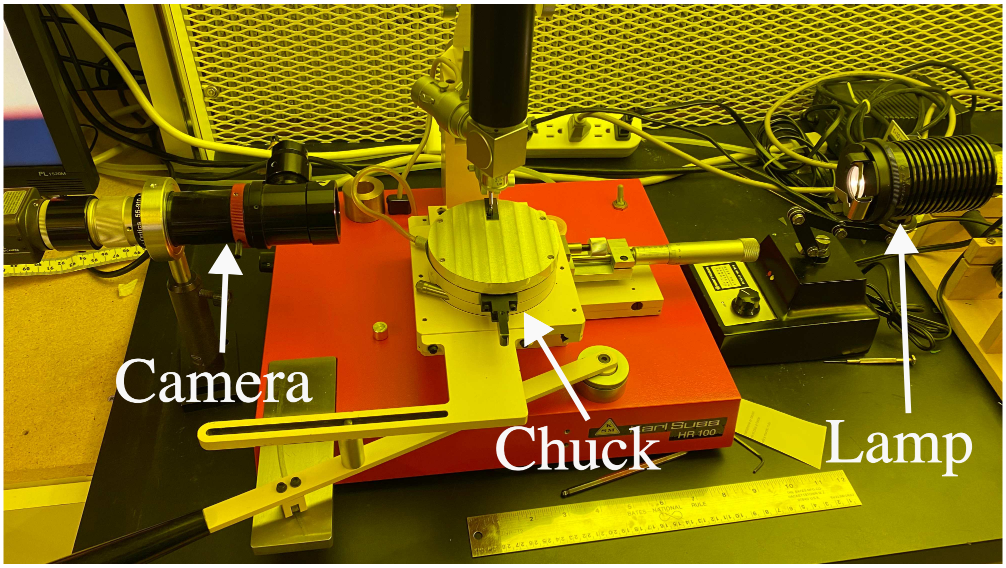

Figure 2.5: Karl Suss diamond scriber used for scribing. The camera that's used to ensure a proper scribing angle is shown on the left while the lamp that projects light onto the tip and wafer for the picture is shown on the right. The scribing chuck is centered under eye piece. The bottom of frame shows handle used to slide the chuck under the diamond, completing the scribe.

the cutting tip and wafer. This image is projected on a screen from which the scribing angle can be measured, as shown in Fig. 2.6 along with a schematic of the scribing angle. Photos of the cutting tip can be difficult to interpret, as it is difficult to distinguish the top surface of the wafer. However, the substrates are very clean, providing a sharp reflection of the cutting tip on the wafer. The angle between the cutting tip and its reflection, as seen through the camera, provides an easy method to measure the scribing angle by considering the geometry shown in Fig. 2.6.

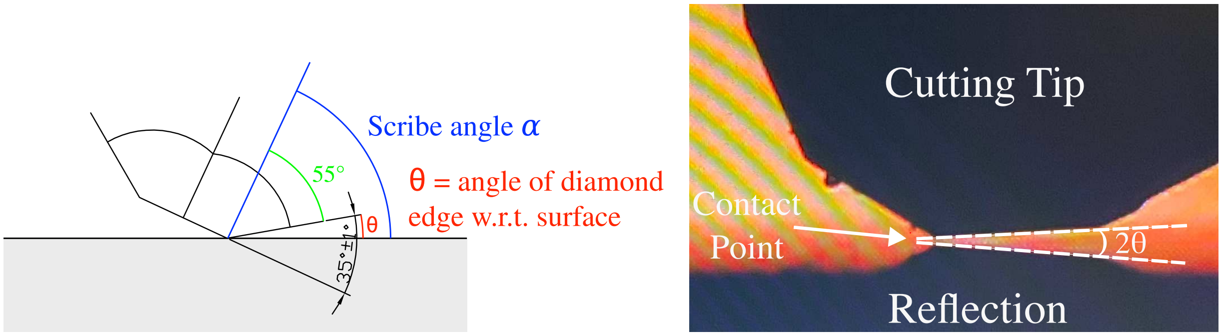

Figure 2.6: The scriber has a pyramid-shaped diamond cutting tip. The success of a scribe is influenced by the angle between the diamond tip and the substrate. The left image shows a schematic of the diamond cutter and what is meant by the scribe angle. The right image shows a capture from our camera that is used to ensure a proper angle.

Once the strips have been scribed, they need to be cleaved apart along the scribe lines. Even with a sophisticated scriber, it is difficult to get a clean cleave from these strips as the wafer material is typically on the order of 700 µm thick. Once the strip has been scribed into a series of smaller squares, it is fixed to a glass slide with the thermoplastic adhesive Crystalbond. Crystalbond liquefies on a 135 °C hot plate, but quickly solidifies as it cools. The strip is carefully positioned on the glass slide such that one square is hanging over the edge of the slide and its scribe is directly on top of that edge. The far side of the square is gently pressed with a toothpick to obtain a clean cleave. Carefully adhering the strip to the glass slide and positioning the squares over the edge one by one is a time-consuming process. However, this time investment greatly improves the likelihood of a successful cleave.

2.2.2 Cleaning and Thinning the Square

Probe fabrication is extremely sensitive to the cleanliness and surface conditions of the wafer material [2], so carefully cleaning it is a critical step before further processing. To start, three 250 mL Pyrex beakers are filled with acetone, methanol, and finally water and sonicated for 60 s in each solvent. Then, each of the beakers is refilled with one of the three solvents. Next, a square is placed on a Teflon ladle and lowered into the acetone bath. The beaker (with square and ladle) is sonicated for 5 min. Then, the square is rinsed with methanol over the acetone beaker before being lowered into and sonicated in the methanol beaker. The process is repeated again for the beaker filled with water.

After the series of sonications, a pair of tweezers is used to suspend the square while rinsing it for 30 s each with acetone, methanol, and finally water before being blown dry with a high-purity N_2 source. It is important to carefully hold the square by one of its corners to minimize the contact area. This cleaning process was informed by the thesis of John Watson [2]. The cleaned surface is protected for further fabrication steps by spinning on a layer of Shipley S1813 photoresist and subsequently baking for 60 s on a hot plate at 135 °C.

As was previously mentioned, four Hall probes are fabricated out of each square. The final step of fabrication is to scribe and cleave the square into its four probes. To increase the likelihood of a successful final cleave, the squares are first thinned to approximately 220 µm. This thinning is performed by fixing the square to a steel collar and puck system shown in Fig. 2.7 and grinding the backside of the wafer in a slurry of water and aluminum oxide.

The square is fixed to the end cap of the steel puck with Crystalbond. The clean, photoresist-covered side makes contact with the puck, leaving the unpolished side of the square exposed. The slurry is formed by mixing tens of grams of aluminum oxide no. 5 (grain size of 20 – 40 µm) with tens of milliliters of water on top of a glass plate. The end cap with the wafer attached is slowly lowered through the collar until it rests on the slurry. A system of magnets and set screws is used to gently touch the puck to the grinding surface, as crashing the square onto the glass will fracture it. The collar is held in a gloved hand and slow circular movements are made letting the weight of the puck provide the pressure for grinding. Typical grinding rates are approximately 2 µm/s, thinning the square from 700 µm to 220 µm in a matter of minutes (depending on the water content of the slurry). It is important to stop grinding periodically to measure the thickness of the square with a dial indicator (see Fig. 2.7). This not only measures the current thickness, but also establishes a rate that can be used to predict grinding times. Thinning is a tedious step due to the safety concerns associated with gallium arsenide dust. The grinding process is carried out in a fume hood and is contained within a plastic receptacle. In addition, appropriate PPE is worn and gloves, collar, and puck are thoroughly cleaned to contain dust to the plastic bin before each thickness measurement. Once the wafer has been ground to the desired thickness, it is carefully loaded onto a piece of backing glass to provide easier handling for future processing steps.

2.2.3 Contacting the 2DEG

Gold-germanium-nickel contacts

Establishing high-quality ohmic contact to the 2DEG (approximately 100 nm below the surface) is one of the most challenging steps in probe fabrication. It has been a long-standing problem for

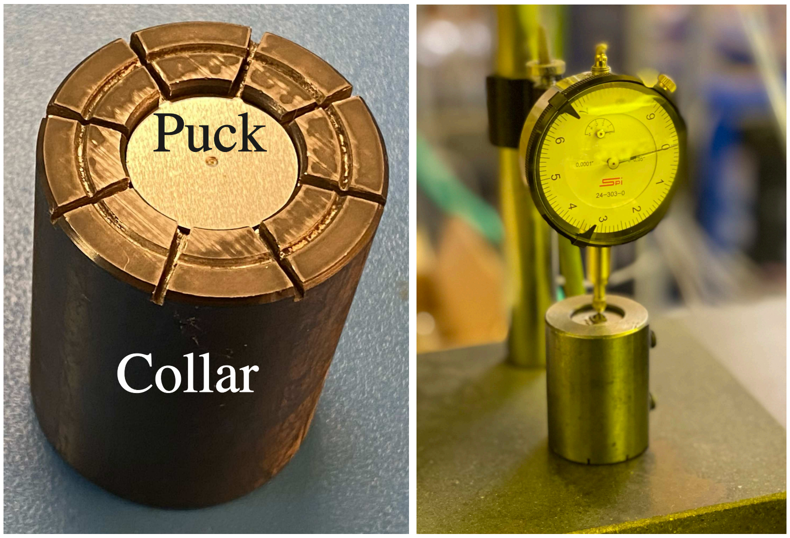

Figure 2.7: Pictured on the left is our puck and collar for grinding. Puck and collar were machined out of steel. Substrate is fixed to collar with thermoplastic adhesive. The right image features a dial indicator that we use to track the progress of the wafer grinding. Puck and collar must be thoroughly cleaned before using the dial indicator to prevent contaminating lab surfaces with arsenic-containing compounds.

our lab and the industry at large. The most common method for contacting the 2DEG in these heterostructures is thermally evaporating gold-germanium-nickel contacts and annealing them in an inert environment. A clean metallization, proper ratio between constituent metals, and an overall contact thickness optimized for the depth of the 2DEG are critical. Gold and germanium both have melting points on the order of 1000 °C; however, their eutectic alloy with a ratio of 88% Au and 12% Ge by weight melts at a much lower temperature of 360 °C [43].

The physics of the annealing process are subtle and remain an ongiong area of research. Historically, thin gold-germanium-nickel spikes were believed to form during the annealing process, penetrating the wafer surface and eventually the 2DEG where they establsihed ohmic contact [44]. A modern study used transmission electron microscopy and energy-dispersive X-ray spectroscopy (EDX) to examine the annealing process in greater detail [45]. Near the eutectic melting temperature, gold and germanium separated, allowing the germanium to combine with nickel. The resulting germanium-rich nickel grains migrated toward the wafer surface due to the wetting properties of nickel. At temperatures around 400 °C, gold- and nickel-rich grains diffused through the wafer surface and toward the 2DEG, while gallium and arsenide flowed upward toward the surface. EDX measurements confirmed that gallium diffuses mainly into gold, and arsenide preferentially diffuses into nickel [45]. This backflow leads to gold-gallium alloys and nickel-germanium-arsenide compounds tens of nanometers below the wafer surface. Germanium continues to diffuse into the AlGaAs layers, ultimately doping the semiconductor near the 2DEG and establishing ohmic contact beyond a certain doping threshold [45].

Cog-Shaped Mesa Etch

The first fabrication step to produce ohmic contact is to define and etch a *cog*-shaped mesa in the center of the square. This leaves a cog-shaped area with an intact 2DEG and an outer region stretching from the edge of the cog to the edge of the wafer, which will be etched deeply, destroying the 2DEG. This pattern is useful for a host of reasons; it promotes lateral diffusion, avoids the "bad" direction of the heterostructure (see below), and establishes a long border between the edge of the contacts and the 2DEG.

The contact pattern is complementary to the cog pattern, but overlaps the mesa by 3 μm. This promotes lateral diffusion through the side walls of the previously etched pattern and results in better mobility at low temperatures [2]. Another concern for contacting the 2DEG is the so-called good- and bad-directions. Contact interfaces oriented along one crystal axis have been found to have lower resistance and better reproducibility than those oriented perpendicular to it [2]. One way to bypass this dependence on direction is to produce a *scalloped* contact design (see Figs. 2.8, 2.9) in which the contacts interface with the 2DEG in orthogonal directions, providing every contact with exposure to the preferred direction. Lastly, it has been shown that the area underneath the contacts does not influence the contact resistance, but rather the length of the border by which the contacts interface with the 2DEG [43]. This scalloped design significantly increases the length of that border, improving electrical contact.

To fabricate this mesa, a layer of Shipley's S1805 photoresist is spun on the square and baked. Next, the mesa is defined photolithographically and photodeveloped with AZ 917 MIF, leaving a protective cog of photoresist in the center of an otherwise exposed wafer surface. This cog pattern underneath the photoresist is the only portion of the wafer for which the 2DEG will conduct. The

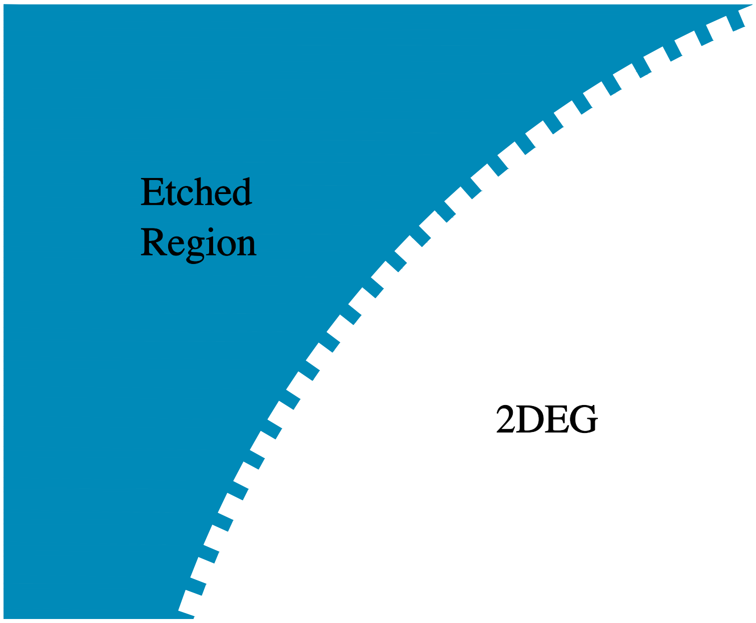

Figure 2.8: A quadrant of our cog etch design defined by alternating rectangles of approximately 8.5 µm ×4 µm and 8.5 µm ×11 µm. The blue region is exposed by the laser and eventually etched away. The white region remains unetched and will conduct.

teeth of this pattern are alternating rectangles of approximately 8.5 µm ×4 µm and 8.5 µm ×11 µm. A wet-etch technique is utilized to remove the 2DEG in the exposed region with a 1:1:78 ratio (by volume) of phosphoric acid, hydrogen peroxide, and water as the etchant. This is a common recipe for etching gallium arsenide [46], and this particular ratio leads to a rate of approximately 1 nm/s at room temperature.

Contact design

There are two main considerations for contact design: a large pattern that can be easily aligned with mesoscopic contacts (see Fig. 2.10) and one that overlaps with the mesa defined by the cog etch (see Fig. 2.11). Since electrical contact to 2DEG relies mainly on the interface that the contacts share with the etched cog, the details of the design are not critical to the performance of the probe aside from that interface [43].

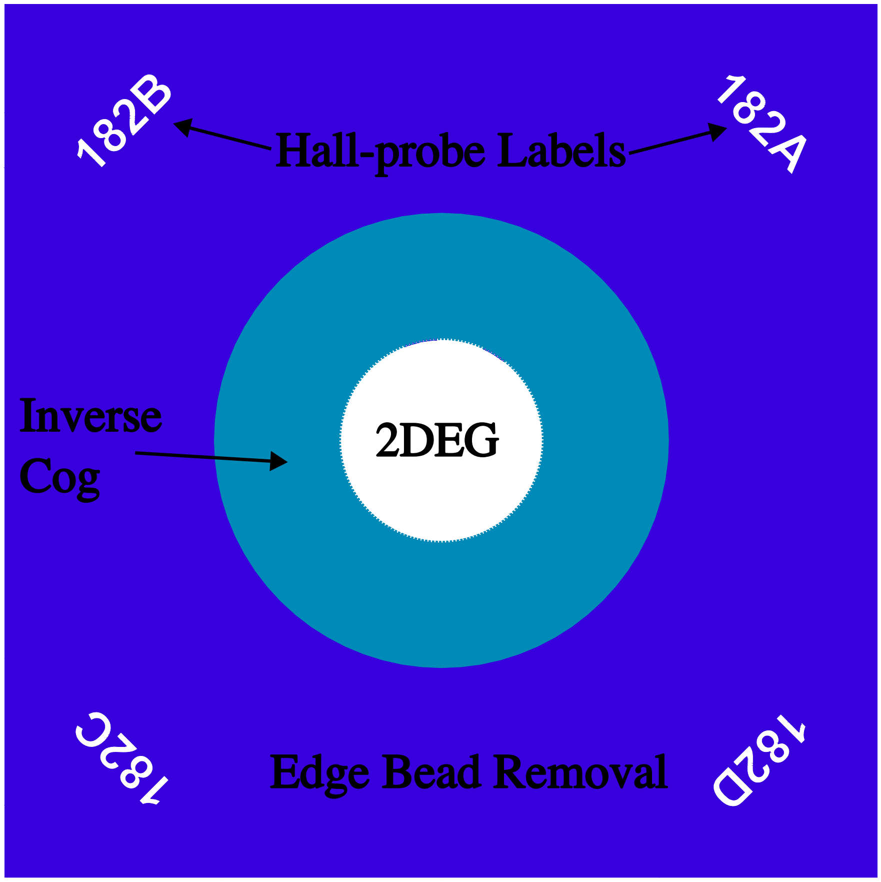

Figure 2.9: Schematic of the cog etch and edge bead on the scale of the entire wafer. The inner portion is the conducting mesa. The turquoise intermediate layer is the etched region immediately surrounding the cog. The outer region is the "edge bead" portion of the mask and will have a significantly larger exposure due to the increased photoresist thickness near the edges of the wafer. The entire mask is 5 mm × 5 mm.

Contact Fabrication

The starting point for contact evaporation is a clean, thinned square with an etched cog, as described in the previous section. That square is dipped in hydrochloric acid (HCl) for 5 s, rinsed in water, and dried with N_2. HCl is thought to etch through native oxides on the surface of the wafer and promote better photoresist adhesion [47]. Strong adhesion prevents the etchant from leaching under the photoresist, destroying the 2DEG in unintended areas. After this dip and rinse, we quickly spin and bake a layer of liftoff resist (Shipley's LOR3B) followed by a layer of conventional photoresist (Shipley's S1805). LOR3B promotes clean *liftoff* after metal evaporation (or sputtering). During development, the conventional photoresist will only dissolve in areas that were photolithographically exposed while the liftoff resist will develop regardless of whether it

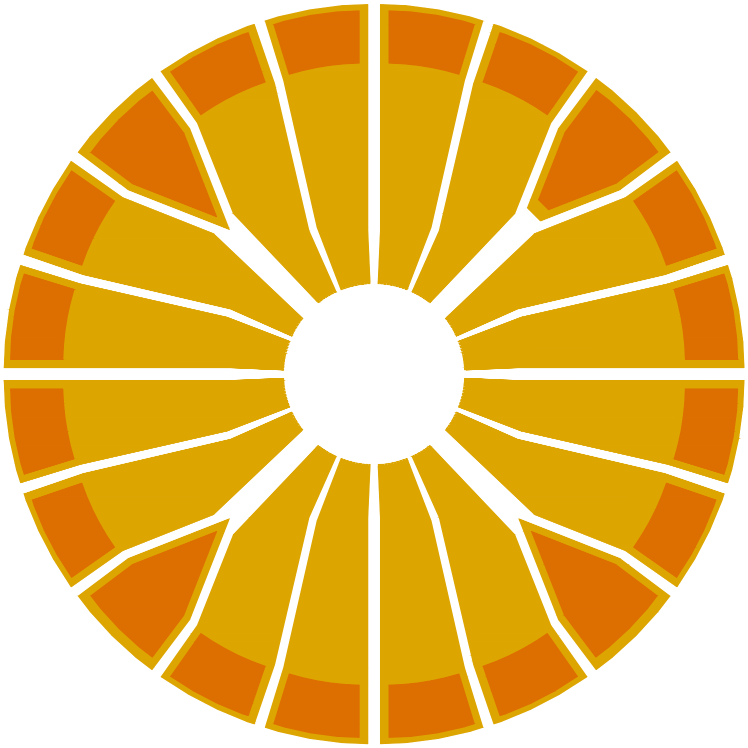

Figure 2.10: Macroscopic contact design. Darkest orange region is the edge bead pattern for the contacts and is subjected to a significantly higher exposure than the rest of the mask.

has been exposed. First, the top layer of photoresist will dissolve, followed by the liftoff resist which dissolves vertically toward the wafer surface and laterally under the window opened in the photoresist. This produces an *undercut* that disconnects the metal deposited on the wafer surface from that which covers the photoresist and sidewalls, encouraging a successful liftoff [48]. This process is represented schematically in Fig. 2.12.

Contact Evaporation

After the contacts have been photolithographically exposed and photodeveloped, we are ready for contact evaporation. First, the square is oxygen plasma ashed (approximately 300 mTorr, 80 W, 30 s) and then dipped for 3 s in TMAH and then HCl. Next, it is fixed to a plate used to hold samples in the evaporation chamber with Crystalbond, and rushed to the evaporation chamber. The plasma ash removes resist scum and carbon based surface contaminants. TMAH and HCl are believed to aggressively clean the surface and remove persistent oxides [2]. The presence of surface oxides

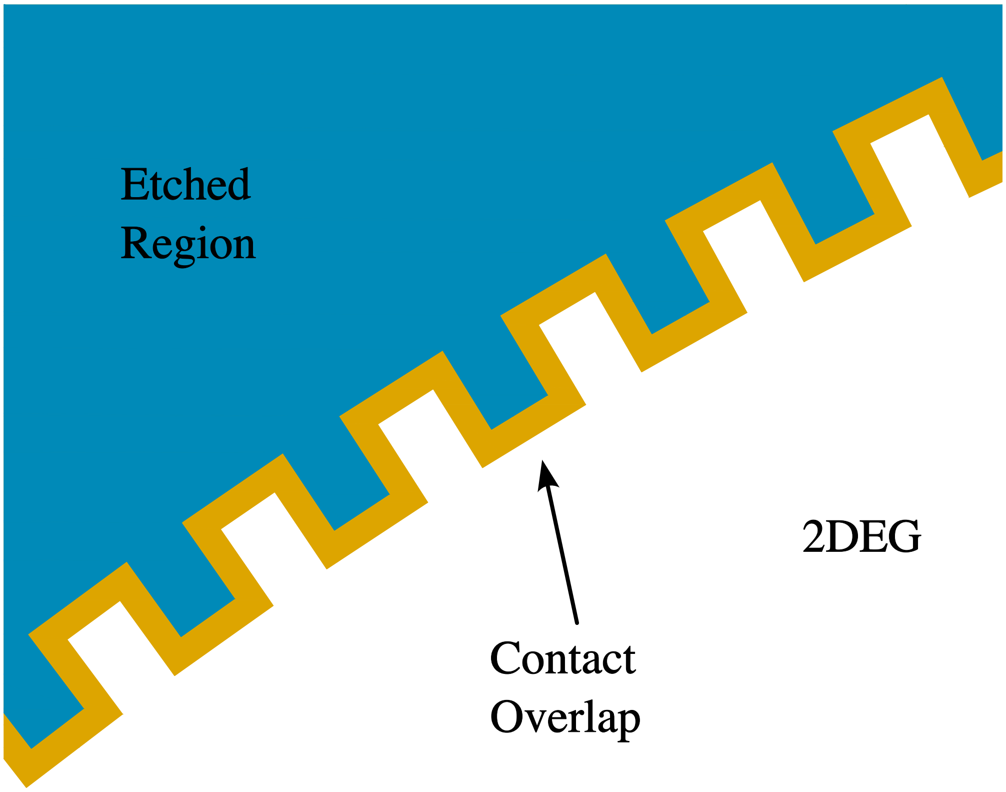

Figure 2.11: This schematic shows the overlap between the etched cog (blue), and the contact mask (gold). This 3 µm overlap promotes lateral diffusion through the sidewalls of the etched mesa and encourages electrical conduction [2].

prevents the growth of high-quality contacts [2, 43], so minimizing air exposure after the acid dips is prudent.

Following the advice of Göktaş *et al.* [43], we use a eutectic mixture of 107.2 nm of gold, 52.8 nm of germanium, and 40 nm of nickel for a 2DEG depth of 80 nm or less. For deeper 2DEGs, we scale the constituents of the recipe by a factor of

$$S = \frac{D + 30\,\text{nm}}{110\,\text{nm}}, \tag{2.3}$$

where D is the depth of the 2DEG in nanometers.

During contact evaporation, it is important to limit impurities in our film growths. The main culprit is contamination from insufficient vacuum or outgassing. To ensure proper vacuum, we pump the chamber with a turbo pump for an extended period of time, typically 24 to 48 h, after which

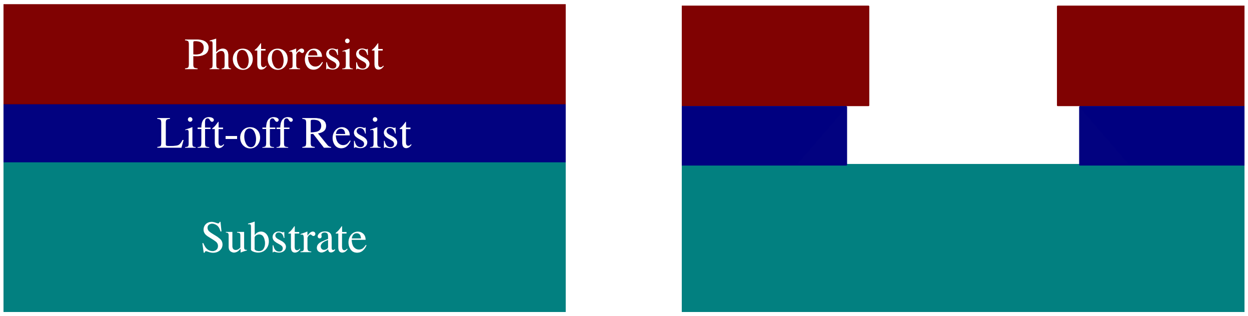

(a) Resist stack **(b)** Photodevelopment

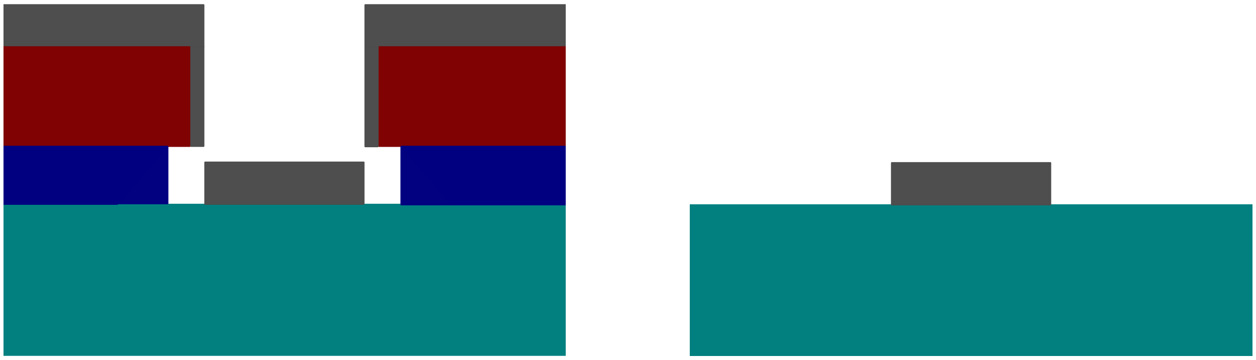

(c) Metallization **(d)** Liftoff

Figure 2.12: (a) Resist stack for liftoff. Photoresist is top red layer, lift-off resist is blue layer, and silicon substrate is torquoise. Typical lift-off resist and photoresist thicknesses are approximately 0.3 µm and 0.5 µm, respectively. (b) A window has been exposed and developed in the photoresist. Lift-off resist has been developed, leaving an undercut between the photoresist and substrate. (c) Metal has been evaporated, leaving a thick coating of metal on the top surfaces of the photoresist and substrate, and a thin coating on the sidewalls of the photoresist. (d) Resist has been lifted off, leaving behind a metallization on the substrate.

a typical vacuum pressure is approximately 0.6 µTorr. To limit outgassing before pumpdown, we carefully clean the surfaces inside our evaporation chamber with methanol on a technical wipe and bake out the evaporation sources under vacuum. To bake out the sources, we run current through them to heat and drive off volatiles that would otherwise be liberated during the evaporation and thus incorporated into the metallization. This is particularly important for alumina evaporation sources that have a large internal surface area and, therefore, outgas a significant amount of water vapor. While outgassing, the pressure increases by a few µTorr. Several hours after outgassing, typical pressures are approximately 0.4 µTorr. Once the sources have been baked out and the chamber has returned to the base pressure, we are ready to evaporate the contacts. We maintain a relatively high evaporation rate (tens of Å/s), as a lower rate incorporates more oxygen into the film. We first evaporate gold, followed by germanium, and finally nickel [43].

After the evaporation, we are ready to lift off the contacts. We heat a Pyrex beaker of dimethyl sulfoxide (DMSO) to 155 °C and lower the substrate into the solution via the Teflon ladle. DMSO dissolves the remaining photresist and liftoff resist, allowing the metal film to float away where it has not adhered to the surface of the wafer. This liftoff can be performed with acetone; however, the volatility of acetone presents challenges. If a square lifted off in acetone is not quickly rinsed with water, the acetone can evaporate, allowing lifted-off metal segments to adhere to the surface. DMSO is oily and has a low vapor pressure, giving ample time to rinse with water before adhesion.

Contact Annealing

Once the contacts have been lifted off, they are ready to be annealed. First, the square is given a three-solvent rinse before being removed from the backing glass. The square is laid on a small portion of a technical wipe, approximately 15 mm × 15 mm in size. The square and the wipe are rested on the Teflon ladle and acetone, methanol, and water are dribbled over it for 30 s each before being dried with N_2. This is a dangerous step, as the thinned square is very light and a strong spray of a solvent or N_2 will launch it out of the ladle. Gently blowing N_2 from any angle other than vertical will have the same result.

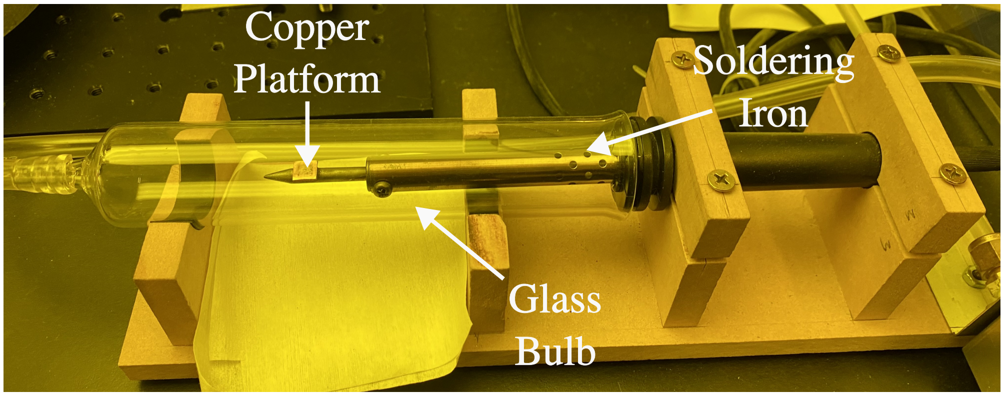

Figure 2.13: Our custom annealing setup. Temperature controllable soldering iron with a copper platform to hold the substrate. Forming gas is flowed through the rubber tube and into the glass bulb to provide an inert atmosphere.

Once the square has been cleaned, it is loaded into our annealing station which can be seen in Fig. 2.13. The annealer is a temperature-controlled soldering iron with a flat copper platform fixed to its tip, which serves as the annealing surface. The iron is housed in a glass tube that is connected to a flow controller and forming gas (an inert gas with high levels of nitrogen (approximately 95%) and a small amount of hydrogen (approximately 5%) hydrogen) tank with a rubber hose, allowing a forming gas environment with variable flow rate.

The annealing is done in two parts: first, the square is annealed at 370 °C for 2 min, followed by 2 min at 440 °C [43], aligning with the previous discussion of the annealing process. Successful contact growth and anneal can be verified by measuring the resistances between contacts with a tabletop multimeter. Typical resistance values that indicate working contacts are on the order of 20 kΩ. There is a strong correlation between the appearance of the contacts and successful annealing. The complicated physics of the annealing process leads to a striking change texture of the contacts compared to that before annealing, as shown in Figs. 2.14, 2.15. The texture transforms from smooth to a pattern reminiscent of a dry river bed. After gaining experience from fabricating dozens of probes, one can inspect the contacts under an optical microscope and determine whether they were successful.

Annealing in a forming gas environment [2] has greatly improved our success rates in forming ohmic contact. Previously, contacts were annealed in a N_2 environment, producing good and bad

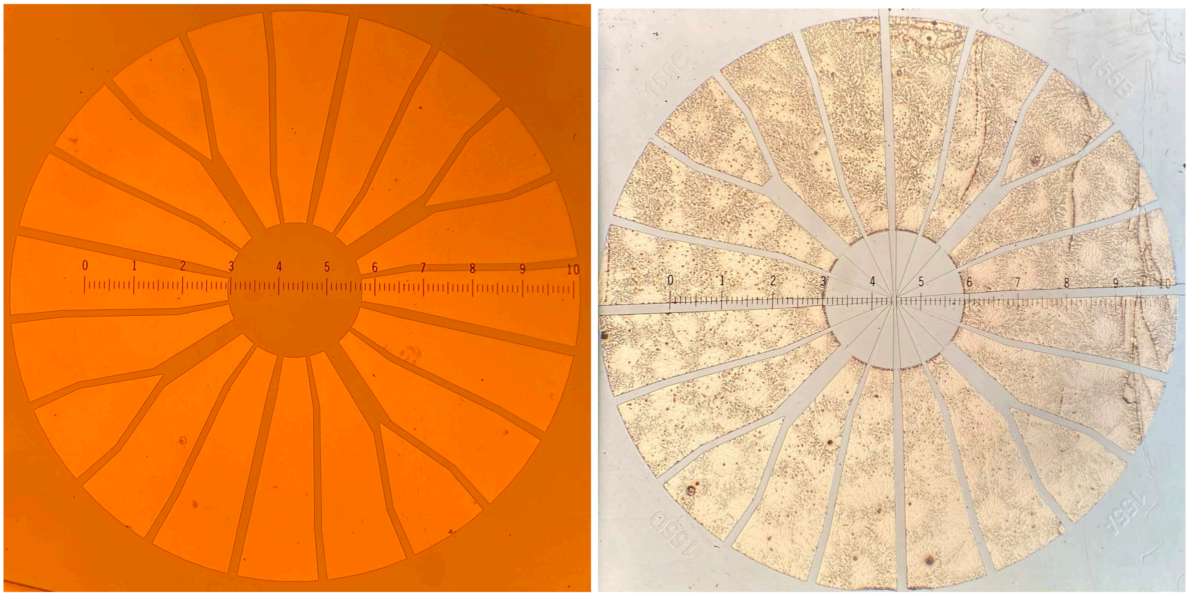

Figure 2.14: Full wafer optical microscope images of contacts before and after annealing to highlight change in texture. Small reticle divisions represent 40 µm. Left picture shows wafer after liftoff, but before annealing. Right image shows wafer after successful annealing.

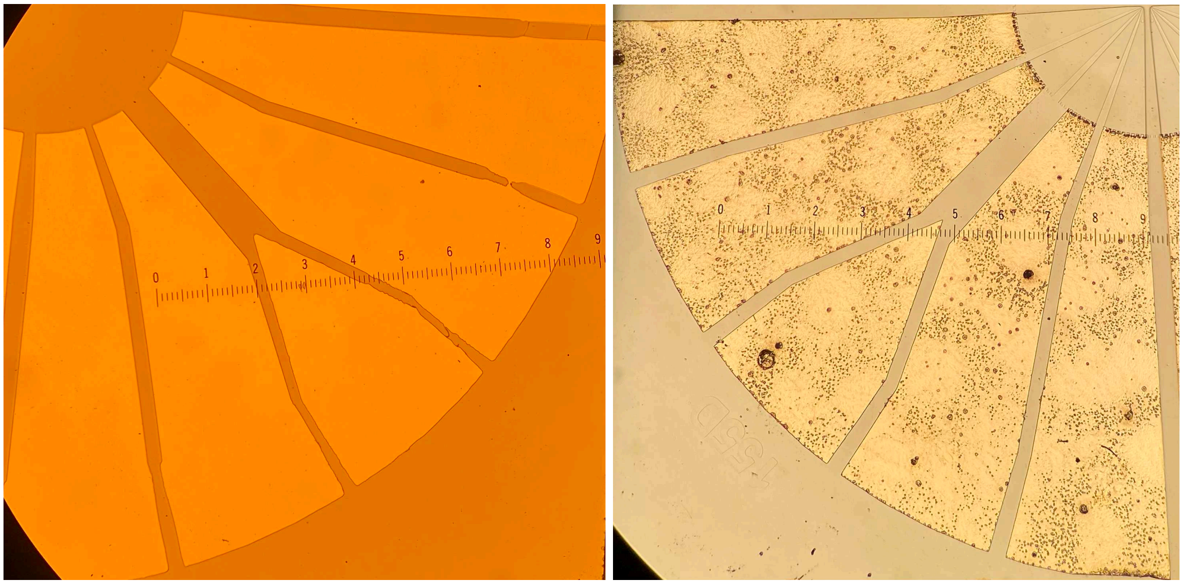

Figure 2.15: Optical microscope images of one quadrant of contacts before and after annealing to highlight change in texture. Small reticle divisions represent 20 µm. Left picture shows wafer after liftoff, but before annealing. Right image shows wafer after annealing.

contacts at similar rates. The forming gas has led to much better reproducibility—typically if the contacts did not anneal properly, it was due to surface cleanliness or evaporation issues.

2.2.4 Insulating Features

The next step is to fabricate the active area of the Hall measurement, which is depicted as the cross with an opening in the center in Fig. 2.2. The insulating arms of the cross emanate from gaps between adjacent contacts and confine current to flow between I^+, I^- leads as well as defining the conducting path for the voltage measurement. Recall that the spatial resolution of the probe is fixed by the size of the active area. When designing the active area, there is a balance between resolution and noise. A substantial contribution to probe noise at low temperature is the presence of DX centers, which add a time-varying potential that affects the 2DEG. A DX center is a deep-level donor defect that can lead to changes in the resistance of the conducting channel [49]. If the conducting channel is wide, contributions from the DX centers average out, minimizing their effect on noise. However, if the channel is thin, DX centers add significant noise to Hall data. We have found empirically that our active area dimension strikes a practical balance between the two competing effects.

Again, in preparation for lithography, we dip the wafer in HCl for 5 s. Photoresist adhesion is crucial for this step, as the small feature etch is delicate and poor resist adhesion typically destroys the conducting channel. After the dip, we spin and bake S1805 photoresist. When the photolithography is complete, we must be thoughtful with photodeveloping. Overdevelopment can extend the insulating features into the active area, killing the probe. Thus, we develop in intervals of 5 – 15 s and check the progress of the development under an optical microscope at each interval. The proper exposure and development appearance are subtle and require experience to recognize. The small yellow cross that appears in the active area, as seen in the right image of Fig. 2.16, indicates proper exposure and development.

Once the wafer has been exposed and developed, the features are ready to be etched. We use the previously mentioned recipe from the cog etch (1:1:78 (by volume) ratio of phosphoric acid, hydrogen peroxide, and water) [46]. For this step, we want to etch through the 2DEG (although we only *need* to etch through the donor layer), but not much deeper. Wet etching removes material laterally, thus etching for too long will extend the insulating arms and destroy the conducting path

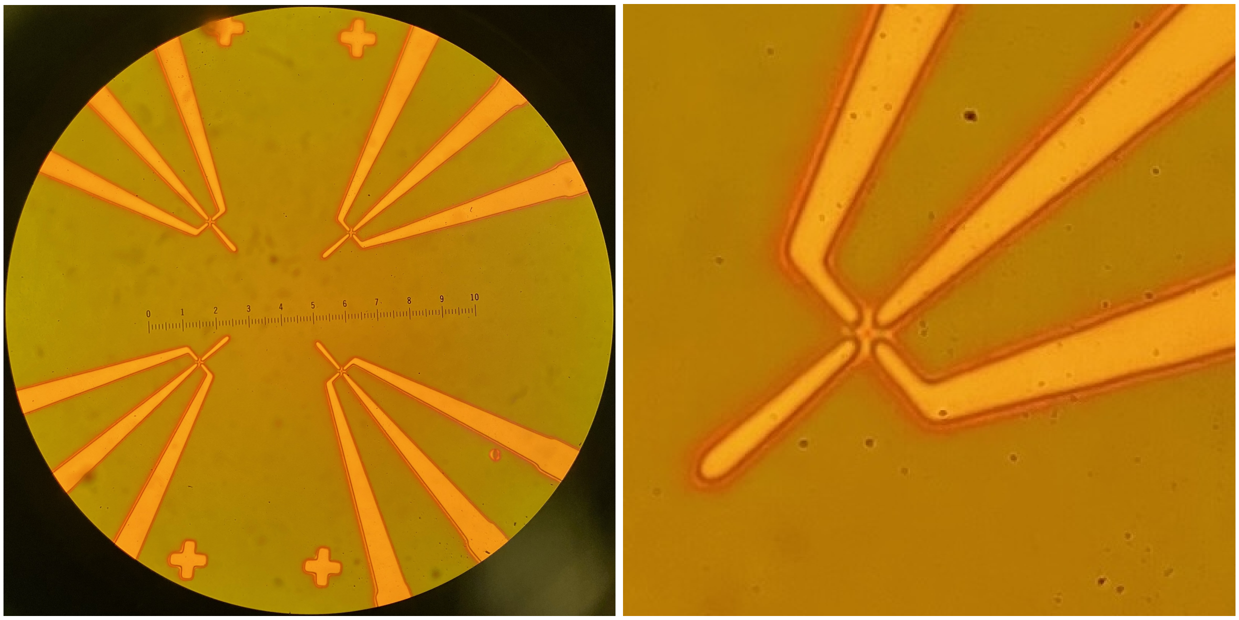

Figure 2.16: Optical microscope images of developed small features ready to be etched. Left picture shows four Hall crosses, small reticle divisions represent 1 µm each. Right image shows a single active area (approximately 1 μm^2) to better bring out the desired yellow cross appearance within the active area that indicates proper development and exposure.

through the active area. Although the dimensions of the active area in the mask are precisely known, subtleties in exposure, development, and lateral etching obscure its true size. Furthermore, sidewall electron depletion effects confine the conducting path by approximately 200 nm [34] on the border of each etched feature. A successful etch is determined with a resistance measurement from a tabletop multimeter. The photoresist is left on the bulk of the square, aside from these small features and exposed areas of the contacts where the photoresist has been scratched away with multimeter probes, allowing for resistance measurements. This allows us to continue etching after measuring the resistance, if necessary. Typical resistance values of approximately 60 – 80 kΩ are somewhat higher than the post-annealing values, as we have confined the conducting path.

2.2.5 Deep Crosses and Probe Separation

The next step is to fabricate two *deep crosses* which electrically isolate the four probes and open a track to scribe and separate them. The first and wider of the deep crosses is 22 µm wide at its thinnest point. The arms of the cross start at the middle of each edge of the square and meet at its center, as shown in Fig. 2.17.

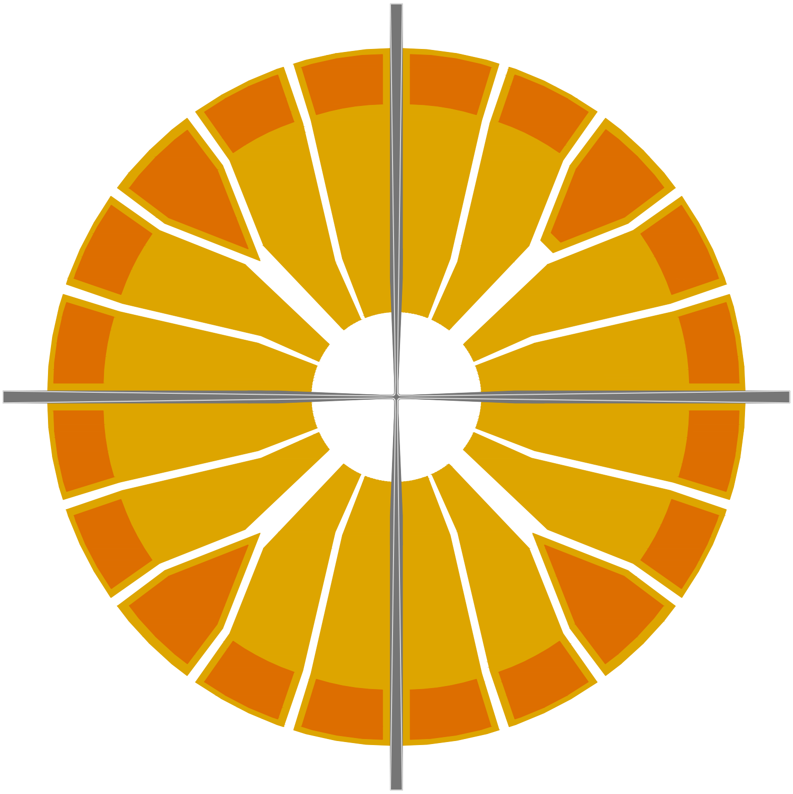

Figure 2.17: Mask design of our deep crosses. Crosses are gray structures that pass through the middle of the wafer and extend to the edges. The wider cross (light gray) is etched first, the thinner cross (dark gray) is etched second.

Again adhesion is critical, prompting the customary HCl dip before photoresist application. Once the pattern is exposed and developed, it should be carefully examined under an optical microscope to confirm that the cross is placed symmetrically with respect to the four active areas as in Figs. 2.18, 2.19. Next, a 30 s O_2 plasma ash is performed to remove photoresist scum before etching.

The deep crosses require a more aggressive etch than that of our insulating features, as they will be etched to a total depth of 1.5 µm, much deeper than the approximately 70 nm insulating features etch. To this end, a mixture of 1:3:50 ratio (by volume) of phosphoric acid, hydrogen peroxide, and water is used to provide an etch rate of approximately 3 nm/s.

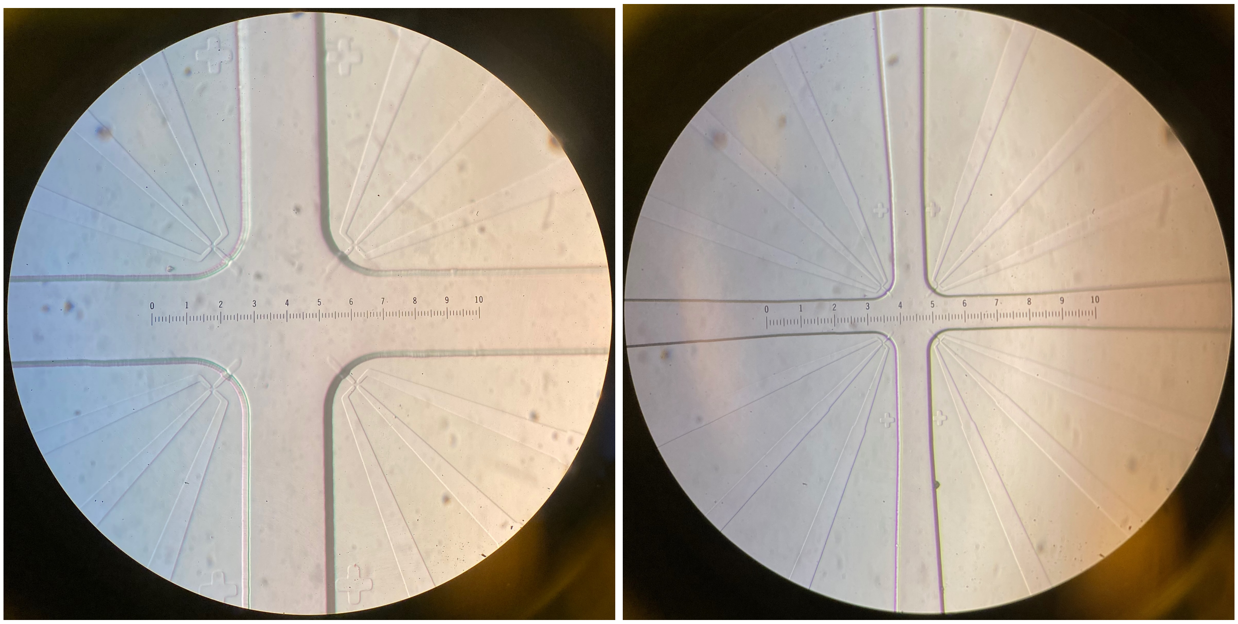

Figure 2.18: Optical microscope images of etched deep cross, highlighting its position with respect to the four active areas. Left photo was taken with 100× objective, small reticle divisions represent 1 µm. Right photo taken with 40× objective, small reticle divisions represent 2.5 µm. Only the first cross has been etched in each of these photos.

Due to the lateral etch profile of wet etching, we implement two deep crosses. The second cross is 16 µm at its thinnest point, and is patterned inside the first as shown in Fig. 2.19. This allows additional etch depth without endangering the active areas. The second cross follows the same method as the first: HCl dip, photoresist spin and bake, lithography, development, careful inspection, plasma ashing, and finally etching. After the second cross is etched, another resistance measurement is made to ensure that the wafer is still conducting through the active area at room temperature.

The last processing step is to cleave and separate the four probes from a square. This scribe needs to be accurate on the order of micrometers to properly separate the probes. The first step is to carefully calibrate the crosshairs in the eye piece to the scriber with a test piece of gallium arsenide. We scribe a line across the test wafer, align the crosshairs to that scribe, and repeat the

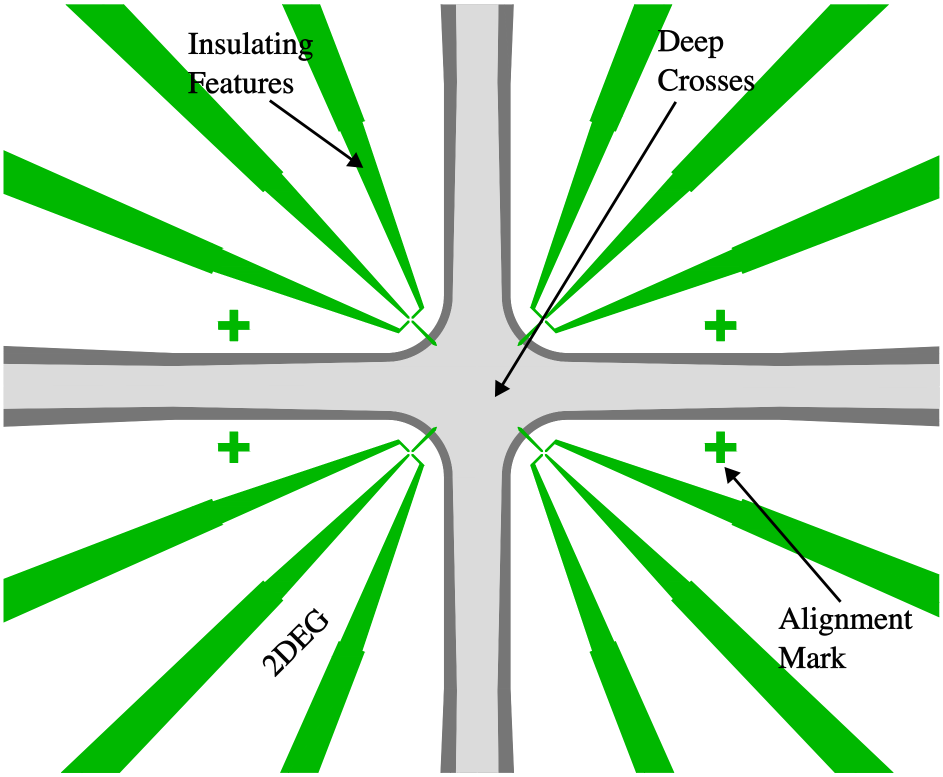

Figure 2.19: Mask design of our deep cross. Crosses occupy the gray region. Insulating features that form the active areas as well as alignment marks for lithographically positioning the deep crosses are pictured in green. The conducting 2DEG is white. The thinnest portion of the inner and outer crosses are 16 µm and 22 µm, respectively.

process. After a few iterations, alignment is sufficiently accurate and we are ready to scribe and separate the real wafer, marking the end of the probe fabrication process.

2.3 Scanning Hall-probe Microscopy System

2.3.1 Cryogenics

Introduction to Open, Closed, and Semi-Closed Helium Cryosystems

Open helium cryosystems, or those for which helium is condensed in a dewar and eventually vented to atmosphere, have a host of advantages over other types of cryosystems [50]. Open systems yield easy access to samples, have low vibrational noise (due to a lack of moving parts), an easily achievable and low base temperature, simplicity in construction, high cooling power, and high temperature stability. However, helium scarcity has been a catalyst for increasing helium prices and conservation efforts [51–54], rendering open systems neither ethical nor economical.

Closed systems conserve helium by circulating it through a sealed path in which it undergoes a cycle of compression, expansion, and heat exchange to achieve cooling. Our system uses a commercial closed-cycle helium pulse tube cryocooler. The cyclic nature of these closed-cycle cryocoolers leads to temperature oscillations of their cold heads on the order of 0.2 K at their cycle frequency [55] (typically around 1 Hz). Our particular cryocooler, Cryomech PT340, has two cold stages (shown in Figs. 2.20, 2.21): the first stage reaches a temperature of 50 K and is thermally connected to a large copper plate in our cryosystem; the second stage is a cold head that reaches 2.8 K and is thermally connected to a smaller copper plate. An optical photo of the stages can be seen in Fig. 2.20. An advantage of this type of cryocooler is that the cold head has no moving parts, limiting mechanical noise [56]. However, the base temperature of the cold head is insufficient for studying a variety of superconductors whose critical temperatures are below 2 K.

To access these lower temperatures, we implemented a semi-closed system that uses the cooling power from our PT403 to cool and liquefy small amounts of externally provided helium that will eventually be vented to atmosphere. In our system, we pre-cool the external helium against the 50 K stage, then liquefy it against the PT403's cold head and collect it in a cylindrical copper reservoir that we call the helium pot. The liquid helium in the pot is pumped to further reduce its temperature to approximately 1.2 K. This process is detailed below.

External Helium Flow

The helium flow process is shown schematically in Fig. 2.21. The external source is ultra-high purity helium (UHP 99.999 %) held in a standard pressurized cylinder (A. in Fig. 2.21). It passes through a mass flow controller (B. in Fig. 2.21) set to a fixed molar flow. The mass flow controller is connected to a stainless steel capillary that enters the vacuum chamber of the cryosystem.

The helium is precooled through a heat exchanger which also acts as a cold trap to remove impurities from the gas (C. in Fig. 2.21). This exchanger is implemented as a cylinder filled with mesh that is linked to the 50 K stage. Next, the helium is further cooled against the cryocooler's

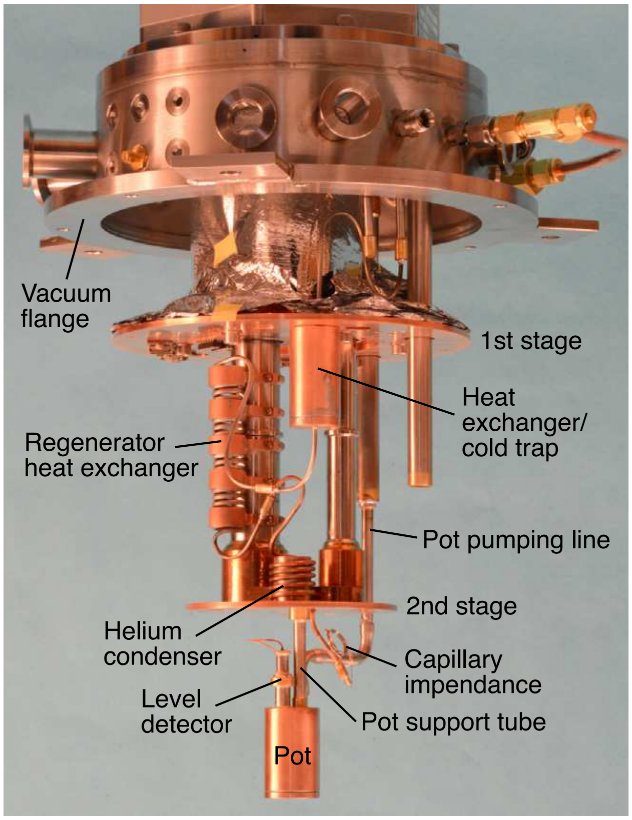

Figure 2.20: Schematic showing the various stages of our cryosystem. An illustration of many of the components highlighted in the helium-flow section. From De Mann, A., Mueller, S., & Field, S. B. (2016). *1 K cryostat with sub-millikelvin stability based on a pulse-tube cryocooler*. *Cryogenics*, **73**, C. Reprinted with permission from Elsevier.

regenerator (D. in Fig. 2.21), allowing for more efficient cooling at the second stage [57]. The helium then travels through a condenser (E. in Fig. 2.21) housed in anchors that are attached to the 4 K stage, reducing the temperature to 5 – 13 K (depending on the flow rate) [57] and liquefying a significant fraction of the helium to eventually collect in the pot. Each of these components are machined from copper due to its excellent thermal conductivity at cryogenic temperatures. Next, the helium passes through a long capillary impedance (F. in Fig. 2.21) with inner and outer diameters of 0.127 mm and 0.25 mm, respectively. This capillary serves as a Joule-Thompson impedance and has a pressure gradient of roughly 1 Bar. The relatively high-pressure helium gas expands as a result of the pressure gradient, further reducing its temperature. Additionally, the thin capillary serves to restrict helium flow. At the end of the capillary, liquid helium drips into the pot (G. in Fig. 2.21), although some helium remains in a gaseous phase, leading to a sputtering effect.

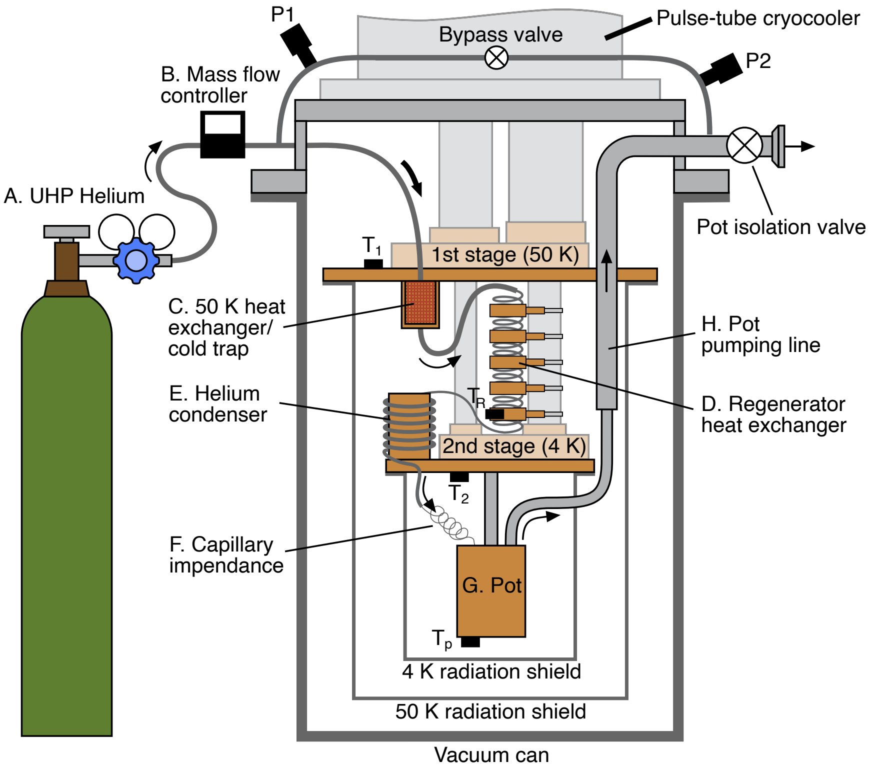

Figure 2.21: Schematic of our semi-closed cryosystem. From De Mann, A., Mueller, S., & Field, S. B. (2016). *1 K cryostat with sub-millikelvin stability based on a pulse-tube cryocooler*. *Cryogenics*, **73**, C. Reprinted with permission from Elsevier.

Figure 2.22 shows an optical photo of the helium pot. As mentioned above, the liquid helium in the pot is pumped externally, lowering its temperature from approximately 2.5 K to 1.2 K. It should be noted that the relatively high specific heat of helium keeps the pot temperature stable to around 25 µK [57], a significant improvement to that of the PT403's cold head. However, this high specific heat leads to a narrow temperature range which is far too restrictive for our experiments. To overcome this, our experimental platforms are a series of removable stages (featured in Sec. 2.3.2) attached to a fixed stage that is only moderately thermally coupled to the helium pot. Figure 2.22 shows the fixed stage to which the removable stages are fixed.

Vacuum Physics

The cryosystem is held at a vacuum to allow efficient cooling and to prevent mechanical noise from the motion of the gas within the system. The system is first pumped with an oil pump and

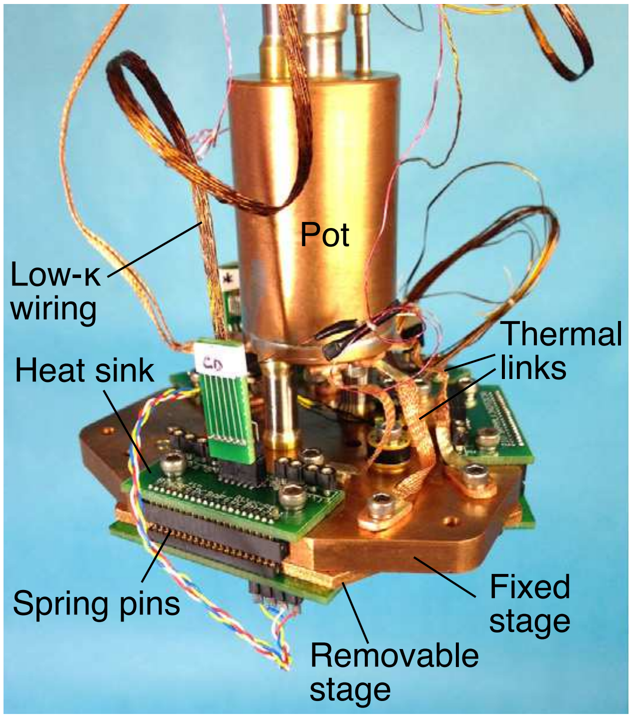

Figure 2.22: Photograph of helium pot connected to the fixed sample stage with removable stage attached below. From De Mann, A., Mueller, S., & Field, S. B. (2016). *1 K cryostat with sub-millikelvin stability based on a pulse-tube cryocooler*. *Cryogenics*, **73**, C. Reprinted with permission from Elsevier.

eventually a turbo pump. Additionally, our radiation shieilds serve as cryopumps, which will be discussed below.

Radiation Shields

The cryosystem and microscope assembly are surrounded by three levels of radiation shielding implemented as concentric aluminum cans (as shown in Fig. 2.21). These shields block electromagnetic noise from sensitive electrical measurements taken in the system. The outermost can interfaces with atmosphere and vacuum on its exterior and interior faces, enclosing the cryochamber. It is sealed to the vacuum flange of Fig. 2.20 with a rubber o-ring. The two inner cans are thermally and physically anchored to the 50 K and 4 K plates, respectively. These inner cans are wrapped with layers of LakeShore NRC-2 superinsulation, a mylar-based material with an exceptional ability to reduce thermal radiation that is commonly utilized in aerospace and cryogenics [58–61]. The inner cans also serve as cryopumps—gas collects on their surfaces through condensation and adsorption processes [62], effectively removing gas from the system and encouraging a very low base pressure when cold.

2.3.2 Removable Sample Stages

Our cryostat is used for a variety of low-temperature applications: transport measurements, thermometry calibration, Hall probe testing, and scanning Hall-probe microscopy. A modular system of removable copper hex plates has been developed, each of which is attached to the fixed stage of Fig. 2.22 with stainless steel screws and thermally linked with Apiezon N-Grease. The plates have access to three 20-pin spring pin banks that contact various instruments. This section will briefly detail each modular plate.

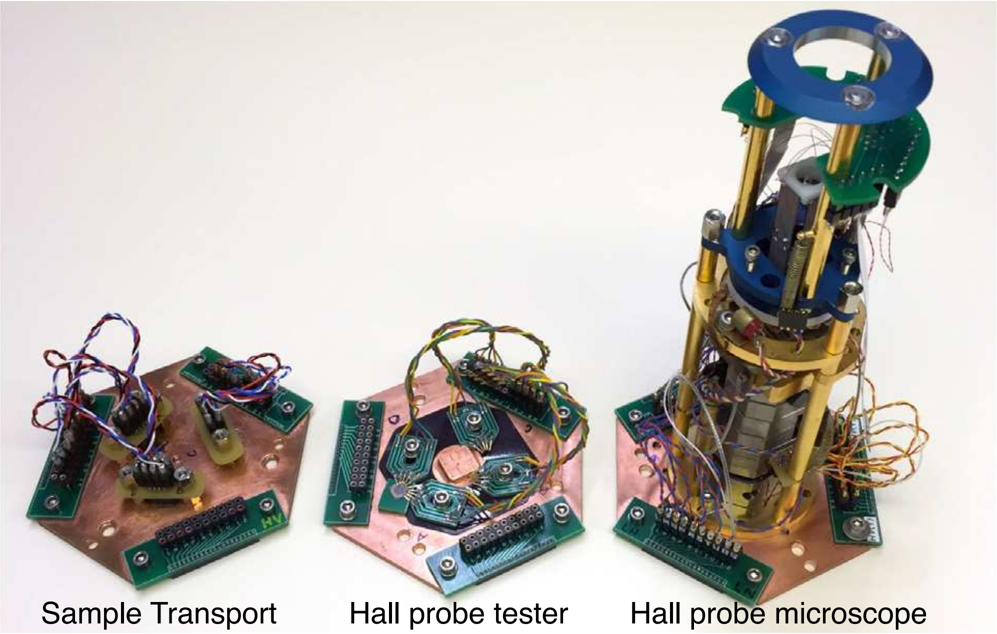

Figure 2.23: Photos of our removable sample stages. The plates pictured here can be used to test noise-performance of Hall probes, make transport measurements, or execute scanning Hall-probe microscopy, respectively. From De Mann, A., Mueller, S., & Field, S. B. (2016). *1 K cryostat with sub-millikelvin stability based on a pulse-tube cryocooler*. *Cryogenics*, **73**, C. Reprinted with permission from Elsevier.

Transport Measurement Jig

The transport measurement jig, the leftmost plate in Fig. 2.23, is used to make transport measurements and calibrate thermometers. In the center of this plate are three sets of posts with custom-machined connectors, each housing four spring pins whose spacing matches that of the four-probe geometry used in our transport structures (Fig. 3.2, for example). The spring pins are fixed to the top surface of the connector with superglue—a sensitive process as any superglue on the shaft of the spring pin will render it immobile. The connectors are machined from clear material for ease in aligning the pins with sample pads. A current source is passed through the outer leads while the inner leads connect to our SR830 lock-in amplifier to measure the associated voltage. Post-processing is conducted to quantify resistance. This setup allows up to three four-probe measurements to be made simultaneously. This jig was used for all the critical temperature and resistance measurements featured in this thesis.

The posts can be removed, and thermometers or sample holders can be screwed or copper taped to the surface for thermometer calibration. The number of simultaneous calibrations that can be conducted is limited only by the physical space on the plate and the three 20-pin spring pin connectors on the fixed stage.

Hall Probe Testing Jig

This plate is pictured in the middle of Fig. 2.23 and has a raised copper platform on which a Hall probe square (consisting of four Hall probes that have not been separated) sits. The square is secured to the platform and electrically connected with four printed circuit boards, each containing four conducting fingers. The fingers are used to apply a current and measure a Hall voltage. The probe is thermally linked to the platform with Apiezon N-grease.

The Hall probe testing process consists of measuring the Hall voltage for an applied field passing through the plane of the probe that switches orientation every few scans. This data is collected as an image of alternating light and dark regions, corresponding to positive and negative fields. Each image is analyzed in IGOR Pro to determine the noise performance and sensitivity of the probes.

Pathologies of daily noise conditions and individual probes lead to Hall frequency- and current-dependent probe performance. For each probe, frequency and current space are explored to find the ideal noise performance. These tests are conducted at 4 K, using no external helium. At this temperature, thermal excitations play a small role in probe noise, making it suitable for testing.

Microscope Assembly

The microscope assembly pictured in the right portion of Fig. 2.23 and in more detail in Fig. 2.24 is used for scanning Hall-probe microscopy. Pictured from top to bottom in Fig. 2.24 are the scanning piezobenders for two-dimensional rastering, the fixtures that house the sample and Hall probe, the Attocube stack, and the spring pin connectors. Throughout this assembly are wiring, printed circuit boards, and connectors that provide the necessary electrical connections to drive microscopy and perform electrical measurements.

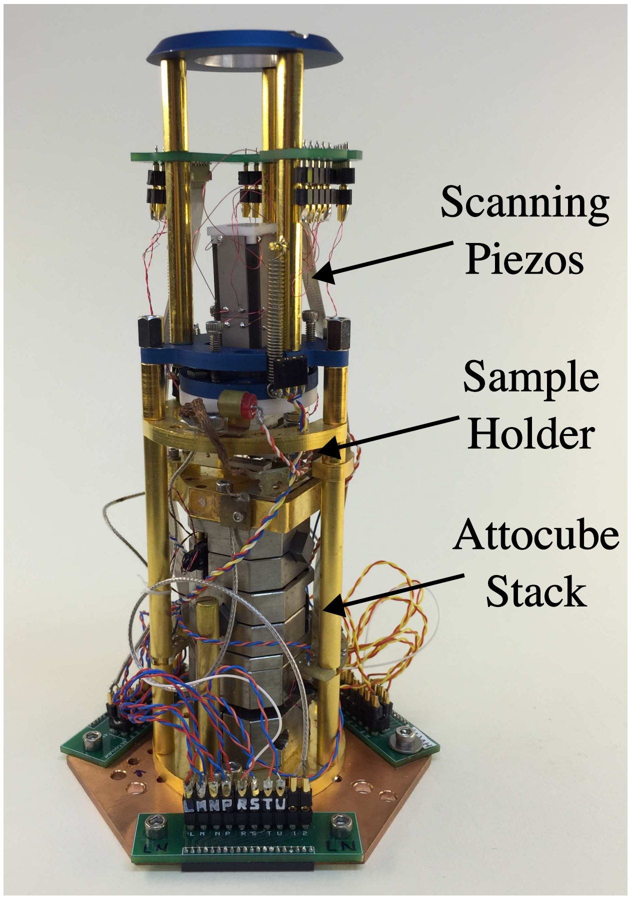

Figure 2.24: Photo of our scanning microscopy assembly

Samples are loaded onto a sample-holding “paddle” before the Hall probe portion of the microscope is attached. The samples are held with gold-plated nickel fingers that are soldered to the surface of the paddles. The paddles feature a small circular copper plate that is situated above a similar plate on the microscope assembly, forming a parallel plate capacitor that is used for position sensing. Paddles also contain thermometery and heaters used for local temperature measurements and temperature-controlling of the sample.

2.3.3 Positioning and Scanning Systems

Discrete Motion

Discrete motion for Hall probe positioning is achieved using Attocube’s ANPxyz100 Nanopositioner, driven by their proprietary nanocontroller (ACN). This system enables precise positioning and operates reliably under extreme conditions, including cryogenic temperatures, high magnetic fields, and high vacuum [63]. The Attocube stack actualizes motion with the stick-slip piezoelectric drive principle. This two-phase method is mediated by friction between a piezoelectric element and a slider, and is driven by a sawtooth voltage pattern. During the stick phase, the piezoelectric element is slowly expanded, moving the slider forward due to static friction. During the slip phase, the voltage is abruptly reduced, resulting in a fast contraction of the piezoelectric element. This causes the piezo to slip with respect to the slider, leaving the slider’s position unchanged [64]. The stick-slip motors are driven at kilohertz frequencies, providing millimeter-scale movements as a succession of small steps. Our attocube stack has three stick-slip motors positioned in orthogonal directions giving us x, y, and z control and a positioning range of 6 mm × 6 mm × 7 mm [63].

Scanning Piezobenders

Although the nanopositioner provides an accurate positioning system, it lacks the smooth motion desired to raster during a scan. Scanning is performed with a piezoelectric bender system as seen in Fig. 2.25. Our standard scan head can sweep a 60 µm × 60 µm square in the plane of the sample. The system is composed of two piezo benders for planar scanning, one piezo bender for vertical motion, a fixed base, a scanning stage, and a second stage. The stages and base are made of Macor, an easily machinable material whose thermal contraction is similar to that of the piezoelectric material. As can be seen in Fig. 2.25, the x- and y-piezo scanners are bisected in their vertical midsection—the electrodes are oriented oppositely for the top and bottom segments, producing an "s" shape when scanning. This keeps the ends of the scanner perpendicular to the scanning direction (and the fixed Macor bases) [65], allowing coplanar movement of the column with respect to the fixed base. There is also a piezobender associated with motion orthogonal to the scan plane, what we refer to as z-motion (vertical in Fig. 2.25). This allows the Hall probe to be set to a fixed height, lowered to touch the surface, or backed away from the surface to prevent a collision between the Hall probe and a sample.

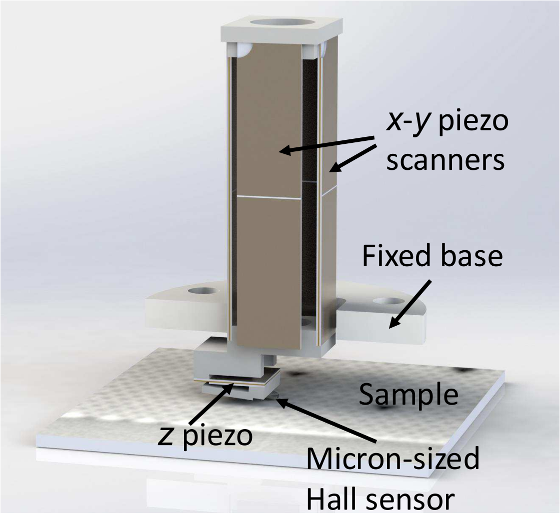

Figure 2.25: Diagram of our piezobender scanning system. Fixed base fixes piezoscanners and probe to the microscope assembly. x- and y-piezo scanners used to raster and z-piezo to raster tip of probe.

A "compensator program" allows us to define a sample surface plane by gently touching the Hall probe to the surface at a variety of points across a grid. The parallel-plate capacitor used for sample position sensing is sensitive to small capacitance changes caused by paddle flexion upon contact. These changes trigger the z-piezo to fully retract. Once the surface plane has been defined, the voltage to the z-piezo is automatically adjusted to maintain a constant scan height. This is important as the samples are generally not flat on the micrometer scale. Compensation allows us to avoid false signals from an uneven scan plane and prevents the probe from crashing into the surface.

Having introduced scanning Hall probe microscopy, detailed the probe fabrication process, and described our cryogenic, positioning and scanning systems that enable SHPM, we now turn to our magnetic imaging studies of superconductors and chirality-induced spin-selectivity materials.

Chapter 3

Trapped Flux and Vortices in Superconducting Aluminum Rings

> “Through measurement to knowledge”
>
> —Heike Kamerlingh Onnes

3.1 Introduction

The mixed state of type II superconductors is of fundamental scientific interest in condensed matter physics. This work investigates the equilibrium state of a type II superconducting thin-film ring as a function of applied magnetic field—focusing on the interplay between fluxoids resulting from azimuthal currents in the ring itself and those due to superconducting vortices hosted in the bulk of the ring. The magnetic signatures associated with fluxoids make high-resolution magnetic imaging a powerful tool for probing these systems. Our method detailed in this chapter produces magnetic images in addition to magnetic field measurements at the ring’s center. This twofold approach helps avoid ambiguity in interpreting our results, an issue that has burdened similar experiments [4]. In the words of Simon Bending [34], "A great deal of information concerning the magnetic properties of superconductors can be gained from bulk measurements including magnetization, transport and heat capacity; yet it is virtually impossible to interpret such data fully without a microscopic picture of flux structures and dynamics."

While a wealth of magnetic imaging studies have focused on the fluxoids’ response to the applied magnetic field for thin-film strips [66–68], the present work examines the topologically distinct geometry of a ring. Recent efforts to image the mixed state in a thin-film MoGe ring using a scanning quantum interference device (SQUID) magnetometer [69] (see Fig. 3.1) demonstrated the dependence of the first critical field on the ring’s geometry, as well as the linear relationship between vortex density and applied magnetic field. We conducted a more detailed study of fluxoid evolution on a smaller ring using complementary techniques and higher spatial resolution for imaging. There is a trade-off between magnetic field sensitivity and spatial resolution in various magnetic imaging schemes. For example, scanning SQUID microscopy offers much higher field sensitivity and Lorentz microscopy yields much higher spatial resolution [34]. SHPM fills an intermediate space with convenient spatial and field resolution for studying vortices [35, 67, 70–76].

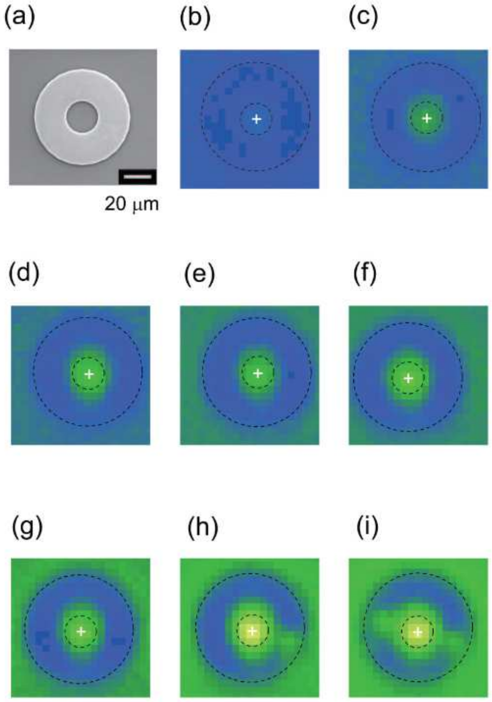

Figure 3.1: Scanning SQUID microscopy images of a MoGe ring with an inner diameter of 10 μm, an outer diameter of 34.5 μm, and thickness of 210 nm after cooling to 4.0 K in different magnetic fields of (b) 20, (c) 30, (d) 40, (e) 50, (f) 60, (g) 70, (h) 80, and (i) 90 μG, respectively. All images have a scan range of 84 μm × 84 μm. Electron micrograph of the ring is given in (a). From N. Kokubo, S. Okayasu, and T. Nojima, "Finite-size effect of critical penetration of Pearl vortices in narrow superconducting flat rings," *J. Appl. Phys.* **125**, 223906 (2019). Reprinted with permission from AIP Publishing.

The general behavior of a thin superconducting ring can be understood by appealing to the previous discussion on the Meissner effect and London's fluxoid. Below its critical temperature, the ring enters a superconducting state. The introduction of a small applied field is met with superconducting screening currents that facilitate the Meissner effect. As that applied field is increased, the energy due to the screening currents increases proportionally until the first fluxoid enters the system. For our geometry, the first fluxoid is hosted in the center of the ring, raising the winding number by one. The currents associated with increasing winding number flow in the opposite direction to the Meissner screening currents, so this change in winding number lowers the overall current and energy of the system. This process of increasing Meissner currents and periodic jumps in winding number persists to the first critical field H_1. As the field increases above H_1, the ring allows flux penetration through nucleated vortices in the metal of the ring itself. For the purposes of this discussion, fluxoids hosted in the center of the ring will be called a fluxoid N, and those hosted in superconducting vortices will be referred to as vortices m.

To predict the behavior of our system, we constructed a theoretical and numerical framework. Previous efforts quantified magnetic fields, sheet-current profiles, and magnetic flux for thin-film rings exposed to perpendicular magnetic fields with negligibly small penetration depths [77]. Later, this was generalized for any ring in the thin-film or Pearl regime, with an effective penetration depth, the *Pearl length*, $\Lambda = 2\lambda^2/d$ [78]. In this limit, the current density variations in the vertical direction are negligible and $\mathbf{H}$ penetrates the entire ring nearly uniformly. Our approach to this problem was informed by previous work on fluxoid behavior for thin-film type II superconducting rings by Kogan, Clem, and Mints KCM [79]. Here, the authors developed an expression for and subsequently minimized the *magnetic Gibbs free energy* of the system. They specified the equilibrium state as the number of fluxoids hosted in the center of the ring, the presence or lack thereof of a *single* nucleated vortex in the bulk of the ring, and the radial position of that vortex. We extended their approach to allow for any integer number of nucleated vortices.

3.2 Rings

To fabricate the rings, we spun and baked Shipley's S1805 photoresist and LOR3B lift-off resist on a 6 mm × 6 mm silicon wafer. LOR3B (1.3 μm) is much thicker than S1805 (0.5 μm) and is used to ensure a clean liftoff after metal growth (as detailed in Chap. 2, see Fig. 2.12). We then photolithographically defined and developed a ring pattern and four-probe transport geometry.

After an oxygen plasma ash to remove photoresist scum, the patterned substrates were loaded into our argon magnetron sputtering chamber. The rings and transport structure were simultaneously sputtered to a thickness of 210 nm from a pure aluminum target. During the sputtering process, a partial pressure of approximately 20 µTorr of oxygen was bled into the chamber. This oxygen environment is key in producing *granular aluminum* [80], a type II superconductor composed of pure aluminum grains separated by a thin aluminum oxide layer. Granular aluminum is a natural material for our rings due to its tunable T_c that is convenient for the base temperature of our cryosystem [81] and its extremely low vortex pinning [80]. The aluminum grain size of approximately 15 nm [80, 82] is very small with respect to the Ginzburg Landau coherence length ξ of the material [83]. ξ sets the physical size of a vortex, thus granular aluminum is a uniform medium from its perspective, making pinning very weak. This ensures that vortices are free to arrange themselves on the basis of magnetic interactions and sample geometry rather than being forced into strong pinning sites. As we examine the experimental results, we will see evidence of this low pinning.

The transport geometry shown in Fig. 3.2 provides a method to measure the normal-state resistivity just above the transition temperature, a useful metric for confirming the uniformity and quality of our granular aluminum films. Four-probe measurements are the industry standard for measuring small resistances. When a two-probe resistance measurement (e.g., using a table top ohmeter) is performed, the resistance associated with the system's wiring and various contact resistances will be measured. This introduces uncertainty because these extraneous resistances can be significant with respect to the sample's resistance. The key to a four-probe transport measurement is the design of voltmeters. They are high impedance, thus they draw minimal current from the circuit being measured. We apply current to the outer leads, measure the voltage difference across the inner leads, and invoke Ohm's law to find the resistance. Consideration of the transport structure's geometry reveals the resistivity. This structure allows for the measurement of additional important characteristics of our films, including T_c and the transition width, as shown in Fig. 3.3. Those parameters allow us to calculate a host of other properties such as Ginzburg Landau penetration depth, Ginzburg Landau coherence length, London penetration depth, etc., which are displayed in Table 3.1. These measurements were conducted with the transport measurement hex plate featured in Sec. 2.3.2.

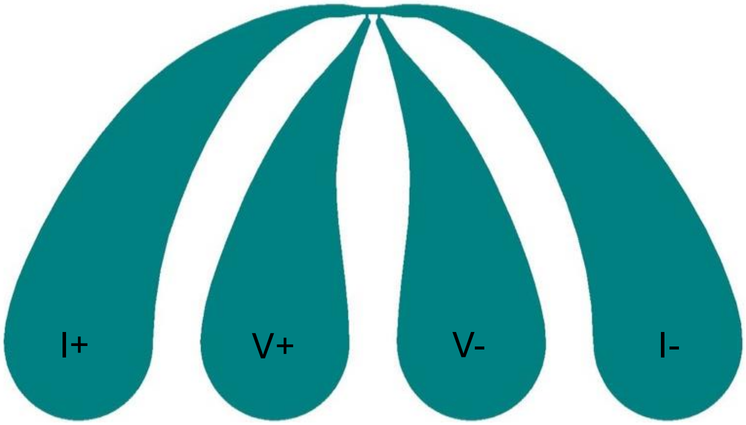

Figure 3.2: A schematic of the four-probe transport structure geometry with labeled leads. The large teardrop-shaped leads are designed to electrically contact the spring pins of Fig. 2.23.

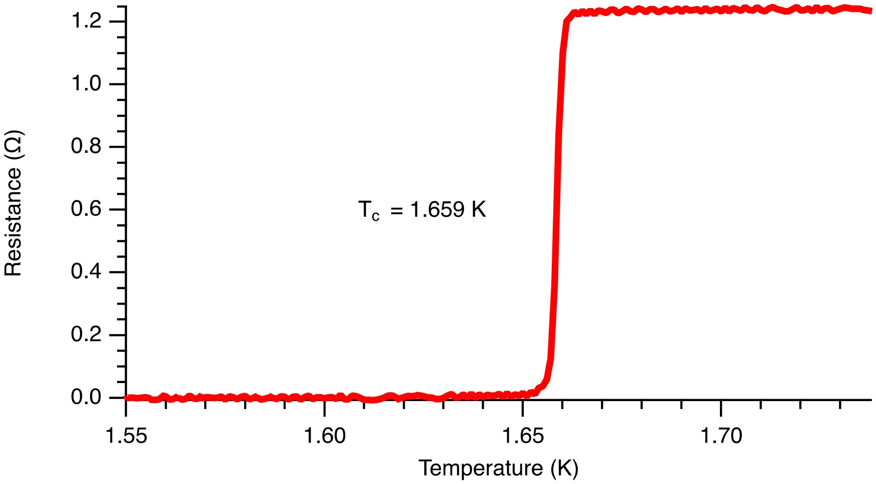

Figure 3.3: Four-probe resistance as a function of temperature for transport structure grown simultaneously with aluminum rings. Note the sharp drop to zero resistance at approximately 1.66 K.

Our ring pattern featured 36 rings of various dimensions. Incomplete liftoff of the inner hole was a common mode of failure, so sputtering 36 rings ensured that we had many high-quality rings

Table 3.1: A table of properties of our aluminum rings that were measured or calculated. Narrow transition width indicates unifrom film and κ places the rings firmly in the type II superconducting regime.

Parameter	Symbol	Value
Critical temperature[a]	T_c	1.659 K
10%–90% transition width[a]	ΔT_c	3 mK
Resistivity[a]	ρ	13.5 μΩcm
London penetration depth [b]	λ_L	15.7 nm
GL coherence length[b]	$\xi(T)$	$50\,\mathrm{nm}/(1 - T/T_c)^{1/2}$
GL penetration depth[b]	$\lambda(T)$	$190\,\mathrm{nm}/(1 - T/T_c)^{1/2}$
GL parameter[b]	κ	3.8

Measured values are denoted with a, calculated values with b.

to choose from. After the liftoff, the rings were inspected under an optical microscope as shown in Fig. 3.4 and the best candidates were considered for the experiment. We chose a ring whose inner and outer diameters were 2.4 μm and 5.0 μm, respectively.

3.3 Theory

The KCM treatment is only valid in the thin-film limit for which $\Lambda \gg d$, so a necessary first step is to confirm that relationship. As our system cools below T_c, it quickly reaches its *freezeout temperature* T_f, the temperature at which the vortex configuration becomes fixed. At T_f, thermal fluctuations become smaller than the characteristic energy scales associated with fluxoids and vortices, effectively stopping the system from exploring phase space. Thus, despite imaging well below T_f, the fluxoid and vortex configurations correspond to a temperature much closer to T_c. We do not have a method to directly measure T_f; however previous experiments on mesoscopic aluminum rings by Davidovíc *et al.* [84] show that it is some 10 mK below T_c. Then for our rings,

$$\Lambda = \frac{2\lambda^2(T_f)}{d} = \frac{2(190\,\mathrm{nm})^2}{210\,\mathrm{nm}} = 57\,\mu\mathrm{m}, \tag{3.1}$$

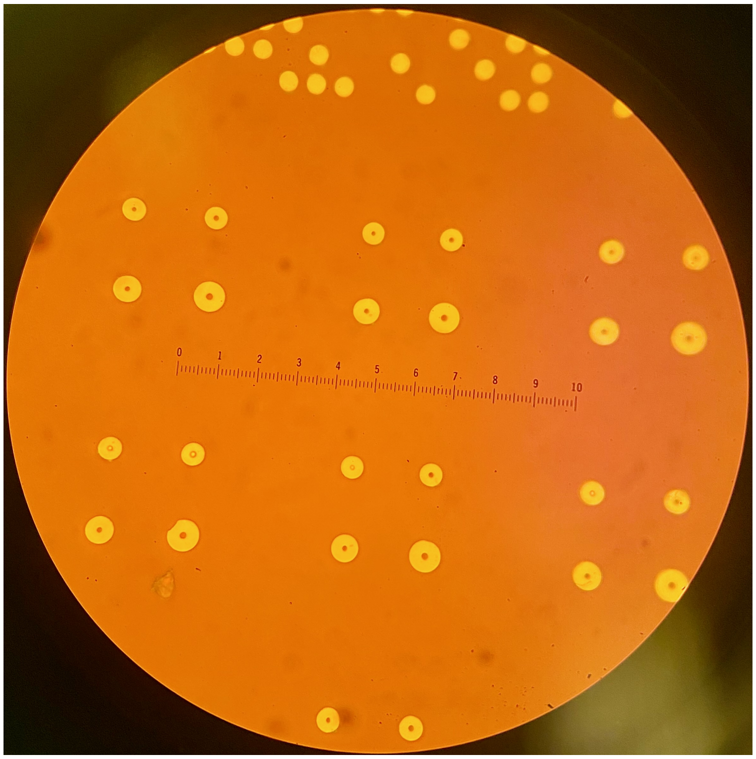

Figure 3.4: Optical photo of a subset of the 36 ring array. Small reticle divisions represent 1 µm. This photo was taken after liftoff and incomplete liftoff of ring centers as well as asymmetric ring structures can be seen. This array was surveyed for an ideal ring for the experiment. The de Bruijn structure for scanning is pictured above the rings as a series of smaller disks.

satisfying the condition of KCM.

KCM used London theory to develop an expression for the *magnetic Gibbs free energy* $\mathcal{F}(N, v, H)$ of a thin-film ring as a function of the number of fluxoids N, radial vortex position v, and applied field H. The magnetic Gibbs free energy is the appropriate thermodynamic potential to consider as it corresponds to systems at constant temperature and pressure in the presence of an applied field, aligning with our experimental conditions. KCM showed that minimizing $\mathcal{F}$ with respect to N, v gives the equilibrium state of the system for a given applied field, H, with or without a single vortex [79]. We will follow the same approach; however, we will develop our own $\mathcal{F}(N, m, v, H)$ that allows the introduction of m vortices.

3.3.1 Stream Function

KCM began by defining the *stream function* $G(\mathbf{r})$ from which the superconducting sheet current density $\mathbf{g}$ can be derived as

$$\mathbf{g} = \boldsymbol{\nabla} \times (G\hat{z}). \tag{3.2}$$

In the Pearl limit, the Amperian field generated by supercurrents in the ring is negligible compared to the applied field H [79], and thus can be ignored. Then we can write a simplified London equation for multiple vortices as

$$\frac{2\pi\Lambda}{c}\nabla^2 G = \mp\phi_0 \sum_{k=1}^{m} \delta(\mathbf{r} - \mathbf{v}_k) + H, \tag{3.3}$$

where v_k represents the position of the vortices. Equation 3.3 is linear, so we can solve for the contribution from the currents that respond to the applied field G_H and those associated with the vortices G_v separately. These constituents of G must satisfy

$$\nabla^2 G_v = \mp\frac{c\phi_0}{2\pi\Lambda} \sum_{k=1}^{m} \delta(\mathbf{r} - \mathbf{v}_k), \tag{3.4}$$

$$\nabla^2 G_H = \frac{c}{2\pi\Lambda} H. \tag{3.5}$$

Informed by the approach of KCM, we found that

$$G_H(r) = \frac{cH}{8\pi\Lambda} r^2 - \frac{c\phi_0}{4\pi^2\Lambda} \ln\frac{r}{a}\left[N + m\frac{\ln(b/v)}{\ln(b/a)}\right]. \tag{3.6}$$

An encouraging aspect of Eq. 3.6 is that we match KCM's stream function due to the applied field upon setting $m = 1$. Interestingly, G_H has *N and m* dependence. That is, despite breaking our stream function into a part due to the applied field and a part due to the vortices, the presence of vortices affects both. It is worth noting that we are assuming that all m vortices are sitting at the same radial position v in Eq. 3.6. *Buckling effects* [85] can be neglected until vortex density is higher than that of our experiment or numerical project. Aligning with intuition, upon moving a vortex from the outer edge ($v = b$) to the inner edge ($v = a$), N increases by one according to Eq. 3.6.

To quantify G_v, a method from Morse and Feschbach [86] was used, mapping our ring to an analogous electrostatic system. We first developed an expression for one nucleated vortex at azimuthal angle θ_v, and then modified G_v to account for an arbitrary number of equally spaced vortices, m. For one vortex,

$$G_v^{(1)}(\rho,\theta,v,\theta_v) = \frac{c\phi_0}{4\pi^2\Lambda}\mathrm{Re}\left[\ln\frac{\sin[\pi\ln(vw/a^2)/2\ln(b/a)]}{\sin[\pi\ln(v/w)/2\ln(b/a)]}\right], \tag{3.7}$$

where $w = \rho e^{i(\theta-\theta_v)}$. To account for m nucleated vortices (equally spaced by angle θ_v), we can sum the G_v solutions as follows,

$$G_v(\rho,\theta;v) = \sum_{\theta_i} G_v^{(1)}(\rho,\theta;v,\theta_i). \tag{3.8}$$

Now that G_H and G_v have been developed, we have an expression for the overall stream function $G = G_H + G_v$. Throughout our theoretical work, we consistently checked our results with those of KCM by setting $m = 1$. We were able to match their expressions, lending confidence in our method.

3.3.2 Energetics

Having established a stream function, we can analyze the energetics of our system. We will start by considering the zero-field free energy—the energy due solely to circulating currents from trapped fluxoids and those associated with vortices. In the absence of an applied field, the energy can be broken down into magnetic and kinetic contributions [79]. KCM showed that

$$E(N,v) = \varepsilon_v(v) + \varepsilon_0\left(N \pm \frac{\ln(b/v)}{\ln(b/a)}\right)^2, \tag{3.9}$$

where

$$\varepsilon_0 = \frac{\phi_0^2 \ln(b/a)}{8\pi^2 \Lambda}$$

is a convenient energy scale for fluxoids and vortices. In their expression, ε_v is the self-energy of a vortex and the second term is the energy associated with the interaction between the currents due to the fluxoids and those associated with a vortex. Appealing to the work of Morse and Feshbach [86] and using a small-angle approximation, KCM showed that the self-energy can be expressed as

$$\varepsilon_v = \frac{\varepsilon_0}{\ln(b/a)} \ln\left[\frac{wv \ln(b/a)}{\pi\xi} \sin\frac{\pi \ln(v/a)}{\ln(b/a)}\right], \tag{3.10}$$

where the coherence length ξ has been used as a cutoff of the diverging current density near the vortex core. Again, we will modify their approach to allow for any number of vortices. Equation 3.10 is simple to adapt as we need to consider the energies of m nucleated vortices, which can be achieved by multiplying this expression by m. Similarly, the second part of the N, m interaction term of Eq. 3.9 needs to be multiplied by m to account for each vortex. Making those changes and adding an additional term yields

$$E(N, v, m) = m\varepsilon_v(v) + m\varepsilon_{vv}(v, m) + \varepsilon_0 \left(N \pm m\frac{\ln(b/v)}{\ln(b/a)}\right)^2. \tag{3.11}$$

The new term in Eq. 3.11, ε_{vv}, is the vortex-vortex interaction energy. It is proportional to the value of the stream function at the position of one vortex due to the presence of the other vortices,

$$\varepsilon_{vv} = \frac{\phi_0}{2c} \sum_{\theta_i \neq 0} G_v(v, 0; v, \theta_i). \tag{3.12}$$

As was previously mentioned, the equilibrium state of the ring can be found by minimizing the magnetic Gibbs free energy. There is a simple thermodynamic relationship that can be integrated to quantify $\mathcal{F}$,

$$\delta\mathcal{F} = -\boldsymbol{\mu} \cdot \delta\mathbf{H} = -\mu\delta H. \tag{3.13}$$

Appealing to the definition of magnetic moment, we have

$$\mu_z(N,m,v,H) = \frac{\phi_0}{8\pi\Lambda}\left[N(b^2-a^2)+m(b^2-v^2)\right] - \frac{H}{16\Lambda}(b^4-a^4). \tag{3.14}$$

Integrating Eq. 3.13 with respect to the applied field H and using the zero-field energy (Eq. 3.11) as our constant of integration,

$$\begin{aligned}\mathcal{F}(N,m,v,h) &= m\varepsilon_v(v) + m\varepsilon_{vv}(v,m)\\ &\quad + \varepsilon_0\left(\left(N+m\frac{\ln(b/v)}{\ln(b/a)}\right)^2 - 2h\left(N+m\frac{b^2-v^2}{b^2-a^2}\right)+\frac{b^2+a^2}{b^2-a^2}\ln(b/a)h^2\right).\end{aligned} \tag{3.15}$$

Here, h is a dimensionless magnetic field introduced by KCM as $h = H/H_0$, with

$$H_0 = \frac{2\phi_0\ln(b/a)}{\pi(b^2-a^2)}.$$

Equation 3.15 serves as the quantity to be minimized during our numerical project to be detailed in Sec. 3.4.

3.3.3 Magnetic Field at Ring Center

Our SHPM system is well suited to measure the magnetic field along the axis of the ring and at its center B_z. Developing a theoretical framework for B_z provides a second method to compare with experiment. As was previously mentioned, this will help avoid ambiguity in analyzing fluxoid behavior. Furthermore, our ability to resolve the number of nucleated vortices in scanning images is limited by the spatial resolution of the Hall-probe, while this B_z measurement allow us to detect changes in m at much higher vortex densities.

The Biot-Savart law is a useful means of calculating the magnetic field due to a current distribution. We will consider the field in the center of the ring and at its surface ($z = 0$) due to some current density $\mathbf{g}$. Let $\mathbf{r}$ start at the center of the ring and end at $\mathbf{g}$. According to the

Biot-Savart law,

$$\mathbf{B}(\mathbf{r}) = -\frac{1}{c}\int \frac{\mathbf{g}\times\mathbf{r}}{r^3} d^2r. \tag{3.16}$$

Our approach is similar to that employed by KCM to calculate the total current I by breaking g_ϕ into its azimuthal average for $r > v$ and $r < v$, separately. Here, we only need the z component of B, thus the cross product can be evaluated as $(\mathbf{g}\times\mathbf{r})_z = -rg_\phi$ where g_ϕ is the azimuthal component of $\mathbf{g}$,

$$B_z = \frac{1}{c}\int_a^b \int_0^{2\pi} \frac{rg_\phi(r,\phi)}{r^3} rdrd\phi \tag{3.17}$$

$$= \frac{1}{c}\int_a^b \int_0^{2\pi} \frac{g_\phi(r,\phi)}{r} drd\phi = \frac{1}{c}\int_a^b \frac{1}{r}\left[\int_0^{2\pi} g_\phi d\phi\right] dr. \tag{3.18}$$

The bracketed term is $2\pi\bar{g}_\phi(r)$, where $\bar{g}_\phi(r)$ is the azimuthal average of $\mathbf{g}$,

$$B_z = \frac{2\pi}{c}\left[\int_a^v \frac{\bar{g}_{r<v}(r)}{r} dr + \int_v^b \frac{\bar{g}_{r>v}(r)}{r} dr\right]. \tag{3.19}$$

Evaluating these integrals and defining a dimensionless magnetic field gives

$$b_z \equiv \frac{2\pi\Lambda b}{\Phi_0} B_z = -\frac{2\ln(b/a)}{1+a/b} h + \left(\frac{b}{a} - 1\right) N + \left(\frac{b}{v} - 1\right) m \tag{3.20}$$

Plugging in our a, b and letting $v = \frac{a+b}{2}$ (which will be shown to be a reasonable approximation) leaves us with

$$b_z = -.992h + 1.083N + .351m, \tag{3.21}$$

a simple expression that can be compared to our experimental results.

3.4 Numerical Analysis

To begin our numerical project, the appropriate values for a, b, ε_0 and ϕ_0 were specified. In order to evaluate the zero-field energy (Eq. 3.11), we first needed to define the self-energy of a vortex (Eq. 3.10), and the vortex-vortex interaction (Eq. 3.12). Next, the magnetic moment (Eq. 3.14) was defined and used to integrate the thermodynamic relationship (Eq. 3.13) with the zero-field energy (Eq. 3.11) as the additive constant. This final numerical expression for $\mathcal{F}$ was used to calculate the magnetic Gibbs free energy for any combination of N, m, v, and h.

The next step was to minimize $\mathcal{F}$. To this end, a series of nested loops were implemented to step through values of N, m, and v for a given h with resolution and bounds of our choice. The first decision made was the range of h, as other parameters depend on the applied field. We let h run from 0 to 7. Recall $H = h \times H_0$ and filling in our values for a, b, ϕ_0 gives $H \approx 2.2$. Thus, our chosen range of H probes approximately $0 - 15.3\,\mathrm{G}$, aligning with the applied field range of our imaging experiment. It was decided to let N and m vary from 0 to 25 since the limits of our hall probe resolution would obscure m before that upper limit. The final range to set was v—any nucleated vortex must appear in the bulk of the ring, naturally restricting its radial position. We also needed to decide on the resolution for the variation of these parameters. N and m are limited to integers. The calculation time depended significantly on the resolution of v and H. Ultimately, for high-resolution plots needed for comparison with experiments, we decided on approximately 20 nm increments for v and 15 mG increments for H.

To perform minimization for a given h, nested loops were used to calculate $\mathcal{F}$ for each possible value of N, m, and v. The lowest value of $\mathcal{F}$ and the associated values of N, m, and v were stored in arrays along with h. These solutions were used to produce graphs of N, m vs. h, v vs. h, and $\mathcal{F}$ vs. h, each of which are helpful for understanding the equilibrium state of the system.

In Fig. 3.5 we plot $\mathcal{F}/\varepsilon_0$ vs. h for all values of N and m that lead to a free energy within the graph boundaries. The minimum value of $\mathcal{F}$ at each value of h is shown in blue. Before the first critical field H_1, oscillations in $\mathcal{F}$ correspond to additional fluxoids hosted in the center of the ring. The behavior of $\mathcal{F}$ changes dramatically as h exceeds H_1. At this point, partial flux penetration via nucleated vortices allows lower energy costs associated with increasing field. This behavior persists until h reaches H_2, which is beyond the range of our simulation.

Figure 3.6, constructed from the minimum values of $\mathcal{F}$ in Fig. 3.5, is particularly useful for comparison with the experiment, as it predicts the number of fluxoids and vortices for a given field.

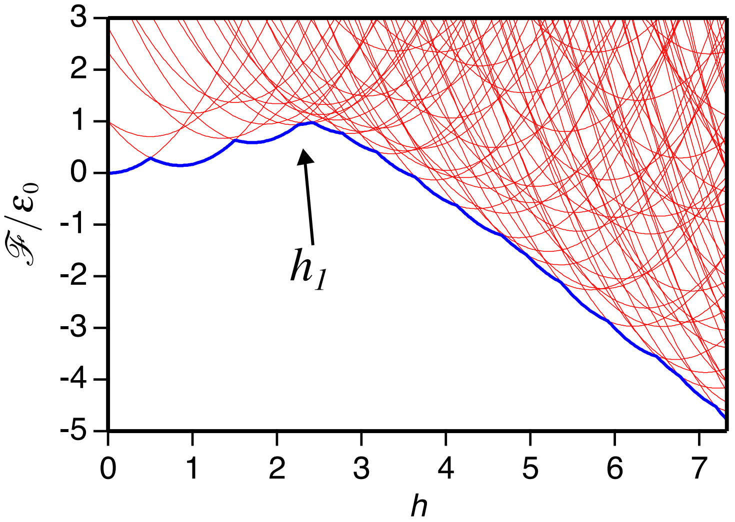

Figure 3.5: Magnetic Gibbs Free-energy contours as a function of h for many values of N and m, calculated from Eq. 3.15. Blue contour is the minimum free energy for each point in h.

The lower panel shows that the winding number N increases twice before the first vortex enters the bulk of the ring. h_1 is the first field at which the ring can lower its energy by nucleating a vortex (at $h \equiv h_1 \approx 2.2$). Beyond h_1, the magnetic Gibbs free energy is arbitrarily lowered by nucleating more vortices until the vortex-vortex interaction becomes significant. This interaction is exponentially small until the spacing between vortices approaches the width of the ring ($W = b - a$); from our simulation this appears to be around $m = 4$. h_1 depends on the geometry of the system [67]—a wider ring would allow vortices to nucleate at a lower field while a thinner ring would require larger fields to nucleate a vortex. The inset of Fig. 3.6 shows the evolution in N and m for a coherence length ξ of 0.50 µm, revealing a consequential decision in our numerical project. The main plot was generated with $\xi = 0.45$ µm. As we can see, the evolution of N and m varies substantially with a modest change in ξ. The value of the first critical field depends on the coherence length via the relationship $H_1 \approx 2\Phi_0/\pi W^2 \ln(2W/\pi\xi)$, thus we have a method of calculating ξ which is based on our experimental results. $\xi = 0.45$ µm best fit our data featured in Sec. 3.5. It is worth pointing out that the accuracy of ξ is naturally limited by the accuracy of our first critical field measurement. As will be discussed in Sec. 3.5, we operated in increments of 100 mG, but our numerical project might have matched reality better if we honed in on H_1 with higher field resolution. The upper panel of Fig. 3.6 shows a sharp jump in the radial position of the vortices with each successive vortex nucleation, indicating a reduction of mutual magnetic repulsion with increased vortex spacing. Additionally, it shows that v is well approximated by $(a+b)/2$, justifying the approximation used in Eq. 3.21. Figure 3.6 will be examined in more detail in Sec. 3.6.

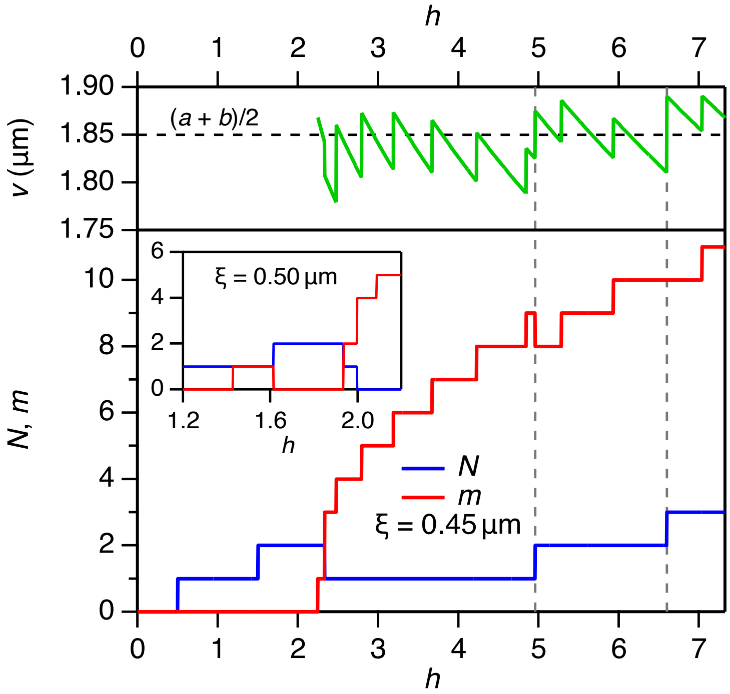

Figure 3.6: Evolution of N (blue), m (red), and v (green) in h for various ξ. Upper panel shows radial vortex position v as a function of h.

These plots serve as a summary of our theoretical and numerical predictions and will be extensively compared with experimental results in Sec. 3.6.

3.5 Experiment

In our experiment, the equilibrium state of the ring as a function of applied field was measured using two distinct methods. First, we took detailed magnetic images of our rings with our SHPM. The image quality was of utmost importance, so images were taken as close to the surface of the ring as was safe, and at a fraction of our typical scanning range. Then, the magnetic field at the ring's center was measured by carefully aligning the Hall probe above the center of the ring and scanning horizontally. Importantly, for either method the ring was heated above T_c, the field was applied, and the ring was cooled back through its transition temperature before each scan. This *field-cooling* presumably ensured that our system was in its equilibrium state.

3.5.1 Magnetic Images

Magnetic images were taken with a scan range of 13.5 µm and at a vertical distance of 0.5 µm above the ring. The full scan range for our standard scanning head is 60 µm, so we effectively zoomed in by a factor of just over four by decreasing the maximum voltage to our piezobenders. The applied field range varied from 0.4 G due to the field of the Earth to 15.3 G.

We aimed to disentangle the magnetic signatures of the Meissner response, the fluxoids, and the vortices. First, the applied field was subtracted from each image. After this subtraction, the gray areas well outside the ring in each image represent the applied field. Thus, the magnetic signal in the images is due solely to the circulating currents in the ring and any vortices present. Shades that are light represent fields that are higher than the applied field, and those that are dark represent fields lower than the applied field. An additional step that proved useful in comparing magnetic signatures across the field range was to standardize the images by setting a fixed field range for all images: 0.14 G above the applied field and 0.09 G below the applied field giving a total range of 0.23 G.

As we increase the applied field, we expect to see three signatures of superconductivity: the Meissner effect, fluxoids being hosted in the center of the ring, and vortices nucleating in the bulk of the ring. These effects are highlighted separately in Fig. 3.7. The darkening of the feature in a) shows the Meissner response increasing linearly with the applied field from 0.6 G to 1.2 G. The introduction of a white spot in the center of the ring in b) is associated with the introduction of a fluxoid ($N = 0 \rightarrow N = 1$). The additional light region in the bulk of the ring in c) is the nucleation of a new vortex ($m = 3 \rightarrow m = 4$).

The overall evolution of our magnetic images in field, taken in 100 mG steps, is depicted in Fig. 3.8, with the applied field in gauss listed in the top left corner of each image. This array

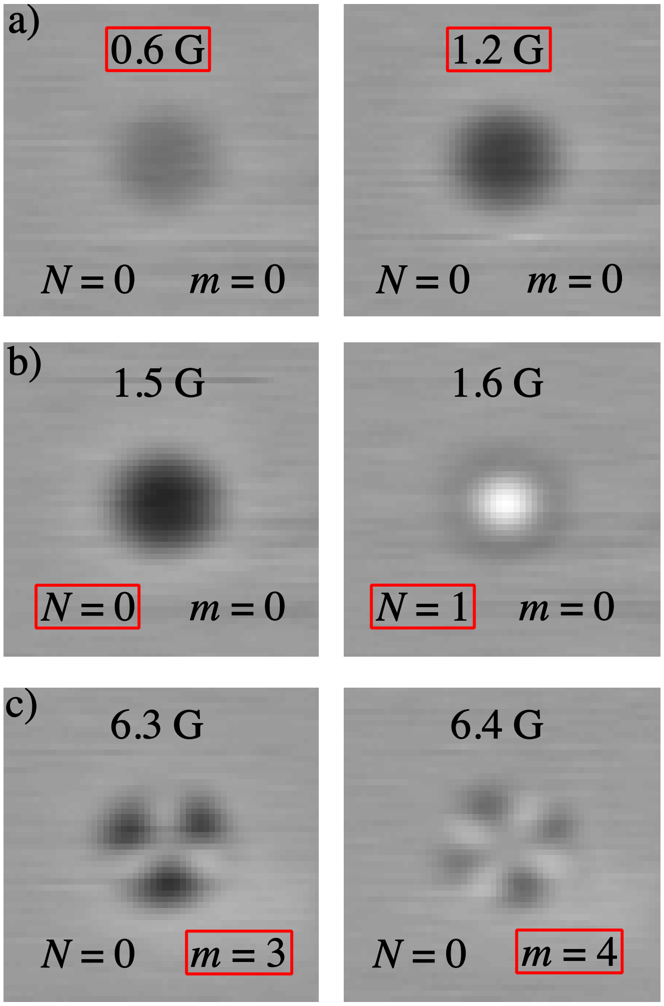

Figure 3.7: Hallmarks of superconductivity in our aluminum ring system. a) demonstrates the Meissner effect. b) shows a jump in winding number associated with a new fluxoid hosted in center of ring. c) depicts the nucleation of an additional vortex in the bulk of the ring.

clearly displays each of the three expected hallmarks of superconductivity. First, we observe a linearly increasing Meissner response starting from our lowest field of 0.4 G up to 1.5 G. The behavior changes abruptly at 1.6 G where the first fluxoid enters the center of the ring ($N = 1$). The magnetic field associated with the fluxoid is much larger in magnitude than the applied field. Recall that London's fluxoid has two terms—one dealing with the flux and the other with an induced supercurrent. Here, the stark field associated with the introduction of a fluxoid indicates that the induced supercurrent is "adding to" the flux to reach the first fluxoid quanta. At 4.2 G, a second fluxoid enters the center of the ring ($N = 2$). As we increase from 5.1 G to 5.2 G, two vortices nucleate in the bulk of the ring, marking the transition into the mixed state.

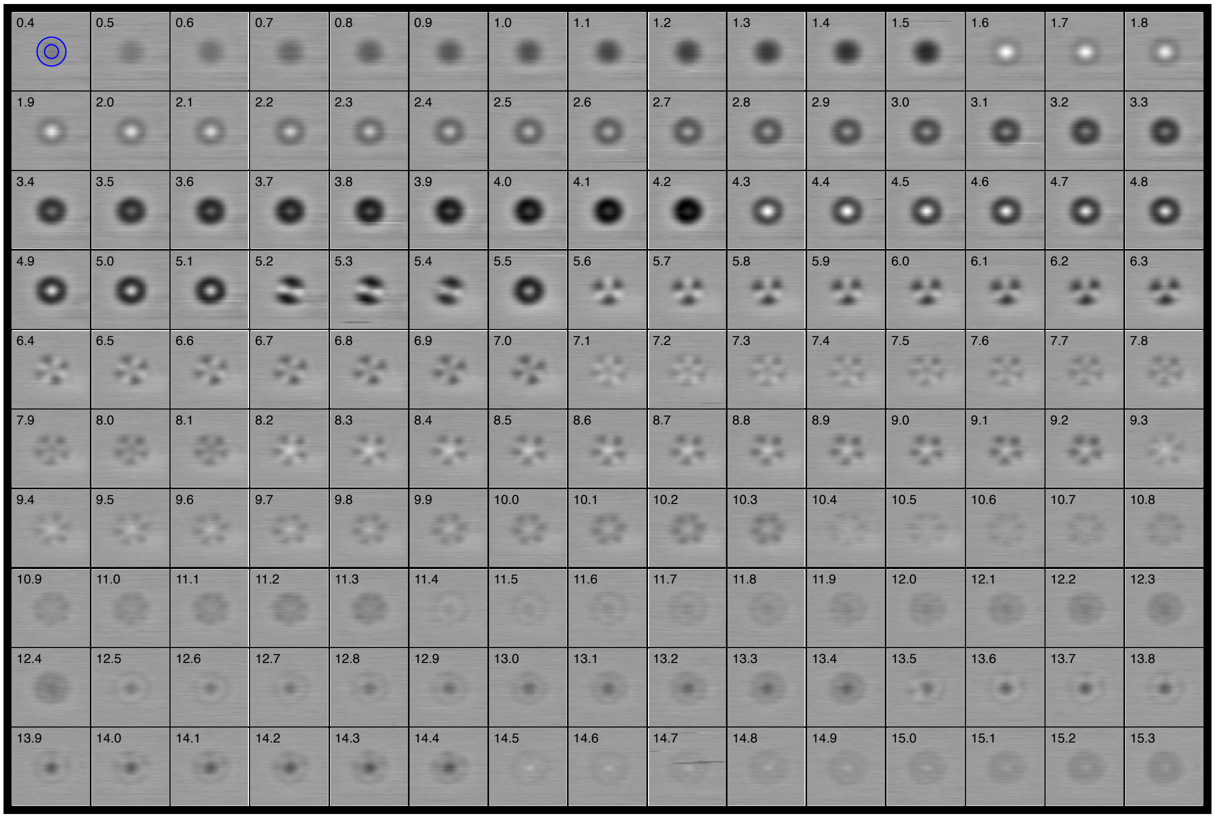

Figure 3.8: Magnetic images of the ring at various applied fields. Applied field (G) given in top left corner of each image. Meissner response is shown as darkening in the bulk of the ring. Increase in winding number is shown as white spot in the center of the ring. Nucelated vortices are white features in bulk of ring (see Fig. 3.7 for details). Outline of ring is shown in blue in the first image (top left).

There is particularly interesting behavior in the applied field range of 5.1 – 5.5 G. At 5.1 G, the ring hosts two fluxoids in its center and no vortices. As the field increases to 5.2 G, two vortices nucleate in the bulk of the ring. These vortices persist through three points in field (5.2 – 5.4 G). Then, at 5.5 G both vortices disappear only to have three nucleate at 5.6 G. This is a surprising deviation from the intuitive monotonic increase in N, m with applied field. However, a closer look at Fig. 3.5 shows that for any applied field h, there are many near-degeneracies in free energy. Additionally, Fig. 3.6 shows that N and m can drop with h, depending on ξ—highlighting the complex interplay between N and m. From this perspective, the abandonment of monotonic behavior is not surprising. Recall that our ξ value was limited by the resolution of our field steps. Possibly indicating that a careful measurement of H_1 would lead to an accurate prediction of this evolution.

As discussed earlier, the magnetic images provide strong evidence of the extremely low vortex pinning characteristic of granular aluminum. A clear example is shown in Fig. 3.8 for the field range of 5.2 – 5.4 G, where the vortices are situated 180° apart. This arrangement appears despite the fact that the vortex-vortex interaction are extremely small at such low vortex densities, suggesting that even the weak intervortex repulsion is much larger than any pinning effects in our rings.

3.5.2 The Magnetic Field at the Ring Center

In addition to the magnetic images, we measured the magnetic field B_z perpendicular to the ring at its center, very near its surface. This measurement was made by scanning across a *fixed* horizontal line passing through the center of the ring, and then averaging the voltage measurements of a few pixels at the center. The scan line with respect to the ring is schematically represented in Fig. 3.9, with the scan line in red. Multiple scans were averaged in an effort to reduce noise. The evolution of this measurement in field was predicted in our numerical project. We scanned 0.5 µm above the ring, used 10 mG steps, and field-cooled for each measurement. Again, the applied field was subtracted off to highlight the contributions from the circulating currents and vortices in the ring. The resulting data is shown in Fig. 3.10.

The B_z data of Fig. 3.10 can be difficult to interpret; however, it agrees with and contains the same information as our magnetic images. Starting from zero, a linear decrease in B_z is observed with increasing applied field. This is the Meissner response of the system. The first deviation from this linear response is an abrupt jump in B_z at 1.53 Oe, which marks the start of a sawtooth pattern. This jump is associated with the first fluxoid entering the center of the ring. As the applied field was further increased, there was another segment of Meissner response, followed by a second fluxoid entering the center of the ring at 4.13 Oe. Each fluxoid value is emphasized with alternating

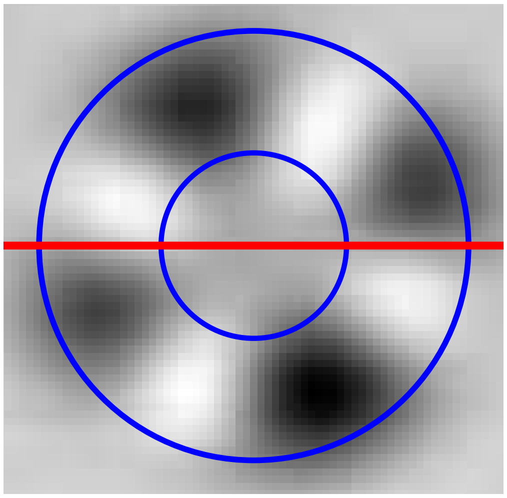

Figure 3.9: Schematic representation of B_z scan line. Ring outline is in blue and the horizontal scan line is in red. A few pixels near the center of the scan were averaged for B_z measurement.

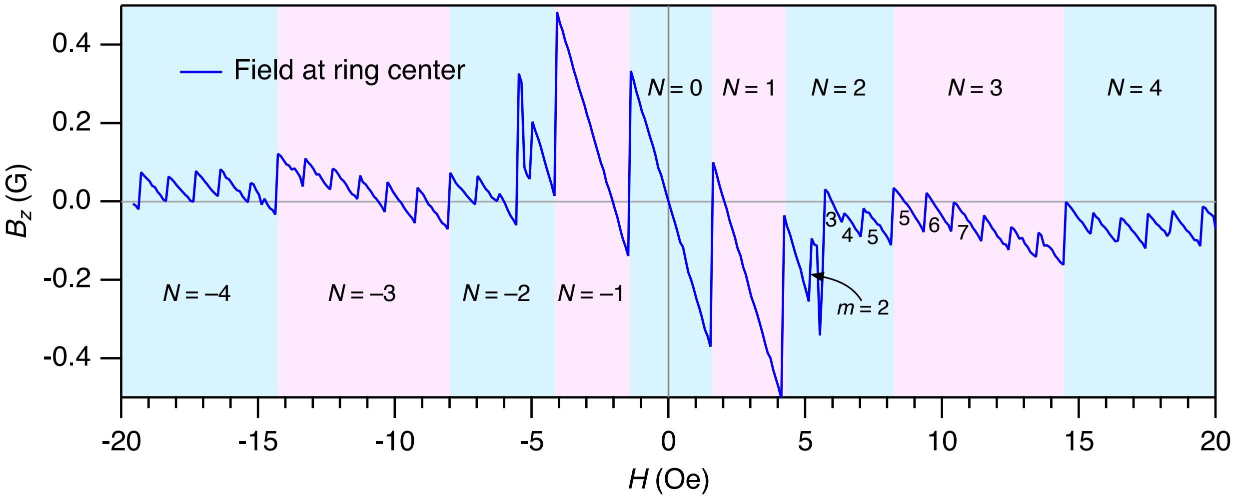

Figure 3.10: Experimental B_z data. Interfaces between blue and pink segments indicate a new fluxoid hosted in the center of the ring. Large jumps in B_z correspond to fluoid changes while small jumps coresopnd to vortex nucleation. Vortex nucleation is labeled along the smaller jumps in black text, starting with $m = 2$ and proceeding until our ability to count vortices was limited by the spatial resolution of the Hall-probe.

pink and blue regions in the background. Next, there is a much smaller jump associated with two vortices nucleating in the bulk of the ring at 5.13 Oe. The number of vortices m is indicated in black text near the smaller B_z jumps. These values of m were obtained by inspecting the magnetic images of Fig. 3.8 at the same applied field; the number of vortices in those images was directly counted, eliminating ambiguity in our results. This process was repeated until our ability to count vortices in the images was limited by the spatial resolution of the Hall probe at approximately 11 G. Just as in our magnetic images, the ring evolved from a two- to zero- to three-vortex state. A striking feature of Fig. 3.10 is the difference in magnitude between jumps due to fluxoids and those due to vortices—if the fluxoid is quantized, why should the magnetic signature due to vortices have a lesser effect on B_z than that due to fluxoids in the center of the ring? Recall that we are averaging pixels directly over the center of the ring, so our measurement is more sensitive to fluxoids than the relatively distant vortices nucleating in the bulk of the ring.

3.6 Comparison of Theory to Experiment

Before any vortices are nucleated, we can calculate the change in field associated with a change in the winding number N, by setting the magnetic Gibbs free energy associated with N fluxoids equal to that associated with $N+1$. From Eq. 3.15, it can be seen that this occurs when $h = N+1/2$. Thus the change in magnetic field between steps in N is simply $\Delta h = 1$, so that

$$\Delta H = H_0 \Delta h = H_0 = \frac{2\Phi_0 \ln(b/a)}{\pi\left(b^2 - a^2\right)}. \tag{3.22}$$

Inserting our values for a and b gives $\Delta H = 2.01\,\mathrm{G}$, while the experimental value shown in Fig. 3.10 is $\Delta H = 2.73\,\mathrm{G}$. This is a significant difference, as previous efforts have yielded better agreement [67]. However, the validity of this calculation is bolstered by the jumps in winding number at half-integer values of h shown in Figs. 3.6, 3.11a.

Recall that Fig. 3.6 shows the results of our free energy minimization, with v (upper panel) and N and m (lower panel) plotted as functions of the dimensionless field $h = H/H_0 = H/(2.73\,\mathrm{G})$. At low fields, we see the expected progression of N, starting at zero and increasing by one at half-integer values of h. As was mentioned in Sec. 3.4, the first vortex enters at $h \approx 2.2$ and the number of vortices rapidly rises to 4 before the vortex-vortex interaction becomes significant. After the $m = 4$ state, the introduction of more vortices is associated with a larger increase in h.

Figure 3.6 also depicts a decrease in N coinciding with the *increase* from $m = 1 \rightarrow 2$. Carefully examining Fig. 3.8 shows no such drop in N. This disparity may be explained by the previous discussion on the accuracy of the Ginzburg Landau coherence length ξ.

Once vortices enter the ring they find a common equilibrium radial position v, shown in the upper panel of Fig. 3.6. The nucleation of a new vortex ($\Delta m = 1$) is accompanied by a sharp increase in the vortices' radial position Then, as h increases at fixed m, the vortices slowly move toward the ring center, until another vortex nucleates and v jumps again. The inward movement of the vortices with h at constant m is due to a changing landscape of the potential well that confines vortices to the bulk of the ring. This energy competition will be detailed in Sec. 3.6.1.

At higher fields, N begins to increase again, but at a much slower rate than $\Delta N/\Delta h = 1$ as is observed before any vortices have nucleated. As the magnetic field is increased, the general trend of any superconductor is towards a state in which the field inside the superconuductor approaches the applied field, as such a state tends to minimize the Gibbs free energy. At low fields this trend is largely satisfied by the nucleation of successive fluxoids (increasing N), but evidently at higher fields the energetics are better satisfied by allowing more vortices to nucleate.

3.6.1 Comparison of the Theoretical and Experimental Field at the Ring Center

Equation 3.20 can be used to calculate the magnetic field at the ring center b_z for the values of N, m, and v (Fig. 3.6) that minimized the free energy. This field is shown in Fig. 3.11a for positive fields h. Comparison of the theoretical result with the experimental results B_z vs. H, replotted in Fig. 3.11b for easy comparison with the theoretical results, shows that the general structure of the two is very similar, although they differ in detail. We outline these similarities and differences in the following, recalling that h (H) and b_z (B_z) refer to the theoretical (experimental) applied field and ring-center field, respectively.

Formation of inital fluxoids. As h is increased from zero, we see the expected negative slope in b_z associated with the Meissner effect. At $h = 1/2$, the winding number N increases from 0 to

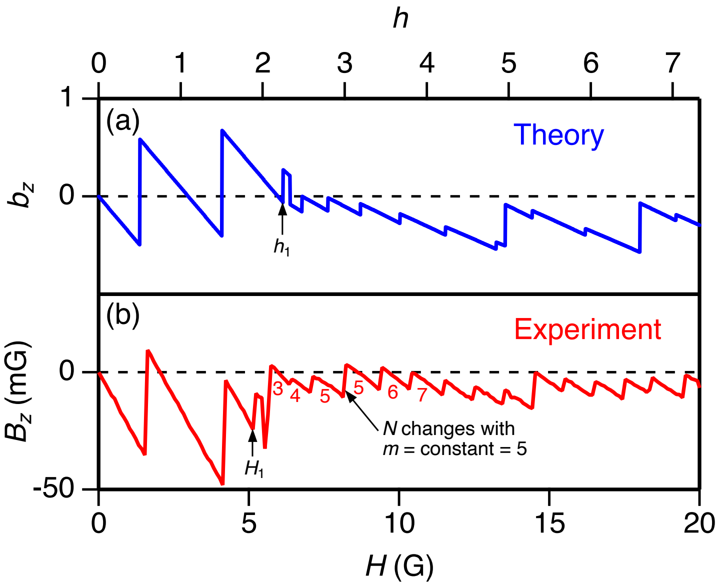

Figure 3.11: Experimental (red, a) and numerical (blue, b) plots of B_z as a function of applied field.

1 as indicated by a large positive jump in b_z; at $h = 3/2$, N increases from 1 to 2. It is notable, as can also be seen directly from Eq. 3.21, that the magnetic field at the ring center does *not* go to zero at integer values of N. The same general behavior is seen in the experimental data: a negative-slope Meissner behavior punctuated by jumps as N increases. Recall that we have scaled h (that is, chosen H_0) so that these fluxoid jumps occur at the same points on their respective axes.

First vortex entry. At $h \equiv h_1 = 2.25$, there is a small positive jump in b_z associated with the nucleation of the first vortex; according to Eq. 3.21 the ratio of this jump to that due to an increase in N is $0.351/1.083 = 0.324$. At a slightly higher field b_z drops down again; from Fig. 3.6, we can see that this drop is due to a change in N, from 2 to 1.

Experimentally, a similar jump is seen at $H_1 = 5.2\,\mathrm{G}$, also soon followed by a large drop. However, as can be seen from Fig. 3.8, this drop is due to vortices temporarily *leaving* the ring, with $m = 2 \rightarrow 0$. We find that the ratio of the first vortex jump to a fluxoid jump is about 0.34, very close to the theoretical value.

Nucleation of successive vortices. As h is increased beyond h_1 a series of jumps in b_z is observed; each smaller jump is associated with the nucleation of another vortex. The heights Δb_z

of these jumps are not consistent, generally becoming smaller for higher-m jumps. In particular, the higher-m jumps are significantly smaller than the jump at h_1 when the first vortex enters.

This behavior occurs because the field at the ring center depends not only on the number of vortices but also on their radial position v; vortices that are closer to the center obviously will contribute more strongly to the field there. This can be seen directly from Eq. 3.20, where the vortex contribution to the field is $b_z^m = m(b/v - 1)$. The dependence of v on h is given in Eq. 3.4. We note that every increase in m is accompanied by a jump in v as well. This makes sense: When a vortex is added, the free energy can be lowered by increasing the inter-vortex spacing (lowering ε_{vv}), at the cost of moving the vortices outward (up the confining potential well). Thus in the term $b_z^m = m(b/v - 1)$, when the increase in m is somewhat offset by an increase in v, so the overall jump in b_z is diminished.

We also note that, as already noted, the first few vortices nucleate over a relatively small field range, but for higher m the field range Δh required to nucleate the next vortex increases with m.

Experimentally the situation is somewhat different. First, the field jump ΔB_z as successive vortices are added is significantly larger relative to the jump due to a change in N than in the theoretical model. And, roughly, the field range ΔH needed to nucleate the next vortex appears relatively constant.

Slope above h_1 *or* H_1. As is evident from Eq. 3.21, the theoretical b_z curve consists of an overall negative-slope Meissner term punctuated by occasional jumps as N and m change. The Meissner contribution is simply proportional to h, and so this slope is the same for all h. However, in Fig. 3.11a we note that the slope *between* successive jumps, while still negative, is significantly less than the pure Meissner slope observed below h_1. Again, we can ascribe this behavior to the radial movement of the vortices. As Fig. 3.6 shows, between m- or N-mediated jumps, v decreases in a linear fashion. Since a derease in v results in an increase in b_z, this effect tends to reduce the overall slope from its large, negative pure-Meissner value.

The same behavior is observed in the experiment, where the slope between N- or m-changing events is significantly lower than its pure-Meissner value. Again, this is indirect evidence that small radial changes in the vortices' position play an important role in determining the details of the resulting measured fields.

3.7 Discussion

The agreement between our theoretical project and experimental results validates our approach of studying fluxoid behavior in thin-film ring systems. Furthermore, we demonstrated the effectiveness with which our method removes uncertainty with regard to vortex formation. While interesting in its own right, this experiment also serves as a method to measure and theoretically predict fluxoid behavior in a spin-triplet superconducting material in an effort to observe half-fluxoid quantized vortices. Our efforts to extend this experiment to the spin-triplet superconductor UTe_2 will be explored in Chapter 4.

Chapter 4

The Search for Half-Quantized Fluxoids

> "Mysteries abound where most we seek for answers."
>
> —Ray Bradbury

4.1 Introduction

Type II superconductors capable of hosting half-quantized superconducting vortices (HQVs)—superconducting vortices carrying a fluxoid of $\Phi_0/2$ or $hc/4e$—have generated interest as a topological quantum computing architecture. It has been proposed that the normal core of a HQV can support a *Majorana fermion* [87]. Instead of traditional bosonic, fermionic, or exotic anyonic exchange statistics, these excitations are theorized to obey non-Abelian exchange statistics, making them viable for quantum computing operations [31, 88–93]. Rather than picking up a simple phase factor upon exchange of two particles, the final quantum state of these HQVs is fundamentally altered by the precise sequence in which they are exchanged [94, 95]. It is important to distinguish between HQVs and half-quantized fluxoids associated with geometric holes in superconducting structures. Half-quantized fluxoids have been observed in physical holes [96], and while scientifically interesting, their utility is limited because they are fixed in space. HQVs hold much more promise for devices, as their magnetic structure allows them to be moved in space via an applied field [97].

Although spin-triplet superconductors may be capable of hosting HQVs, HQVs are believed to be energetically unfavorable compared to their fully-quantized counterparts [4,30,32,96,98,99]. As detailed in Chap. 1, there are charge currents associated with either fluxoid quantization condition for vortices; however, spin currents are only present in HQVs. Charge currents are screened and fall off exponentially, whereas spin currents remain unscreened and fall off as approximately $1/r$.

This leads to an energy profile that diverges logarithmically with sample size [30]. Thus, HQVs are generally unstable in the bulk [30,32]. In contrast, in a mesoscopic geometry such as a micrometer-scale ring, unscreened spin currents are naturally restricted, making them a better platform for HQVs. Another method of stabilizing HQVs is by introducing an in-plane magnetic field [4,30,32,96,99]. Unlike spin-singlet Cooper pairs, spin-triplet Cooper pairs can be magnetically polarized, allowing their spins to align with the field. This lowers the Zeeman energy, and thus the overall energy of the system.

4.1.1 Candidate Material Uranium Ditelluride

Our main material for study is uranium ditelluride (UTe_2), which was recently found to superconduct [100]. As shown in Fig. 4.1, it is a nearly ferromagnetic superconductor and exhibits strong ferromagnetic spin fluctuations which may be responsible for its unconventional pairing. Although paramagnetic in its normal state, its physical properties are strikingly similar to those of ferromagnetic materials [3,100,101]. Its candidacy as a potential spin-triplet superconductor is bolstered by Knight shift measurements (with applied magnetic fields along various orientations with respect to the d-vector) [3,102], an experimentally verified high second critical field [100,103], and power law behavior of the electronic specific heat below its transition temperature [104–107] as seen in Fig. 4.2. UTe_2 is a particularly convenient material for study as its claimed critical temperature of 1.6 K [100] (demonstrated with various measurements in Fig. 4.2) is close to the base temperature of our system and can be exceeded for field-cooling with modest sample heating.

Knight shift measurements yield information about the spin susceptibility of materials—the degree to which their conduction electrons can be polarized by an external magnetic field [108]. The Knight shift is a shift in nuclear magnetic resonance (NMR) frequency between identical nuclei in a metallic and non-metallic environment. This quantity can identify changes in spin pairing symmetry associated with transitioning into the superconducting state. Above their critical temperature, both spin-singlet and spin-triplet superconductors are normal metals (generally speaking) and exhibit finite magnetic susceptibility, and thus a Knight shift. Below T_c, the Cooper pairs in spin-singlet

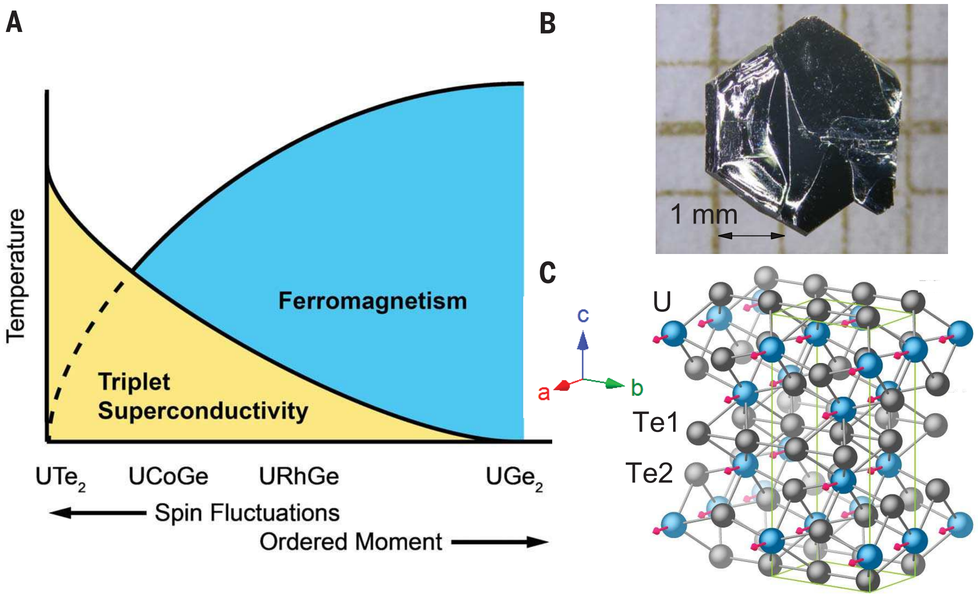

Figure 4.1: (A) Phase diagram of Uranium-based superconductors, UTe_2 is on the paramagnetic end with strong spin fluctuations that may be responsible for spin-triplet pairing. (B) Millimeter-scale bulk UTe_2 crystal. (C) Crystal structure of UTe2, with U atoms in blue and Te atoms in gray. From Ran, S., Eckberg, C., Ding, Q.-P., Furukawa, Y., Metz, T., Saha, S. R., Liu, I.-L., Zic, M., Kim, H., Paglione, J., & Butch, N. P. (2019). *Nearly ferromagnetic spin-triplet superconductivity*. *Science*, **365**(6454), 684–687. Reprinted with permission from AAAS.

superconductors have zero net spin, causing them to lose their spin susceptibility. This manifests itself as a significant decrease in Knight shift compared to that above T_c. For spin-triplet materials, the pairing symmetry allows the electrons to continue to be polarized below T_c when the d-vector is perpendicular to the external field, leading to little or no change in Knight shift [3]. Knight shift measurements indicate that UTe_2 is a spin-triplet superconductor [3, 100, 102, 109, 110]. This measurement technique, along with specific heat measurements [5, 6], has been used to disqualify other notable candidates, such as strontium ruthenate Sr_2RuO_4, a previously compelling avenue for topological quantum computing [4, 111–113]. Jang *et al.* utilized cantilever magnetometry to measure magnetization jumps associated with fluxoids hosted in a micrometer-scale ring with increasing applied field along the axis of the ring [4]. With the introduction of a sufficiently large static in-plane field, the magnetization jumps associated with increasing perpendicular field decreased by a factor of two compared to their values in the absence of an in-plane field. This is consistent with the formation of half-quantized fluxoids. See Figs. 4.3, 4.4 for a visualization of the

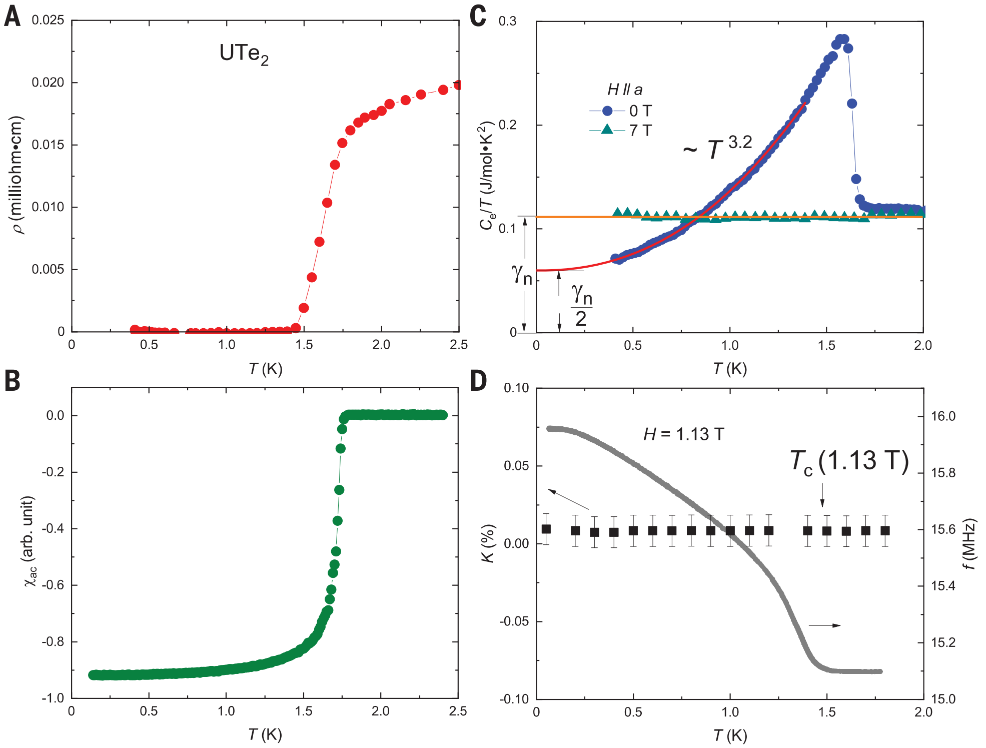

Figure 4.2: Temperature-dependent properties of UTe_2. (A) Resistivity as a function of temperature, showing a critical temperature of approximately 1.6 K. (B) AC magnetization data indicating a superconducting transition. (C) Electronic contribution to heat capacity exhibiting power law behavior below the critical temperature. (D) NMR Knight shift data indicating a superconducting transition. All of these measurements indicate a similar critical temperature. Note that in (D) H is applied parallel to the d-vector, so this data does not indicate spin triplet superconductivity. See Fujibayashi *et al.* [3], for example, for Knight shift comparison along different crystal axes. From Ran, S., Eckberg, C., Ding, Q.-P., Furukawa, Y., Metz, T., Saha, S. R., Liu, I.-L., Zic, M., Kim, H., Paglione, J., & Butch, N. P. (2019). *Nearly ferromagnetic spin-triplet superconductivity*. *Science*, **365**(6454), 684–687. Reprinted with permission from AAAS.

ring structure on a cantilever, as well as magnetization data as a function of applied field (along the rings axis) for various in-plane fields [4]. This magnetization data has been difficult to reconcile with the Knight shift and specific heat measurements indicating spin-singlet superconductivity. A possible explanation for these results is that the in-plane applied field caused fully-quantized vortices to nucleate in the sidewalls of the ring (or at a canted angle) [7], leading to a smaller change in magnetization, as measured by the cantilever.

A related piece of evidence supporting the status of UTe_2 as a spin-triplet superconductor is its high critical field with respect to the *Pauli limit* [100, 101, 114]. In spin-singlet pairing symmetry, electron spins are antiparallel, leading to misalignment of at least one electron spin with the applied

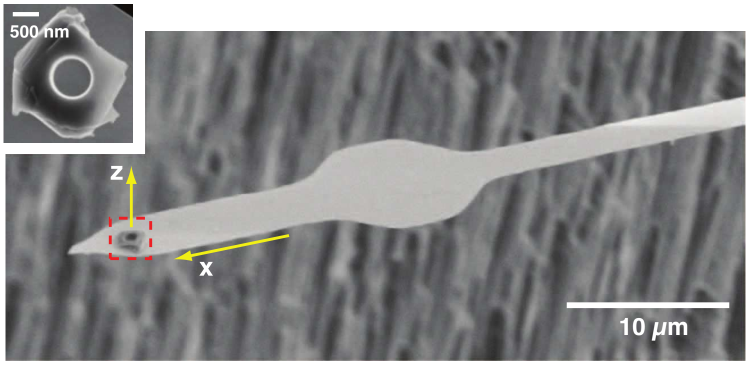

Figure 4.3: The cantilever used to make magnetization measurements and a typical Sr_2RuO_4 ring. From Jang, J., Ferguson, D. G., Vakaryuk, V., Budakian, R., Chung, S. B., Goldbart, P. M., & Maeno, Y. (2011). *Observation of Half-Height Magnetization Steps in Sr_2RuO_4*. *Science*, **331**(6014), 186–188. Reprinted with permission from AAAS.

field. The Zeeman energy associated with this misalignment ($U = -\vec{\mu} \cdot \vec{B}$) becomes energetically unfavorable when it exceeds the condensation energy [115], and the associated magnetic field is the Pauli limit. Since spin-triplet pairing symmetry permits the spin of both electrons to align with an applied field, they can superconduct at fields well above the Pauli limit. Upper critical field measurements for uranium ditelluride are consistent with spin-triplet superconductivity [100, 103].

4.2 Devices and Experiments

We have conducted a series of experiments aimed at confirming superconductivity, measuring the critical temperature, and imaging superconducting vortices in uranium ditelluride. Collaborators from Nick Butch's group at the National Institute of Standards and Technology (NIST) grew high-quality single crystal UTe_2. Its crystal structure and a photograph of a bulk crystal grown by our collaborators are shown in Fig. 4.1. Collaborators from the Daniel Dessau group at the University of Colorado Boulder used a focused ion beam to fabricate devices of UTe_2 suitable for scanning Hall-probe microscopy and Little-Parks experiments. Scanning Hall-probe microscopy requires samples that are flat on the micrometer scale to prevent our Hall probes from crashing into the surface. As detailed in Chap. 2, probe fabrication and mounting processes represent a large time

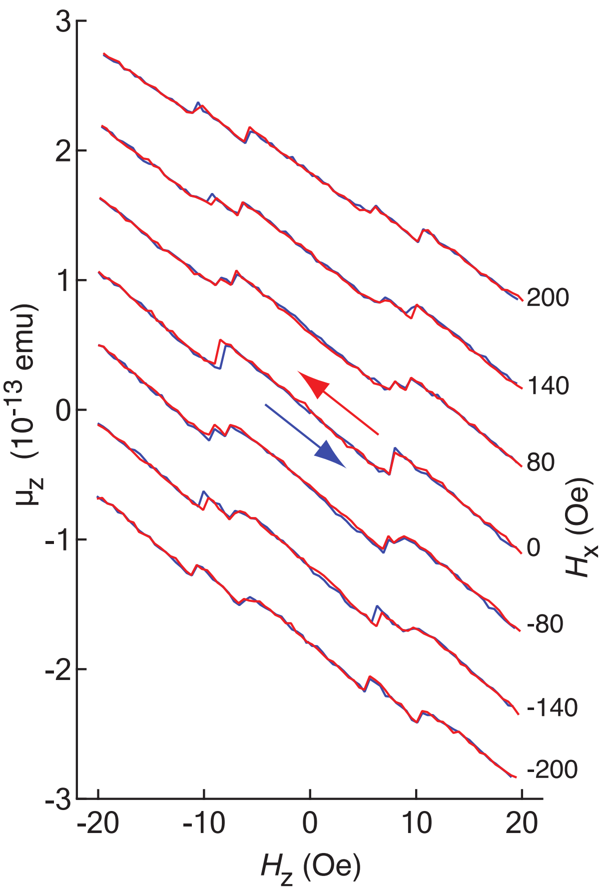

Figure 4.4: The claimed magnitization data that reveals fully-quantized and half-quantized fluxoids, depending on the in-plane applied field [4]. Magnetization (left axis) is displayed as a function of applied field along the ring's axis. The series of trends correspond to varying fixed in-plane applied fields (right axis). For an applied in plane field (H_x) of zero Oe, there are clear jumps in magnetization associated with increasing H_z (in magnitude). As the in-plane field is varied, what was once a single jump in magnetization corresponds to two smaller jumps. This is the claimed evidence for half-quantized fluxoids. These results have been contested [5,6], potentially explained by vortices nucleating in the sidewalls of the ring [7]. From Jang, J., Ferguson, D. G., Vakaryuk, V., Budakian, R., Chung, S. B., Goldbart, P. M., & Maeno, Y. (2011). *Observation of Half-Height Magnetization Steps in* Sr_2RuO_4. *Science*, **331**(6014), 186–188. Reprinted with permission from AAAS.

investment, so great care is taken not to inadvertently destroy a probe. This presents difficulties in device fabrication.

4.2.1 Planarized slab measurements

Confirming Superconductivity and Measuring the Critical Temperature

The aim of our first imaging experiment was to confirm that devices fabricated from UTe_2 crystals were superconducting by measuring their critical temperature and nucleating a fully-quantized vortex. To this end, CU Boulder collaborators fabricated a flat, planarized slab approximately 20 micrometers long, 10 micrometers wide and 3 micrometers thick, as shown in Fig. 4.5. The device fabrication process is detailed in Sec. 5.3.1. It is clear from Fig. 4.5 that the slab has a sufficiently flat surface for scanning Hall-probe microscopy.

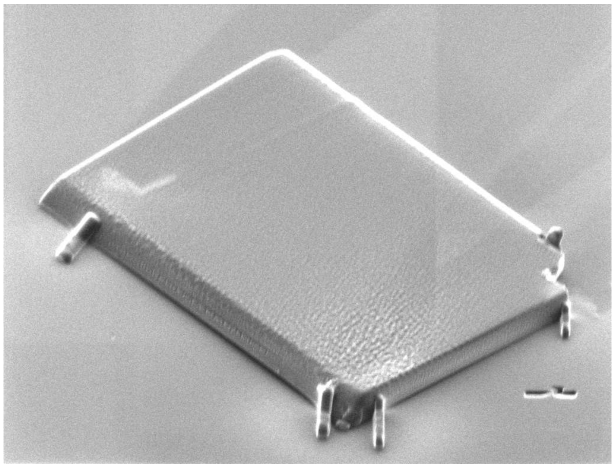

Figure 4.5: An electron beam photo of an approximately 20 µm × 10 µm planarized UTe_2 slab.

Our first objective was to confirm the superconductivity in and measure the critical temperature of the slab. We located the slab with our Hall probe microscope and carefully centered our scan range around the center of the slab using our positioning and scanning systems. We then fixed the scanning piezobender position in one direction, allowing us to continuously scan a one-dimensional line about the center of the slab. After taking preliminary data to estimate the critical temperature of the slab, we applied a static magnetic field and documented our horizontal scans as a function of temperature from 1.65 K to 1.40 K. The resulting data appears in Fig. 4.6, with a 1.65 K scan at the top of the image and a linear progression to 1.40 K at the bottom.

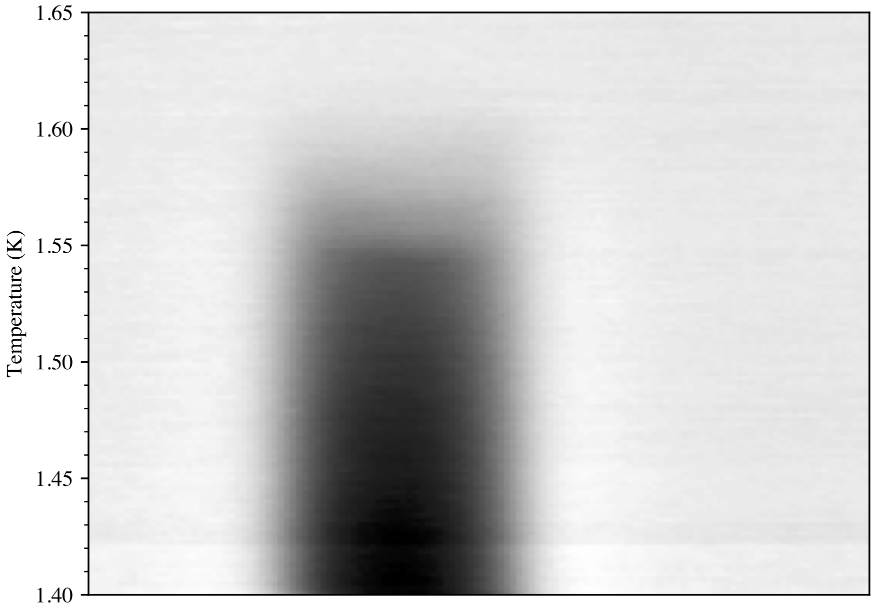

Figure 4.6: Scanning Hall data to measure the critical temperature of the UTe_2 slab. The probe's position was fixed in one direction of the scan plane and a one-dimensional scan was performed about the center of the slab. The progression of those scans as a function of temperature (from 1.65 K at top to 1.40 K at the bottom) is depicted. The dark region indicates a Meissner response, whose disappearance marks the critical temperature.

The Meissner response of the slab is seen as a dark feature that decreases in intensity with increasing temperature. This response was quantified by generating fits to the individual horizontal line profiles that form Fig. 4.6. An example fit is shown as the blue plot in the left graph of Fig. 4.7, the measured line profile is the red plot. Due to its appearance in the line profiles, we refer to the magnitude of the Meissner response as the *Depth of the Meissner Signal* (approximately 9 arbitrary units in the example above). This depth is plotted as a function of temperature in the right graph of Fig. 4.7. This data shows a critical temperature near 1.6 K which closely matches values measured by our crystal growers and those claimed in the literature [100].

Nucleating and Imaging a Vortex

The next experimental effort was to nucleate and image a fully-quantized superconducting vortex. We imaged the magnetic response of the superconducting slab in a series of applied magnetic fields, field-cooling between each scan. Two scanning Hall images that illustrate this work are shown in Fig. 4.8. The left image shows the slab in the Meissner state. The yellow-green

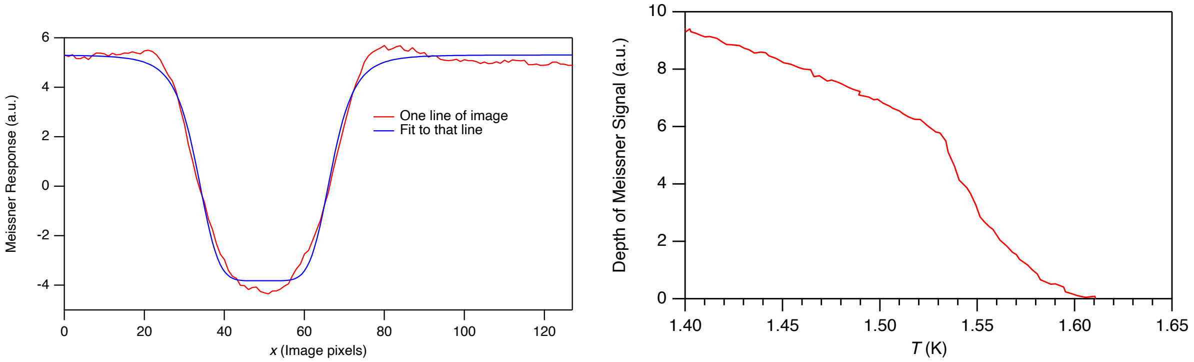

Figure 4.7: The Meissner response from Fig. 4.6 was cataloged as a function of temperature. Left plot shows a single horizontal line profile of a scan (in red) and a numerical fit of that scan (in blue). Right plot shows the magnitude of that Meissner response as a function of temperature. This indicates a critical temperature of 1.6 K.

region that makes up the background is the applied field (near 20 G). The light halo surrounding the slab is a region in which the measured field is higher than the applied field, as the expelled field lines pass around the slab and cluster near the edges (see Fig. 1.2) [116, 117]. The field directly over the slab is lower in magnitude than the applied field, due to the slab's Meissner response. The right image shows the slab imaged in a higher applied field in which a vortex is nucleated in the bulk of the material. Since the Meissner response scales linearly with the applied field [118, 119], data from Fig. 4.7 was appropriately scaled to the applied field of the right image of Fig. 4.8. The Meissner response and applied field were subtracted from the raw Hall voltage from the scan, leaving only the contribution from the vortex. This is analogous to the method used to isolate the magnetic contribution from the fluxoids alone in our aluminum ring experiment. This is believed to be a fully-quantized vortex as the geometry and lack of in-plane magnetic field presumably make HQVs unfavorable in this scenario [4, 30, 32, 96, 99].

4.2.2 Little-Parks Device

The groundbreaking Little–Parks experiment confirmed the electron pairing described by BCS Theory and the fluxoid quantization discussed in Sec. 1.6.2 [120]. In this experiment, Little and Parks measured the critical temperature of a thin-walled superconducting cylinder as a function of applied magnetic field along the axis of the cylinder. Rather than varying smoothly with the

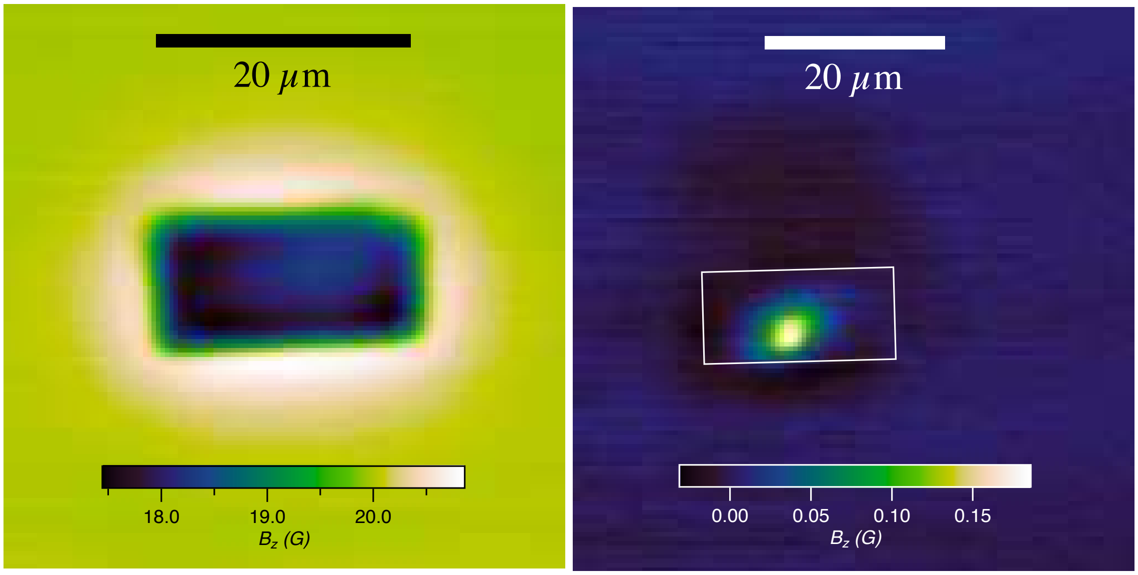

Figure 4.8: Scanning Hall-probe images of the UTe$_2$ slab from Fig. 4.5 in the presence of an applied field. Left image shows slab in a field lower than H_{c1}. Right image shows slab in the intermediate state with one nucleated vortex. The applied field and Meissner response have been removed numerically to highlight the contribution from the nucleated vortex.

applied field, the critical temperature exhibited oscillations with a period of $hc/2e$, indicating fluxoid quantization at that value. Local maxima in critical temperature coincide with minima in free energy for a superconductor [96, 120–122]. It is important to note that the critical temperature is not measured directly; instead the device was held at a fixed temperature along its superconducting transition (approximately 1.55 K in Fig. 4.6, for example) and resistance oscillations were measured as a function of magnetic field, as shown in Fig. 4.9. These resistance measurements serve as an indirect proxy for measuring the critical temperature [14, 120]. The goal of our experiment was to measure resistance oscillations associated with fluxoids hosted in a ring device as a function of the out-of-plane field at a variety of static applied fields in the plane. If the out-of-plane oscillation period reduced by a factor of two (to $hc/4e$) with a sufficiently high in-plane field, it would suggest half-quantized fluxoids hosted in the ring.

For our proposed experiment, collaborators from CU Boulder fabricated a device suitable for a Little-Parks experiment that can be seen in Fig. 4.10. Here, four leads are arranged for a transport measurement analogous to that of Fig. 3.2. In the center of the transport geometry, a micrometer-scale ring structure was fabricated in which the fluxoids would be hosted. During fabrication,

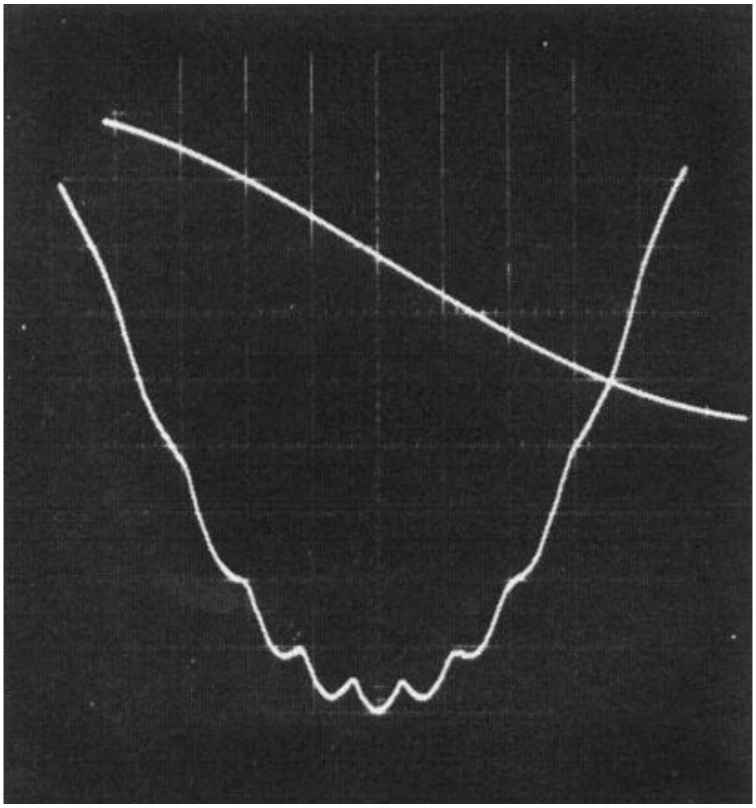

Figure 4.9: Original data from Little-Parks experiment. Displayed are oscillations in resistance along the superconducting transition and the applied magnetic field (linear feature). Reprinted Fig. 4.9 with permission from: W. A. Little and R. D. Parks, *Phys. Rev. Lett.* **9**, 9 (1962). Copyright (1962) by the American Physical Society.

one end of the slab is naturally tapered, and this edge was used as a ramp to promote conduction from the substrate to the top of the device. 10 nm of chrome and 100 nm of gold were thermally evaporated on top of the substrate to allow conducting channels. Deep focused ion beam (FIB to be discussed in Sec. 5.3.1) cuts were made through the conducting layer and into the silicon substrate below to electrically isolate the paths. Lastly, the FIB was defocused to weakly mill the top surface of the device, removing the conducting layer from the leads and the ring structure.

This device was plagued with conduction issues. First, the mesoscopic leads that connect the device to a current supply and voltmeter were damaged in transit and had to be repaired with silver paint. The device itself seemed to be electrically shorted, despite the cuts made through the ramp and device and into the substrate. A likely culprit was a chrome-gold layer opposite the platinum ramps that may have remained in tact, shorting the sample across the ring structure. These issues

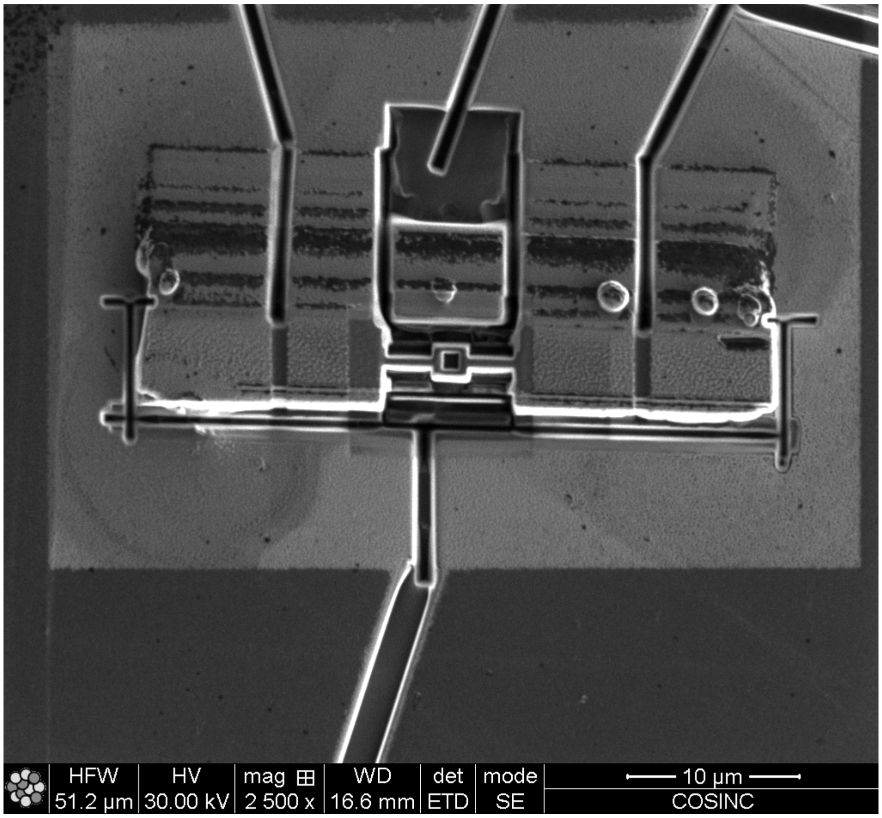

Figure 4.10: Electron beam image of Little-Parks device fabricated from uranium ditelluride. Current passes between outer leads, voltage difference is measured between inner leads, and fluxoids are hosted in the center ring structure.

led us to pursue an alternate sample geometry and experiment that would not rely on intricate conducting paths.

4.2.3 Attempt to Observe Trapped Flux and Vortices in a Ring

After preliminary experiments to confirm superconductivity, measure T_c, and nucleate a vortex in the slab, the next objective was to conduct a fluxoid experiment on a uranium ditelluride ring analogous to our aluminum ring experiment in Chapter 3. That is, we intended to image fluxoid evolution in the center of the ring and vortex nucleation in the bulk as a function of applied field along the axis of the ring in addition to making B_z measurements near its surface. This experiment was to be conducted at a variety of in-plane applied fields in an effort to stabilize half-quantized fluxoids and vortices. A finished device potentially suitable for this experiment was fabricated by our CU Boulder collaborators and can be seen in Fig. 4.11.

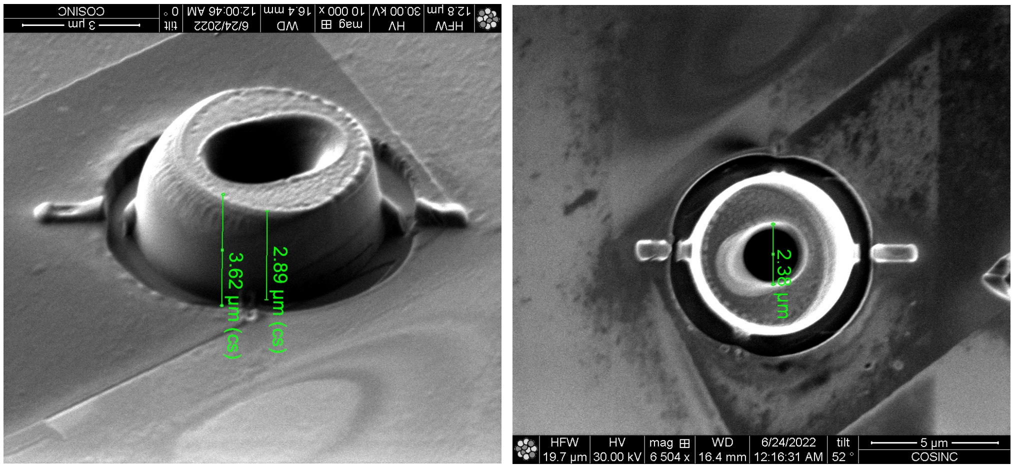

Figure 4.11: Electron beam photos of micrometer-scale UTe_2 ring fabricated for a fluxoid experiment. Left image shows a side view and right image shows a top-down view of the same ring.

The process of orienting our probe position at room temperature as well as calibrating its movement and positioning over a sample at cryogenic temperatures is important to introduce to explain the difficulties encountered in this experiment. At room temperature, we use a digital microscope and a reflective silicon mirror situated on the microscope assembly near the Hall probe (Fig. 4.12) to position our probe with respect to the sample (Fig. 4.13). Pictured in the bottom portion of both images in Fig. 4.14 is a granular aluminum structure composed of 4 µm-diameter dots arranged in a de Bruijn sequence whose dimensions are on the scale of hundreds of micrometers. This type of pattern composed from a de Bruijn sequence is useful in positioning at cryogenic temperatures. Any 4×4 subset of this pattern, interpreted as the presence and absence of superconducting dots, uniquely defines the position of the subset. Our pattern is large enough to orient the Hall probe above it at room temperature, thus when we cool down, lower the Hall probe, and take a preliminary field-cooled image, we can find our position. This also serves as an *in situ* movement calibration method. We record our position and move to some nearby position on the pattern. We can then calibrate the measured steps taken by the attocube to the distance traveled in each direction according to the de Bruijn pattern.

When attempting to image the rings, we first used the de Bruijn to locate our position and calibrate movement as described above. Referencing a photo of the device placement with respect

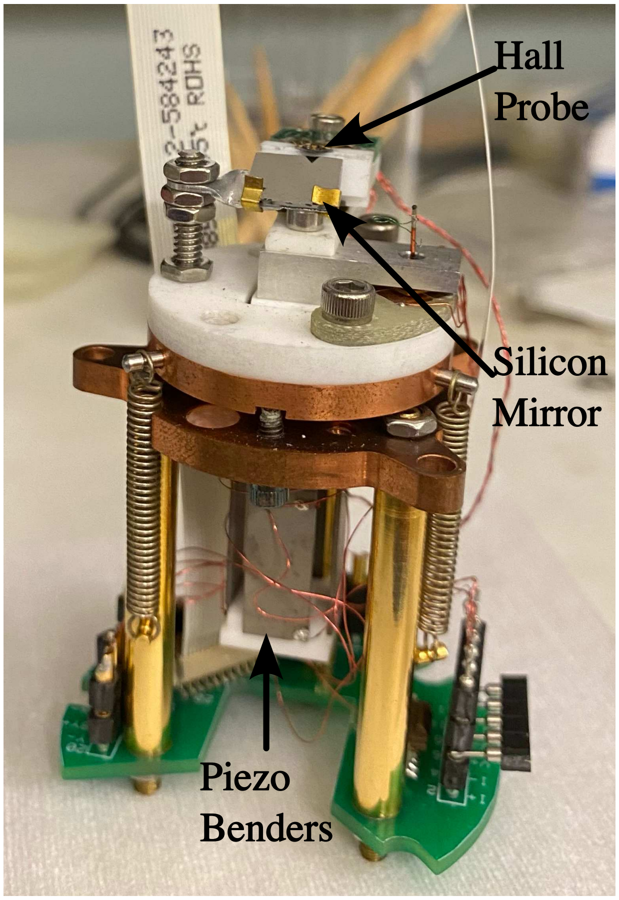

Figure 4.12: Scanning head of microscope showing position of silicon mirror with respect to Hall probe. Mirror used to orient Hall probe over sample for positioning at room temperature.

to the de Bruijn pattern, we calculated the necessary number of steps and direction to position our probe over the device. After moving over the estimated device position and field-cooling, no superconducing signature was present. In addition to the de Bruijn pattern, these substrates had a series of aluminum guide arrows as seen in Fig. 4.14. We attempted to position the probe over a nearby guide arrow, which was successfully centered in our field of view upon field-cooling, supporting our position calibration and movement scheme.

We returned to the estimated device position and took images in various applied fields, but no device signal was evident. To confirm device placement, we used the previously described compensator program to plot the z-piezo touch voltage (vertical touch position) in a 1 µm × 1 µm grid spanning the scan range. This revealed a device with dimensions consistent with those of Fig. 4.11 near the center of our scan range. We continued scanning the device in a variety of

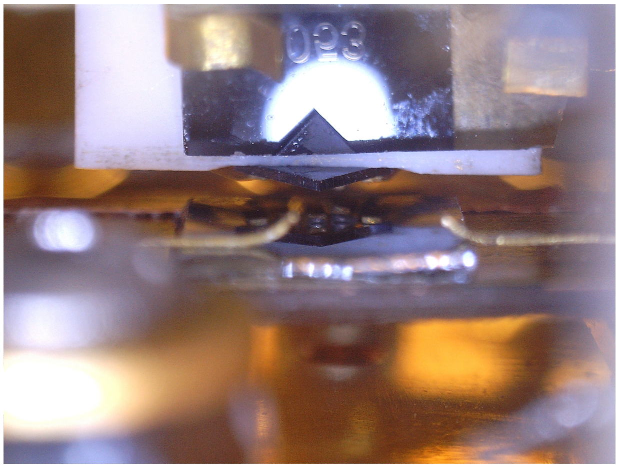

Figure 4.13: Digital microscope image of Hall probe position with respect to sample at room temperature. The silicon mirror is the reflective rectangle in the upper portion of the photo. The sample's reflection reveals a label "063". The Hall probe's reflection is the sharp pointed triangle on the bottom of the mirror. The gold fingers in the reflection are used to secure the sample to the sample holder. The sample, Hall probe, and sample-holding-gold fingers are all visible in the bottom portion of the photo. The top of a thermometer is out of focus in the foreground of the photo on the left side.

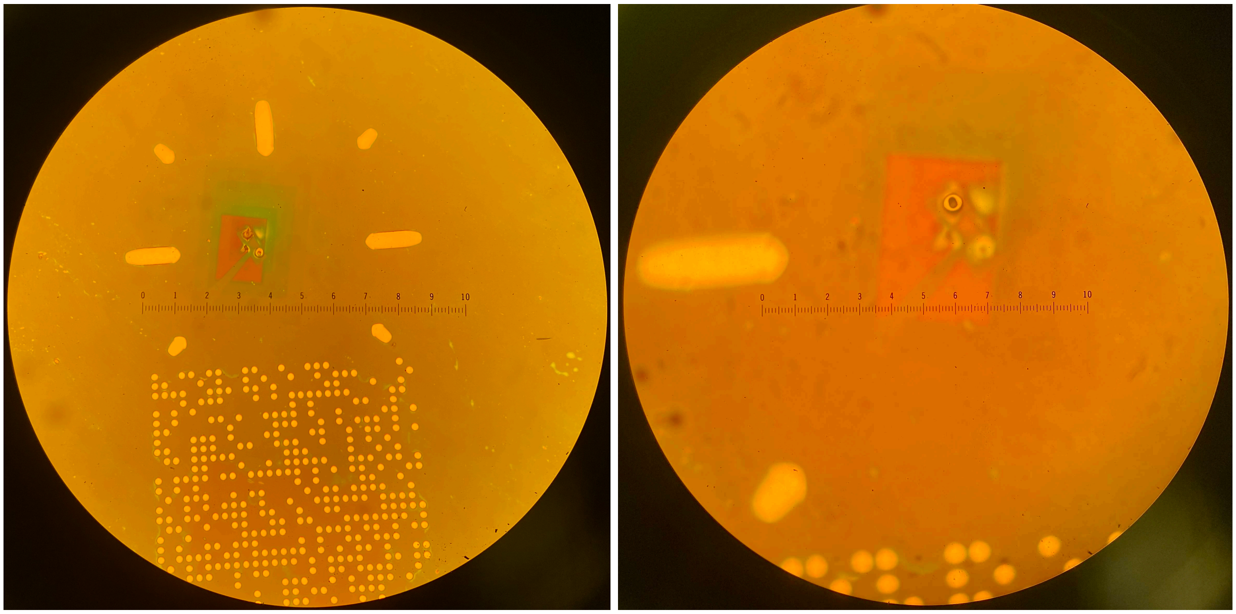

Figure 4.14: Optical images of UTe_2 ring from Fig. 4.11. Left image taken with 40 × objective, right image with 100 × objective. These images demonstrate the layout of the rings with respect to the guiding arrows and de Bruijn pattern (disks). We orient position and calibrate movement with respect to de Bruijn and then move over the device.

applied fields and detected a weak signal. It was unclear whether this indicated superconductivity or whether it was an artifact arising from an electrostatic feature. Despite an electrostatic feature being static in the lab frame, it leads to a time-varying potential from the perspective of the scanning Hall probe. This potential can capacitively couple to the sensor, producing a false signal.

Figure 4.16 shows scanning Hall data for the magnetic signal in an applied field of 3 G. The image on the left was taken at 2.20 K (above T_c) and the image in the middle was taken at 1.28 K (presumably below T_c); they are plotted on the same field scale. The signal did not change significantly in appearance above or below T_c. The raw data from the middle image was subtracted from that of the left image and plotted on the same field scale as the other two in the right image for comparison. There is a faint outline of the artifact in the right image; however, this could be explained by a subtle difference in scan height or position between images due to thermal cycling.

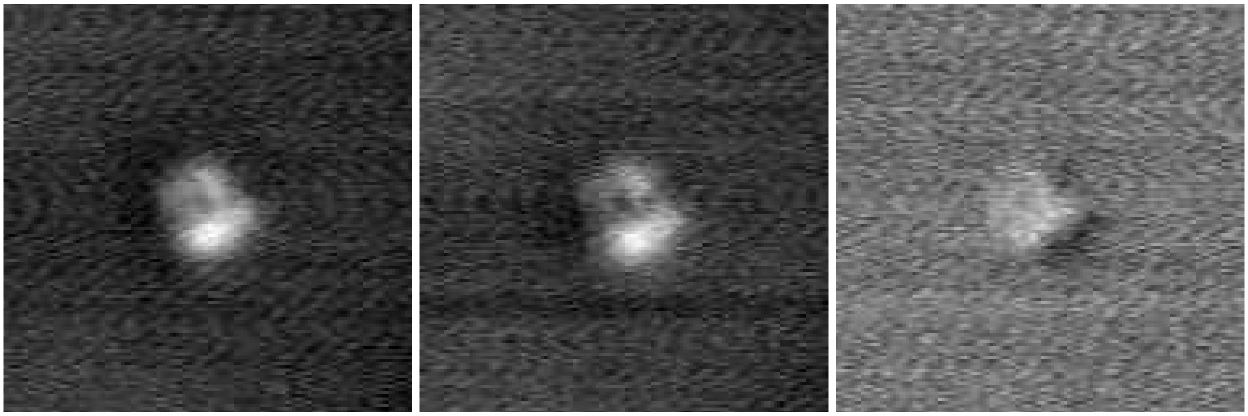

Figure 4.15: Left and middle images are scanning Hall-probe images of UTe_2 ring from Fig. 4.11, both taken with an applied field of 3 G. Left image was taken above the critical temperature at 2.20 K, middle image was taken below the critical temperature at 1.28 K. Right image is the taken by subtracting the signal from the middle image from that of the left. All images are plotted on a 3 G scale. The visible seems to faint for superconductivity and could be explained by a change in scan height after thermal cycling.

After the inconclusive imaging results above, the substrate was coated with 100 nm of gold. This conducting layer served to dissipate surface charge and help shield the probe from electrostatic effects. Figure 4.16 shows two scanning Hall images of the magnetic signal with the conductive coating, both taken at 1.28 K, far below the previously measured critical temperature. The image on the left was taken in a 0 G applied field, while that in the middle was taken in a 50 G applied field. The signal did not appear to change in magnitude between the two images, but the raw data from the 0 G image was subtracted from that of the 50 G image to isolate any superconducting features; this is plotted on a 5 G scale in the right hand image of Fig. 4.16. We expect a Meissner contribution from a 50 G applied field to be stark on a 5 G scale. The lack of features in the subtracted image indicates that there is no evidence of superconductivity at 50 G despite these images being taken at a temperature considerably lower than previously measured T_c. This experiment was repeated for a variety of applied fields between 1 and 50 G, none providing a meaningful difference after subtraction. These discouraging results led us to consider whether our bulk uranium ditelluride crystal had ceased to superconduct. The next aim of our project was to confirm its superconductivity.

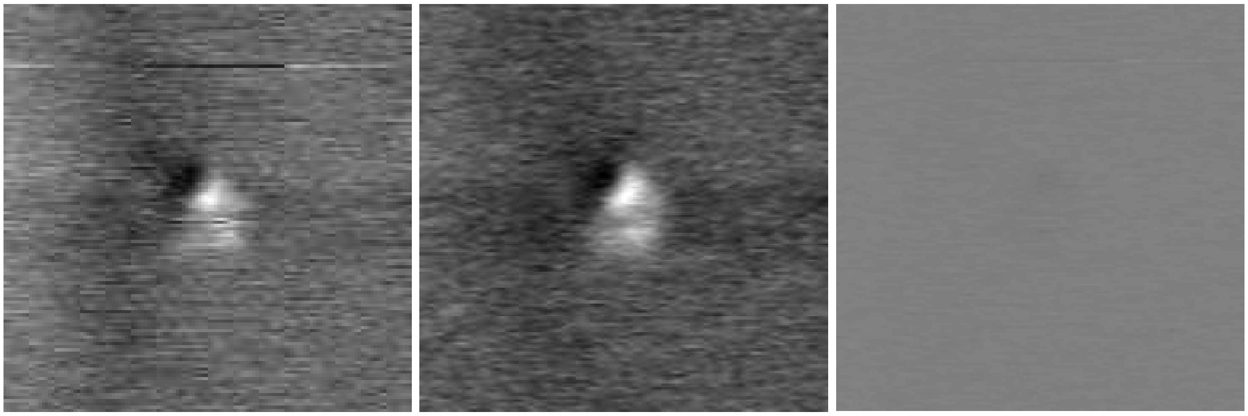

Figure 4.16: scanning Hall-probe images of UTe_2 ring from Fig. 4.11, both taken at 1.28 K, well below the critical temperature. Left image was taken with 0 G applied field and middle was taken with a 50 G applied field, both images are plotted on a .3 G scale. The right image is the difference between the two images on a 5 G scale. The lack of features in the right image indicates that the sample is not superconducting.

4.3 Crystal Quality and Other Issues

Fig. 4.17 shows an optical image of the bulk uranium ditelluride crystal from which the slab, ring, and Little-Parks devices were milled. The crystal is the dark feature near the edge of the substrate and the transparent portion is GE low-temperature varnish, which was used to fix the crystal to a silicon substrate.

To confirm superconductivity in this crystal, we lowered the Hall probe near its surface at room temperature using the digital microscope scheme. The typical approach and touch method (as will be described at the end of this section) was dangerous for the Hall probe because the crystal

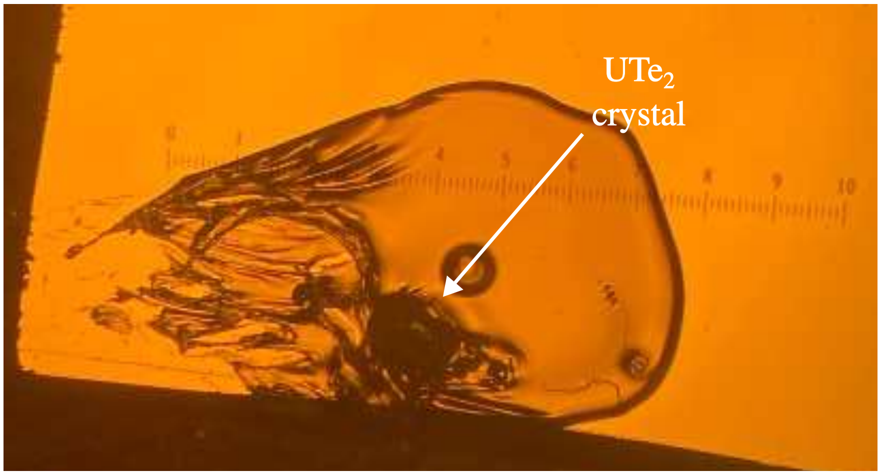

Figure 4.17: An optical photo of a millimeter scale UTe_2 crystal attached to a silicon substrate for a critical temperature measurement. The devices featured in this chapter were fabricated from this bulk crystal.

surface was uneven on the scale scale of hundreds of micrometers. We used the mirror and digital microscope system to fix the position of the probe to approximately two millimeters above the surface of the crystal, after which we closed the chamber and cooled to the base temperature of our system, well below the presumed critical temperature of the crystal. We then applied a magnetic field and measured the Hall response as a function of temperature. This data is represented in Fig. 4.17. Between 1.2 K and 1.6 K, the measured field was some fraction of the applied magnetic field. Above 1.6 K, the measured field increased rapidly before matching the applied field near 1.8 K (the exact temperature value depended on the magnitude of the applied field). This data is analogous to that of Fig. 4.6, and indicates a relatively high critical temperature for uranium ditelluride [100]. This gave confidence in the quality of our bulk crystals, but it drew fabrication and handling processes into question.

Exposure to Air

It is well-known that uranium ditelluride is highly sensitive to air [106, 123–126]. A recent study [124] on crystal growth techniques for uranium ditelluride concluded, “The possible oxidation process of UTe2 crystals can be inferred: when UTe2 crystals were exposed to the air, the outside surface in UTe2 crystals will be oxidized and split into strips due to the release of the stress.” The

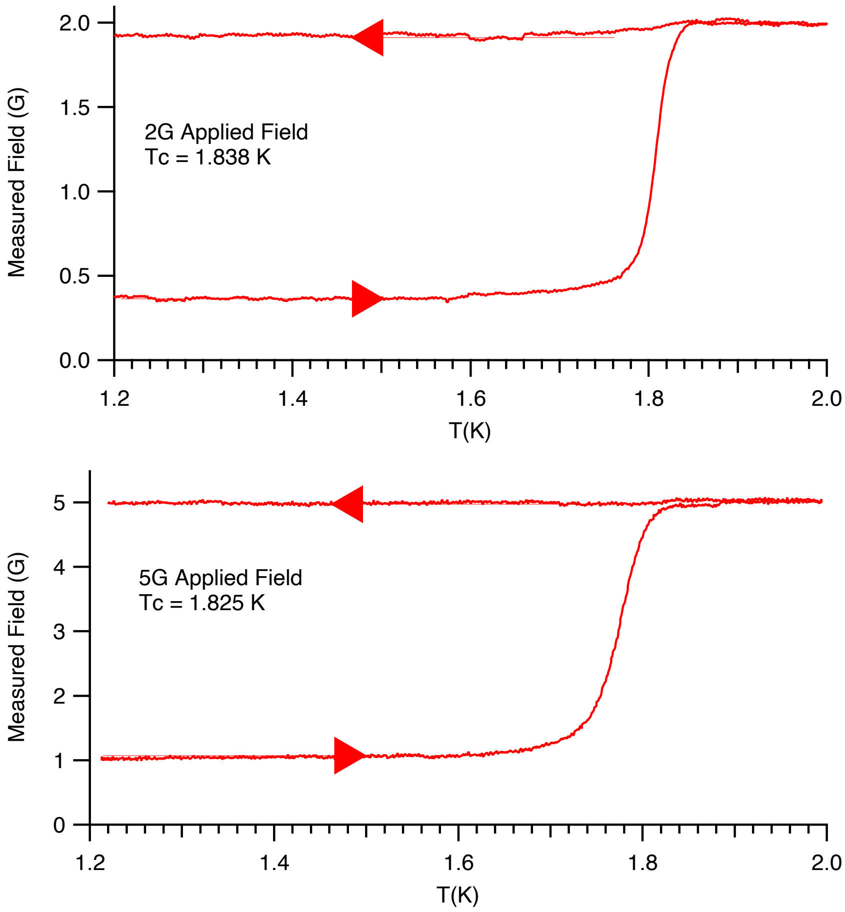

Figure 4.18: Critical temperature data of the UTe_2 crystal from Fig. 4.17. Top plot shows transition with a 2 G applied field, bottom plot shows transition with a 5 G applied field. Both indicate a T_c of just over 1.8 K.

depth of oxidation in this study was not reported, but oxidation of the surface was observed after a mere 25 s exposure to air.

This could explain the high critical temperature of 1.8 K for our bulk crystal as well as the failure of micrometer-scale devices to superconduct at 1.28 K. Our results are consistent with the oxidation of the outermost layer of both the bulk crystal and the devices, destroying superconductivity in those layers. In millimeter-scale bulk crystals, this likely leaves hundreds of micrometers of undisturbed material to exhibit a Meissner response. The relatively large superconducting region could dominate the Hall signal, leading to the observations of Fig. 4.18. However, micron-scale devices are possibly thin enough so that modest oxidation could penetrate the entire device. A reasonable counterpoint to this explanation lies in our earliest T_c measurements of a micrometer-scale planarized slab (see

Fig. 4.6). This device exhibited a critical temperature near 1.6 K. Perhaps when this device was fabricated, the oxidated layer on the surface of the crystal was very thin with respect to the size of the slabs that were lifted out, leaving most of the device capable of superconducting. The crystal has been stored in an inert argon glovebox since our collaborators received it; however, continued oxidation in an inert environment can be mediated by reactive intermediates formed during surface oxidation [127], self-sustaining oxidative reactions (autocatalytic) [128–130], or residual oxidation from trace air in the glovebox atmosphere.

Another possibility is that the oxidation occurs from handling the devices and not from the bulk crystal from which they are fabricated. This is less likely because our handling process improved greatly after our earliest measurements. We developed the following technique to limit the exposure of the uranium ditelluride device to air while preparing for a scanning Hall measurement: We start by mounting a "fake" sample to the microscope sample holder. This sample is a piece of silicon with the same dimensions as the substrate. It contains a de Bruijn pattern identical to that of the substrate but has no device. After mounting the substrate, we attach the microscope to the 4 K plate, where we can confirm various electrical connections to the scanning microscope head and related thermometry. We also balance the capacitor bridge used for touch sensing. Next, rigid posts that connect the microscope assembly to the 4 K stage are removed, allowing the microscope to hang from springs in an effort to further isolate vibration. The digital microscope is oriented to display a side view of both the Hall probe and fake substrate—this is useful for observing the probe as it approaches the sample vertically. The attocube nanopositioner is used to bring the probe within millimeters of the substrate and the digital microscope is repositioned to align the probe above the de Bruijn pattern. We then back the probe a few millimeters away from the substrate, reconnect the rigid posts, and remove the microscope from the 4 K plate. At this point, the real device is opened to air, and the following process is performed as quickly as safe handling allows: Optical photos are taken of the substrate through a microscope to record the device placement with respect to the de Bruijn pattern for positioning at cryogenic temperatures. The real substrate is then fixed to the sample holder and the microscope is mounted to the 4 K stage. Again, the rigid posts are removed, allowing the microscope to hang from springs. The digital microscope is used to monitor the probe as it approaches the surface of the substrate and is oriented over the de Bruijn pattern. The vertical position is noted and the probe is backed up a safe distance from the sample. The vacuum cans are attached to their various plates and vacuum system base, and the vacuum chamber is pumped. At this stage the sample is in a high-vacuum environment, ending the time-sensitive portion of the process. Next, the probe is retracted with the z-piezo bender and stepped to within an estimated millimeter of the surface. Once it has stepped, the z-piezo is used to extend the probe through its vertical motion with the touch sensor activated. If there is no touch, the z-piezo is retracted, the attocube advances the probe some fraction of the scan range of the z-piezo toward the surface, and the piezo again extends the probe through its range. While time consuming, this process ensures that the probe will contact the surface during a gentle extension of the z-piezo, preventing a crash. Once a touch is detected, the position is recorded and the attocube is used to back the probe one millimeter away from the surface, preventing a crash during the cool down due to thermal contraction. Carefully following this "rapid cooldown" process limits air exposure to approximately ten minutes.

4.3.1 Future Direction

If the issue with our devices is an oxidated layer on the bulk crystal, an avenue for future experiments could be to cleave the bulk crystal just before fabrication, ensuring a clean surface. Uranium ditelluride readily cleaves along the a-b plane [131], and in-vacuum cleaving is a common method for yielding oxide-free surfaces for device fabrication [132]. Although the delicate nature of spin-triplet superconductivity and instability of HQVs present significant experimental challenges, the promise held for topological quantum computation makes this a worthwhile endeavor. The fluxoid experiments successfully completed in Chap. 3 along with our initial attempts using UTe_2 represent an exciting path forward in the search for HQVs and realization of topological quantum computing.

Chapter 5

Chirality-Induced Spin-Selectivity Effect

> "Difficulties are meant to rouse, not discourage."
>
> —William Ellery Channing

5.1 Introduction

The Chirality-Induced Spin-Selectivity or CISS effect is garnering interest in spintronics as a medium for manipulating electron spin without the need for an external magnetic field or cryogenic temperatures [133–137]. The effect arises from the interaction between an electron's spin and the helical electric potential it experiences when traveling along the chiral axis of certain molecules or materials [138]. This interaction energetically favors one spin species over the other (with respect to the chiral axis), resulting in spin-dependent resistance and effective spin filtering. Although the precise details of the CISS effect are not fully understood, there are various useful models to aid in developing a quantitative understanding of the effect [134, 137–142].

A simple CISS model is that of an electron traveling in a helical path, defined by a chiral arrangement of ionic cores as shown in Fig. 5.1. As the electron passes by each core, it encounters a radial electric field emanating from it. This leads to a relativity-induced effective magnetic field $\mathbf{B_{rel}}$ of

$$\mathbf{B_{rel}} = \frac{\mathbf{v}}{c^2} \times \mathbf{E}_{\text{chiral}}, \tag{5.1}$$

where $\mathbf{v}$ is the velocity of the electron, $\mathbf{E}_{\text{chiral}}$ is the chiral electric field experienced by the electron, and c is the speed of light [138, 143]. Figure 5.2 shows the relative orientations of the electron's velocity and a nearby electric field due to an ion. The cross product in Eq. 5.1 indicates an induced magnetic field aligned with the chiral axis (c-axis in this diagram) [138]. The electron experiences a radial Lorentz force that confines it to circular motion with an upward drift velocity. Additionally,

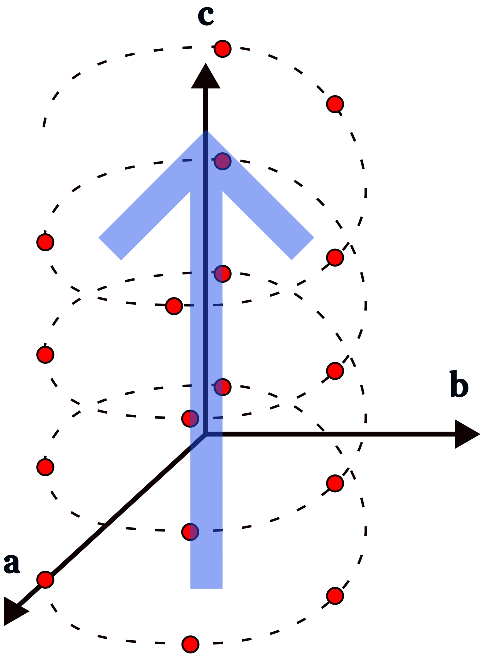

Figure 5.1: The red spheres represent a helical distribution of ionic cores. Electrons travel in a helical path defined by this arrangement of ions. The motion of the electrons can be considered as a circular motion with some overall drift velocity upward along the c-axis, denoted with the blue shaded arrow.

the magnetic moment of the electron behaves as a dipole, splitting the energy of the spin states and leading to spin-dependent conduction via the Zeeman effect $U = -\boldsymbol{\mu} \cdot \mathbf{B}$, where $\boldsymbol{\mu}$ is the magnetic moment.

A more sophisticated explanation of the CISS effect is closely related to the Rashba spin-orbit interaction; however, the origin differs [144–146]. The Rashba effect is an interaction between a charged particle's spin, momentum, and an external electric field. It adds the following term to its Hamiltonian,

$$\mathcal{H}_\mathrm{R} = \alpha_\mathrm{R} \left(\boldsymbol{\sigma} \times \mathbf{p} \right) \cdot \hat{\mathbf{E}}. \tag{5.2}$$

Here, α_R is the Rashba coupling coefficient which signifies the strength of the spin orbit coupling, σ is the Pauli Spin matrix, $\mathbf{p}$ is the momentum, and $\hat{\mathbf{E}}$ is a unit vector pointing in the direction of the electric field. The origin of the CISS mechanism is the radial electric field resulting from the geometry of the ionic cores, rather than the external field associated with the Rashba effect [145]. Since the momentum and electric field are fixed by the electron's travel and the arrangement of

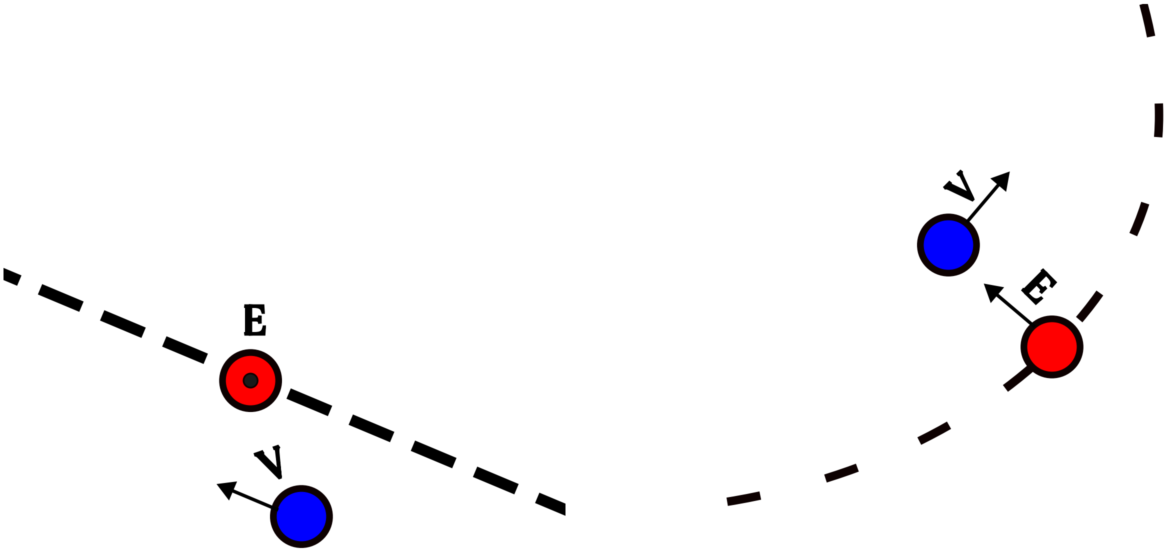

(a) Side-View **(b)** Top-Down

Figure 5.2: An electron (blue) passing by, and interacting with, an ionic core (red). (a) depicts a side view of the interaction, (a-c or b-c plane, for example, from Fig. 5.1) with respect to the chiral axis. (b) is a top-down view of the interaction, (a-b plane from Fig. 5.1). Dashed lines represent the helical path that defines the arrangement of atoms and the path that the electron travels.

ions, it is illuminating to apply a vector identity to eq. 5.2 to demonstrate the spin-dependence,

$$(\boldsymbol{\sigma} \times \mathbf{p}) \cdot \hat{\mathbf{E}} = \boldsymbol{\sigma} \times \left(\mathbf{p} \cdot \hat{\mathbf{E}}\right). \tag{5.3}$$

Thus, the energy is maximized (minimized) with a spin parallel (anti-parallel) to the drift velocity of the electron (blue arrow in Fig. 5.1).

The discovery of the CISS effect was the result of efforts to understand enantioselectivity in biochemical processes [138]. Enantiomers are pairs of chiral molecules—they have the same atomic makeup and connectivity, but are mirror images of each other [147]. The chiral nature of enantiomers leads to strikingly different properties between them. The mechanism by which biological systems distinguish between enantiomers, enantioselectivity, is a vast research area [148–150]. Electron transfer is a critical aspect of biochemical processes; thus, a possible mechanism for enantioselectivity is spin filtering. This idea gained traction as modest spin filtering was experimentally realized in gases composed of chiral molecules [151,152]. Spin filtering is quantified via spin-selectivity,

$$S = \frac{I_+ - I_-}{I_+ + I_-}.$$

Gas-phase experiments on CISS materials revealed spin selectivity of order 10^{-4}. However, recent experiments on chiral films have shown spin-selectivity nearly one thousand times higher [138, 153–155], encouraging continued research.

Much of the existing body of research is related to molecular CISS; however, an emerging and promising class of CISS research is in single-crystal materials. The relative ease with which single-crystal materials can be utilized in device physics [156] offers a significant advantage in the field of spintronincs. Our discussion will be focused on one such material.

5.2 Methods of detecting CISS

Spin-selectivity exhibited in the CISS effect is subtle and difficult to detect. This section will detail a handful of methods with which the effect has been experimentally verified, as well as a novel method proposed by our group.

5.2.1 Spin Hall Effect

The spin Hall effect is a phenomenon that can be exploited to detect spin filtering [157] and is employed in two of the detection methods described below. It arises from spin-orbit coupling (SOC) and causes moving electrons to deflect laterally on the basis of their spin as seen in Fig. 5.4. This leads to spin accumulation at the transverse edges of a high-SOC material [158]. The strength of this effect scales with the strength of the spin-orbit interaction in the material.

Spin Hall Detection

In this approach, a slab of the CISS material is fabricated with the chiral axis along the longitudinal direction. Metallic leads are attached to the ends and a detection electrode of high-SOC material (i.e. tungsten) is deposited on top of the slab near its middle. A potential difference is applied across the leads as shown in Fig. 5.4, causing a charge current to flow through the

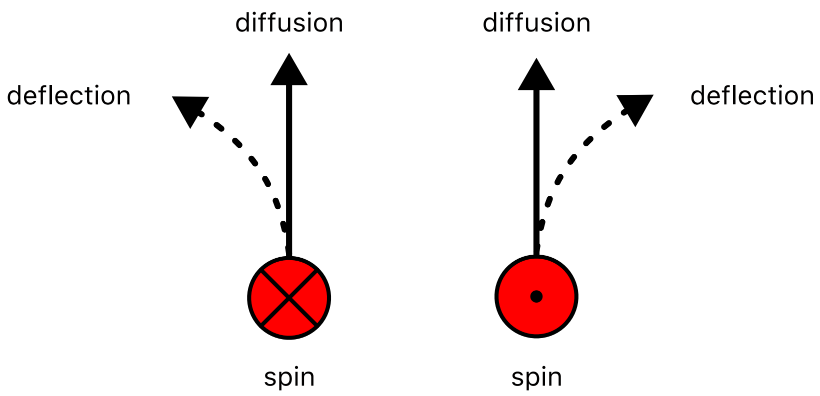

Figure 5.3: A depiction of the spin Hall effect. The electrons have spins have opposite spins, pointing in to and out of the page. They are each diffusing upward with some velocity. The dashed trails represent the path traveled by the electrons due to the spin Hall effect.

device [157, 159]. Electrons from the induced current will diffuse upward into the detection lead. When the spin of these diffusing electrons interacts with the effective electric field of the high-SOC material, they will be deflected to transverse edges, depending on their spin. That is, electrons of opposite spin species will be deflected to opposite edges of the electrode. Without spin-filtering, no voltage difference is detected (see Fig. 5.5). However, in the presence of spin-filtering, electrons disproportionately accumulate on one edge, leading to a measurable voltage difference.

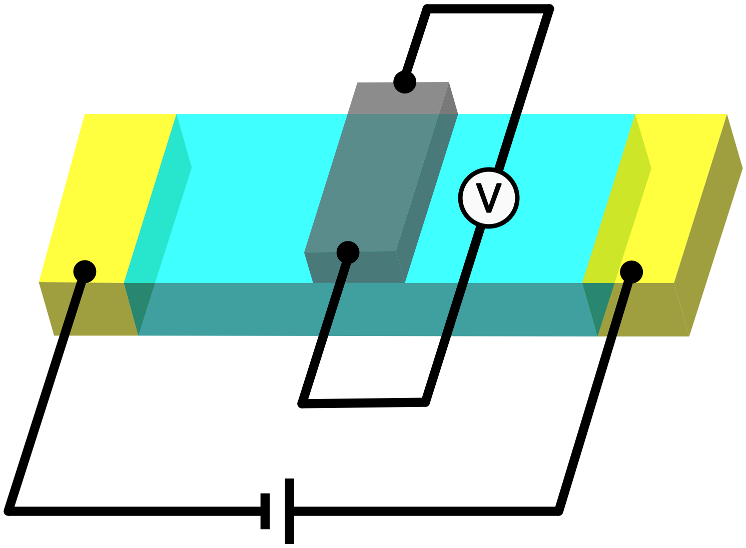

Figure 5.4: A typical device for standard Spin Hall detection. A voltage difference is established across the gold contacts, forcing a current through the CISS material (cyan). The Spin Hall effect leads to a measurable voltage difference across the high-SOC detection electrode (gray). The yellow segments are gold leads.

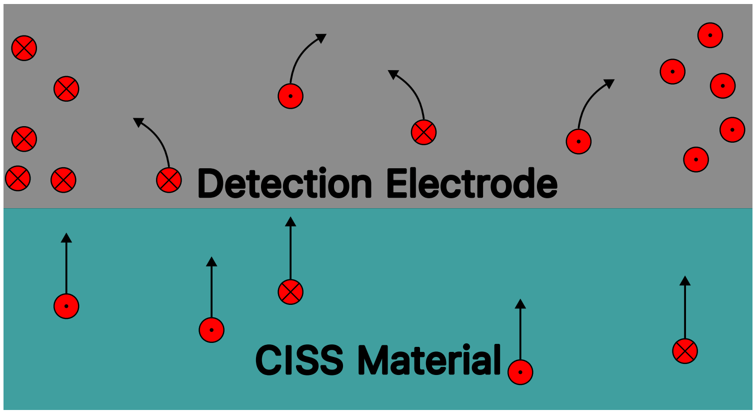

Figure 5.5: A two-dimensional cross section of the high-SOC detection electrode (gray) and the CISS material (cyan) along the c-axis. As electrons diffuse upward from the CISS material into the electrode, they are subject to spin-dependent deflection.

Inverse Spin Hall Detection

Inverse spin Hall detection works for the same device as the spin Hall detection method [157]. Thus, these devices have the advantage of offering two distinct CISS measurement methods. For inverse spin hall detection, a potential difference is established across the transverse edges of the detection electrode, causing a charge current to flow from one end to the other. As that current diffuses into the slab device below, one spin species can easily travel along the chiral axis, while the other is inhibited by the CISS effect, leading to a potential difference in the longitudinal direction of the slab [157, 159–161]. A schematic of this detection method is shown in Fig. 5.6.

5.2.2 Electromagnetochiral Resistance Detection

For electromagnetorchiral (EMC) resistance detection, a slab of CISS material is fabricated, again with the c-axis running along the longitudinal direction. Electrodes are attached in a four-probe geometry and a magnetic field is applied along the device axis. A current is passed through the sample and its voltage is measured with a lock-in amplifier. The direction (with respect to the horizontal) and magnitude of H are varied to produce resistance plots as a function of I, H. The resistance in the slab can be represented as $R(H, I) = R_0(1 + \mu_0 \gamma \vec{H} \cdot \vec{I}) = R_0(1 + R_{\text{EMC}})$ [162], where μ_0 is the vacuum permeability constant and γ is the so-called R_{EMC} coefficient. Thus,

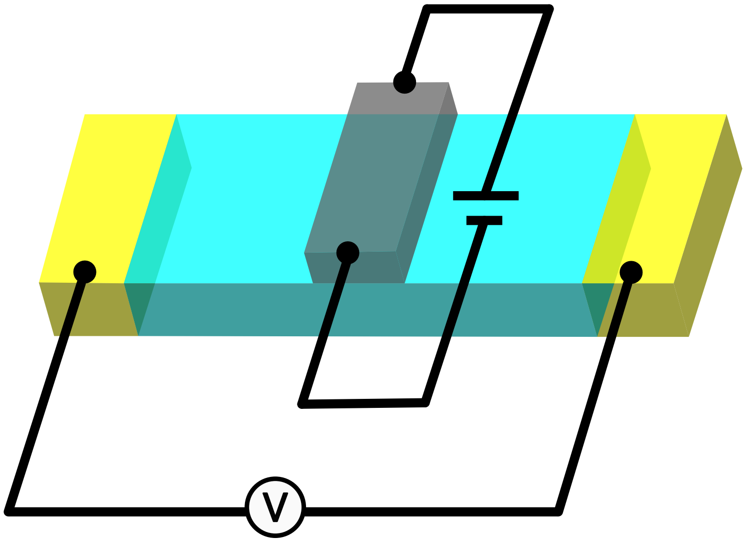

Figure 5.6: A typical device for inverse Spin Hall detection. A voltage difference is established across the detection electrode and the spin Hall effect generates a voltage across the gold leads. CISS material is cyan (with chiral axis along longitudinal direction) and yellow segments are gold leads. Gray segment is high-SOC detection electrode.

a drop in resistance is associated with anti-parallel H and I, while an increase in resistance is associated with parallel H and I. EMC resistance is a manifestation of nonreciprocal electron transport [162]. Ordinary metals have magnetoresistance that is symmetric in H, I [163], that is, $R(H, I) = R(-H, I) = R(H, -I)$.

An advantage of this method is that many leads can be attached along the slab, enabling high-resolution measurements of the CISS effect that are only limited by the minimum distance by which leads can be attached. This is a powerful tool for measuring chiralities between grains [162, 164].

5.2.3 Scanning Hall Detection

Our scanning Hall-probe microscope may provide a CISS detection technique that has not yet been exploited. The proposed device for this method would be the same previously discussed slab depicted schematically in Fig. 5.7.

For this experiment, an unpolarized current is passed through the slab along its chiral axis. This applied current becomes macroscopically polarized across a short length scale—the exact distance is not known for our material $NaCu_5S_3$, which will be discussed in the following section. This

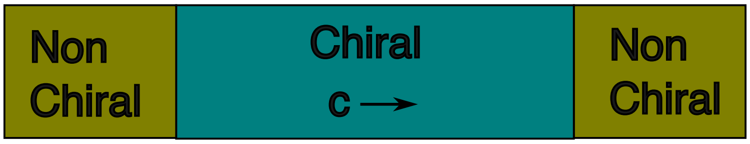

Figure 5.7: Schematic representation of chiral (C) and non-chiral (NC) regions of a slab device. The chiral region is composed of CISS material while non-chiral end segments are gold ramps to allow conduction through the slab.

macroscopic alignment of spins depicted in Fig. 5.8 leads to a measurable magnetic field. This spin arrangement for a slab geometry has a simple magnetic analogue—the constant magnetization vector oriented along the c-axis is reminiscent of a bar magnet and should lead to a similar dipolar magnetic signature. The current flowing through the slab will create an additional magnetic field, obscuring the CISS field. The current-induced field will point out of the substrate's surface on one hemisphere and into that surface on the other hemisphere. A critical step to isolate the CISS field is to model the field due to current passing through the slab and subtract it from the raw Hall data.

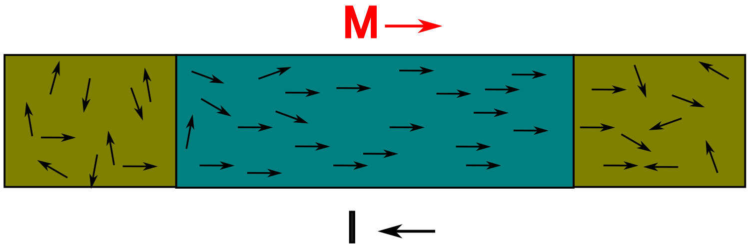

Figure 5.8: Macroscopic spin alignment and magnetization for current-carrying CISS slab.

5.3 Experiments

The experimental efforts of our group have focused on ferrichiral single-crystal sodium pentacupride sulfide ($NaCu_5S_3$). This material is an exciting candidate due to its chiral structure, high-quality growth techniques (which hold potential for thin-film growth), and relatively high spin-orbit coupling [165]. Additionally, the material is theorized to have switchable Dresselhaus spin-splitting which provides a handle to manipulate the spin-polarization [165].

The material was grown by collaborators in the Kenneth Poeppelmeier group at Northwestern University using a solvothermal crystal-growth technique with ethanediamine as the solvent [165]. They generated this specific sodium thiocuprate by melting appropriate ratios of sodium sulfide, copper sulfide, and sulfur powder. Figs. 5.10, 5.9 depict a slab of candidate material fabricated by CU Boulder collaborators, the same team responsible for uranium ditelluride devices. The slab in Fig. 5.9 is approximately 12 μm wide and 27 μm long, as indicated by the scale bar.

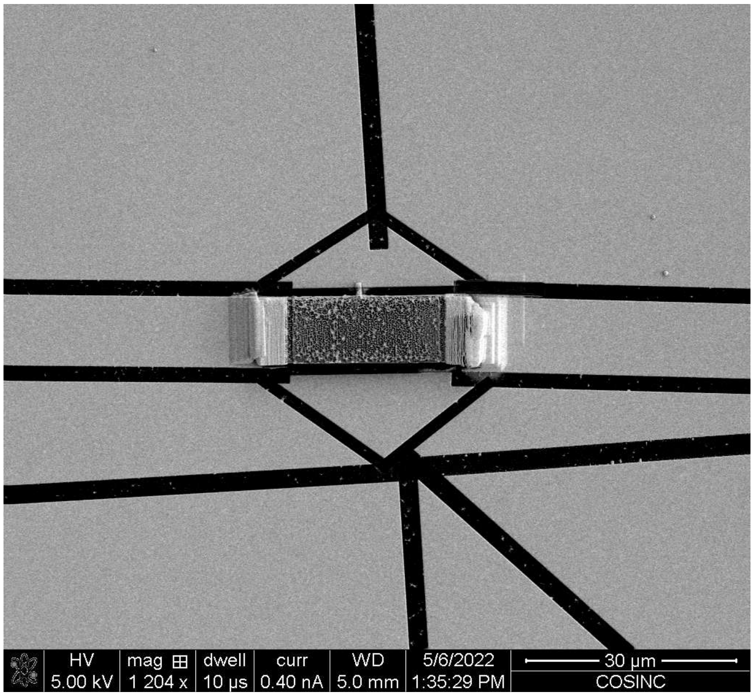

Figure 5.9: An electron beam image of a 12 μm × 27 μm $NaCu_5S_3$ slab with 30 μm scale bar. Grainy texture of device could be due to material redeposition during fabrication [8].

5.3.1 Device Fabrication

Our collaborators lifted a plate from a mesoscopic rod of $NaCu_5S_3$ before fabricating the slab depicted in Fig. 5.9. The liftoff and slab fabrication were performed with a focused ion beam mill that contains a high-resolution scanning electron microscope and an ion source for sample milling.

The lift-out process is well documented in Figs. 5.11, 5.12. It should be noted that these images correspond to a lift-out from a macroscopic crystal of UTe_2, rather than the mesoscopic sodium

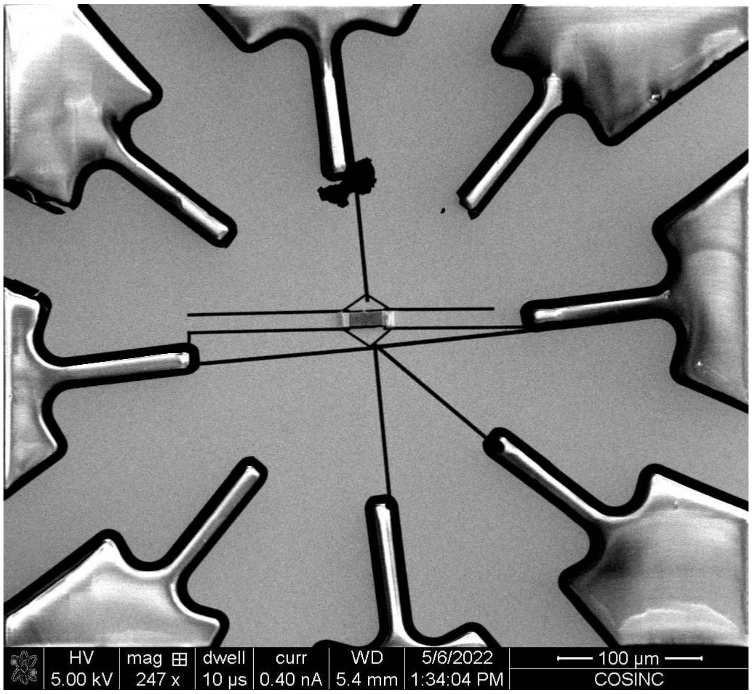

Figure 5.10: An electron beam image of our $NaCu_5S_3$ slab with 100 µm scale bar. Inverse clover pattern is a layered resist structure of photoresist and liftoff resist for the conducting channel evaporation.

pentacupride sulfide rods used to fabricate CISS devices. The methodology is identical, thus these images are appropriate for a discussion of the fabrication process, which is particularly relevant for this chapter. The solvothermal crystal growth technique utilized for our crystals yields a landscape of mesoscopic rods and platelets. The chiral axis (c-axis) is oriented along the longitudinal direction for rods, and perpendicular to the plane for platelets. The rods are better-suited for device fabrication due to the orientation of their chiral axis.

Fabrication starts with a survey of rod structures for a suitable candidate with appropriate size and surface smoothness. Once such a rod has been identified, a micrometer-scale slab is defined by milling a trench directly above and below the slab as shown in the left image of Fig. 5.11. After the trenches have been formed, a nanomanipulator is attached to the top surface of the slab. The ion mill is then used to disconnect the platelet from the side walls of the trench. Lastly, a cut is made along the bottom of the slab to completely free it from the rod. The nanomanipulator is then used to lay the slab onto a substrate that is compatible with scanning Hall microscopy. The slab is “welded” to the surface of that substrate using the focused ion beam and a platinum-containing

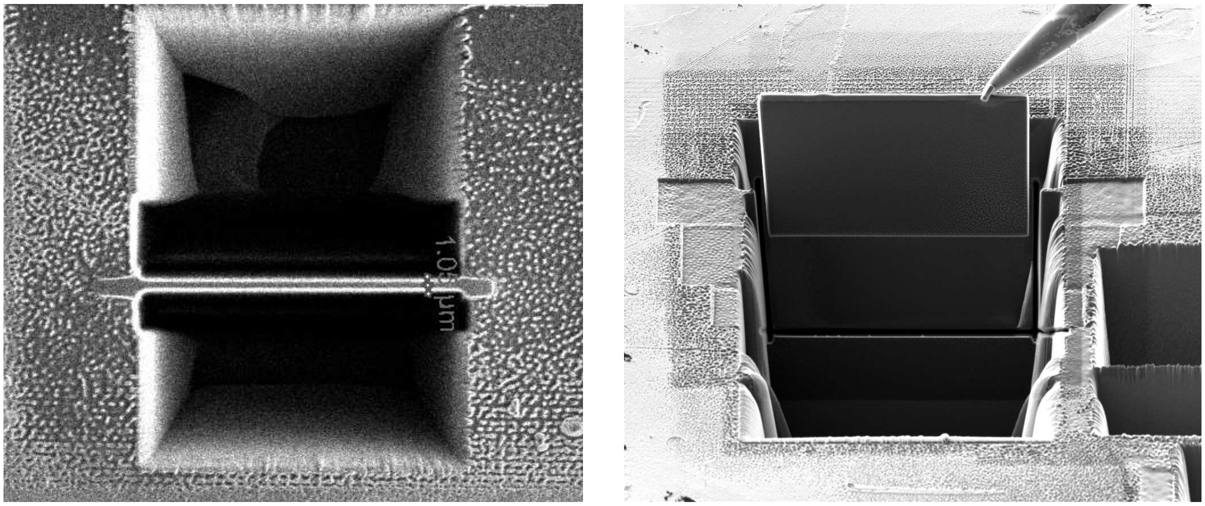

Figure 5.11: Scanning electron microscope images of the process of lifting a slab out of a macroscopic UTe_2 crystal. Left image shows a slab that has been defined by milling out two trenches—one directly above and one directly below the platelet. Right image shows the same slab that has been attached to a nanomanipulator for liftoff. After attaching the nanomanipulator, three additional cuts are made to the slab to free it from the side walls as well as the bottom of the trench.

precursor gas. With the slab anchored to the surface, our collaborators mill it into the desired device geometry with a series of cuts. First, there are high-powered cuts, each removing large amounts of material and forming a crude device shape. These are followed by low-power cuts with higher resolution, allowing them to hone in on an ideal device geometry. The next task is to

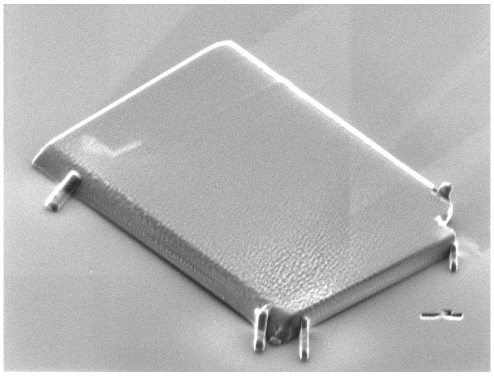

Figure 5.12: Scanning electron microscope image of a slab that has been lifted out and welded to the surface of a silicon substrate. It is now ready to be milled into a device.

provide an infrastructure to pass current through the slab. To start, platinum is deposited in a ramp that connects the substrate's surface to the top surface of the slab. The deposition rate is relatively low and imaging capabilities are limited, making a ramp with a smooth height gradient difficult to achieve.

Up to this portion of fabrication, the wafer is coated in layers of liftoff resist and conventional photoresist. There is a small resist-free *target area* in which the device is placed, as well as openings for electrical traces to provide current to the device, as shown in Fig. 5.10. The resist layers are the outermost film with varying darkness and texture that form the outline of a clover pattern. After the ramps are deposited, chrome and gold are evaporated over the entire substrate to form the conducting paths. Chrome serves as the adhesion layer that helps mitigate the lattice mismatch between gold and silicon [166]. The gold layer is the primary conduction layer, while a thin chrome-gold oxide promotes wetting. These evaporations are performed under a submicro-Torr vacuum. Typical film thicknesses are approximately 2 nm of chrome and 100 nm of gold.

After evaporation, the photoresist is lifted off in a DMSO bath at 155 °C. This disconnects the evaporated film that covers the target area and traces from that which was deposited on top of the photoresist. The target area is wider than the slab, so additional FIB fabrication steps must be taken to confine conduction through the slab and remove the conducting layer deposited on top of it. The first cuts are made along the longitudinal edges of the slab and ramp into the silicon. This disrupts any conduction from the slab to the silicon or conducting layer on its transverse sides (top or bottom from the perspective of Fig. 5.9). Next, cuts are made in the target area to electrically isolate various leads. This forces the current to pass through the device. Lastly, a gentle (low power) and unfocused cut is made directly on top of the slab to mill through the top layer of gold and chrome, revealing the CISS slab beneath. The slab and ramp cuts can be clearly seen in Fig. 5.9 and the current-confining cuts can be seen in Fig. 5.10.

5.3.2 Slab Measurement

In a typical scanning Hall probe measurement, we pass an alternating current through the Hall probe and measure the incoming Hall signal with a lock-in amplifier. For this experiment, a 20 μA DC current was applied to the Hall probe, while a 1 mA AC current was driven through the magnetic sample. The previously mentioned DX centers that plague Hall probe microscopy introduce low-frequency (Hz-scale) resistance noise to the probe; however, the Hall voltage and sensitivity remain largely unaffected by these fluctuations. Applying an AC signal to the sample yields an alternating magnetic field that generates an oscillating Hall voltage at the driving frequency. This allows the lock-in amplifier to easily detect the Hall voltage and disregard the low-frequency DX center noise as well as a DC voltage offset due to asymmetry in the probe.

5.3.3 Disentangling CISS Physics

As was previously discussed, this experiment should yield a magnetic signature from passing current through the slab as well as one from any spin-polarization of the CISS effect. Figure 5.13 shows a raw scanning image of the device. The field from the current-carrying slab is evident in the division into two distinct regions. The portion of the image above the slab shows a bright positive field, while that below the slab shows a dark negative field.

The next task was to model and subtract the field due to the current distribution to potentially reveal a CISS magnetic signature buried beneath it. To this end, a numerical expression for the field at some fixed scan height across the entire scan range was developed via the Biot-Savart law. A line profile was taken from the raw data over the conducting leads and far from any potential CISS signature. The conducting leads have the same width as the CISS slab. This line profile gives magnetic field as a function of the y-position for the scan height used in our experiment, and the Biot-Savart expression was fitted to the line profile. The line profile and fit can be seen in Fig. 5.14. The fit matched the experimental data well from the y positions of approximately −5 μm to 30 μm. The fit deviates from the line profile from −30 μm to −5 μm while remaining qualitatively similar.

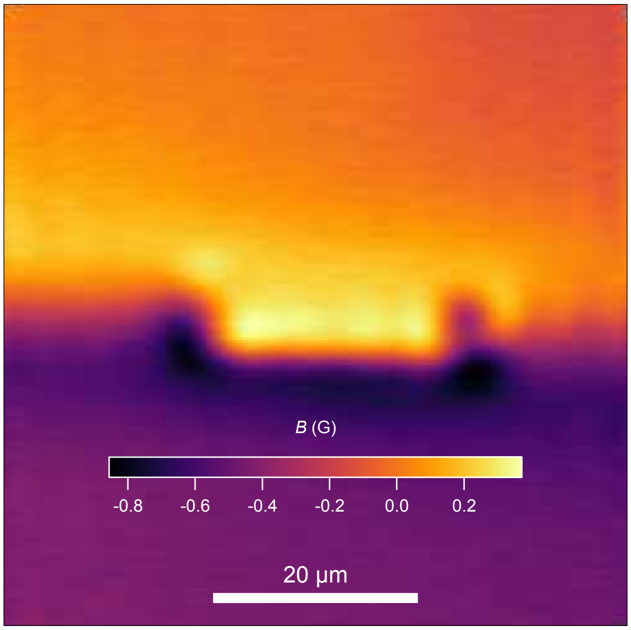

Figure 5.13: Raw Hall probe image of CISS slab. Orange (positive) and purple (negative) regions align with expectations for the field due to a current-carrying slab. 1 mA passing through slab for this scan.

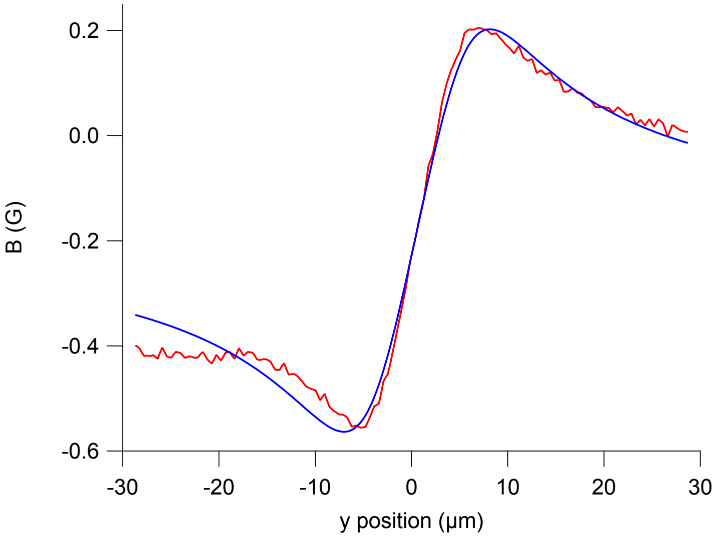

Figure 5.14: Biot Savart fit (blue) vs. line profile data (red). See Fig. 5.15 for the image after this fit was subtracted.

.

This fitted field was subtracted from the two-dimensional raw image. Figure 5.15 shows the magnetic image after subtraction. We expected an underlying dipolar magnetic field—a strong positive field at one end, a strong negative field at the other end, and smooth transition in between. Instead, a bright positive field can be seen over the middle of the bar, and dark negative spots over either end. The Biot-Savart fit and subtraction gave mixed results—the fit effectively subtracted off the field due to the current; the background looks virtually the same over any region far from the slab, however, no clear CISS signature was revealed.

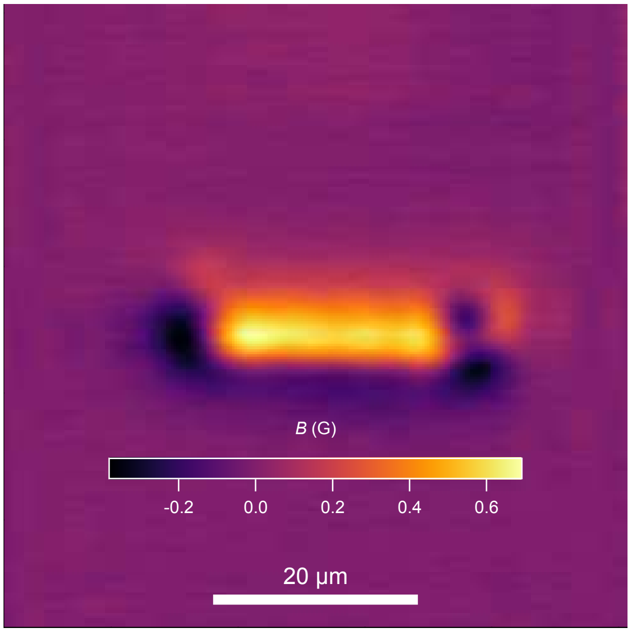

Figure 5.15: Hall probe image of CISS slab with field due to current subtracted off. Uniform background indicates successful subtraction, however the slab exhibits no CISS magnetic signature.

This result prompted a reexamination of the slab fabrication process. A possible explanation for the unexpected signal on either end of the slab is an irregularity in the conducting path. For example, the current may have flowed into the platinum ramps and through the bottom of the slab, or even the silicon substrate itself (a doped Monsanto wafer with resistivity between $4 - 10\,\Omega\,\mathrm{cm}$). Another possibility is that the conducting layer on top of the platinum is discontinuous, forcing the current through an unintended path. These potential issues stemmed from the ramp, leading us to develop a device for which the CISS physics is a considerable distance from the ramps.

5.4 U-Shaped Sample

To isolate CISS physics from magnetic effects due to the ramp, a new device geometry was proposed. We refer to it as the U-shaped device due to its resembelance to a block letter “U”. It is composed of two vertical branches connected by a horizontal branch. The longitudinal directions of the two vertical branches are non-chiral a- or b-axes, while that of the horizontal branch is the chiral c-axis. A schematic of this geometry and its anticipated spin alignment are shown in Fig. 5.16. Unpolarized current climbs a ramp and enters in the leftmost vertical branch. The current remains unpolarized as this branch is not chiral. As the current flows through the horizontal branch, it becomes spin polarized along the direction of travel due to the CISS effect. This polarization remains throughout the horizontal branch. Finally, the current travels down the remaining branch in which spin-scattering returns it to its unpolarized state.

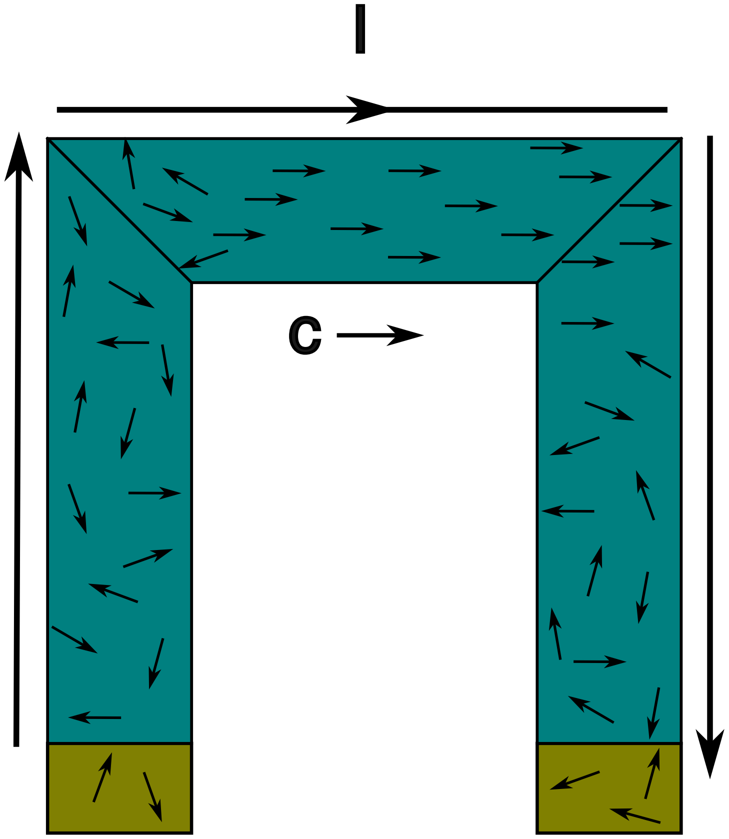

Figure 5.16: Macroscopic spin alignment for proposed u-shaped sample. The arrows represent the orientation of the electron's spin—unpolarized on the outer legs corresponding to the a- or b-axis, and polarized across the middle leg that corresponds to the c-axis. Conducting ramps are shown in yellow on the bottom edge of each leg.

For this device, the CISS signature occurs across the middle branch, tens of micrometers away from any complicated current dynamics from the platinum ramps. Additionally, the long arms along the non-chiral axes provide a suitable region for a line profile of our magnetic image for a Biot-Savart fit. A finite element method simulation was performed to produce qualitative predictions of the magnetic fields from the charge-current distribution as well as the CISS effect; these simulations are featured in Fig. 5.17. Both align with expectation—the left image shows alternating positive and negative magnetic fields, consistent with the direction of the current flow, and the right image shows the expected dipolar field arising from spin polarization.

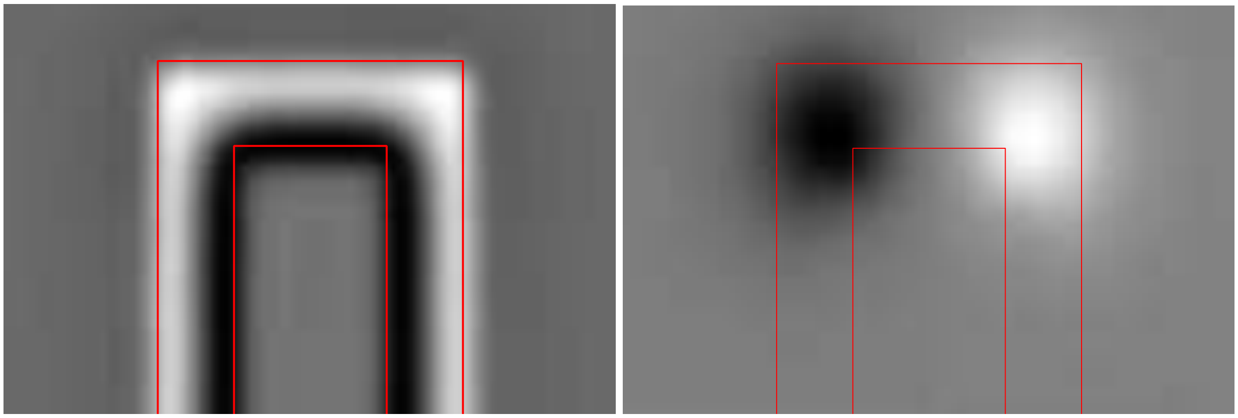

Figure 5.17: A FreeFEM simulation intended to provide a qualitative overview of the field due to the current density alone.

The realization of a U-shaped device has proven to be a challenge in microfabrication. Sodium pentacupride sulfide is a relatively difficult material for FIB milling, differences in quality and success rates are striking compared to those of more forgiving materials (such as uranium ditelluride). Fabrication has been afflicted by charge accumulation (obscuring the device from scanning electron microscope images and even causing it to move) [167], substantial redeposition during ion milling [8], and the brittle nature of the material. This has led our collaborators to search for a new fabrication method. Recent success in fabricating simple devices has been achieved with a method in which the device is milled while suspended above the substrate. This process mitigates strain and charge accumulation effects, renewing hope in a complicated device geometry.

Figure 5.18 shows a comparison of slab devices fabricated with the new (left) and previous (right) FIB techniques. In spring 2025, we developed custom scanning substrates for U-shaped devices for a future fabrication trip. These substrates consist of a label, a de Bruijn pattern, and gold leads that could be wire-bonded to our microscope's paddles to supply current to the device.

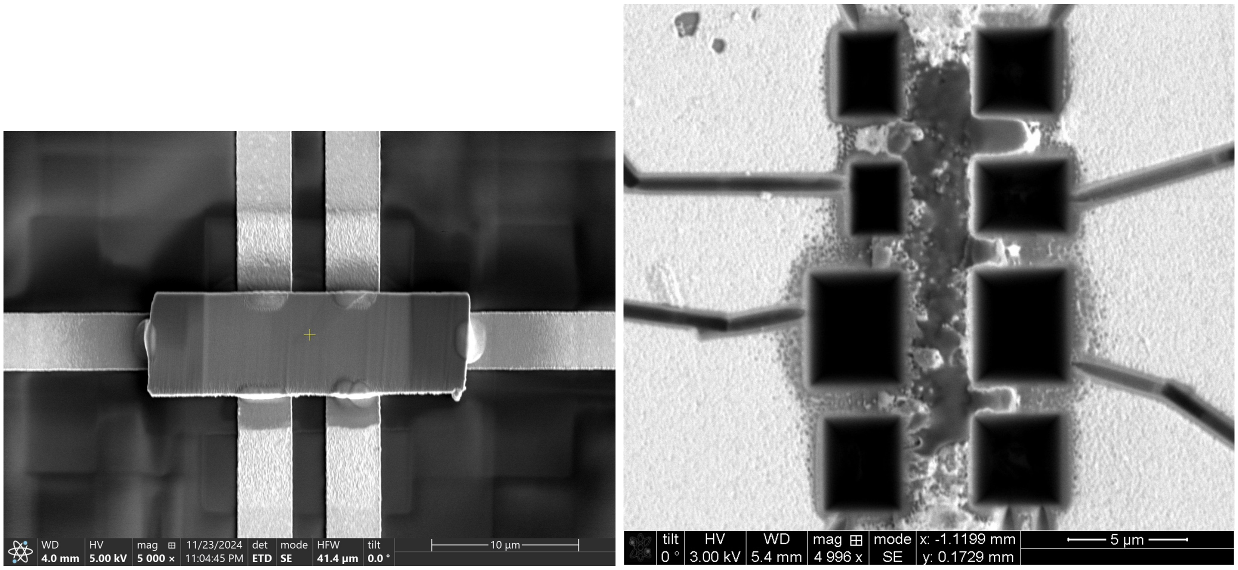

Figure 5.18: Two slabs of $NaCu_5S_3$ that were fabricated with different methods. The slab on the left hand side was fabricated with the new FIB technique (informed by [8]) in which the slab is milled above the substrate. The slab on the right was fabricated with the previous technique in which the slab was welded to the scanning substrate before being milled into the final device. The difference in quality between the two methods is striking.

In closing, the CISS detection has proved to be subtle and difficult to detect. We have proposed a new detection method that relies on magnetic imaging. Additionally, we have detailed an optimal sample geometry in which any spin-polarization associated with the CISS effect is separated from possible magnetic signatures from non-uniform current distribution in the conducting ramps.

Bibliography

[1] H. K. Onnes. Further experiments with liquid helium. c. on the change of electric resistance of pure metals at very low temperatures, etc. v. the disappearance of the resistance of mercury. *Leiden Communications*, 119b:122–124, 1911. Reprinted in *Communications from the Physical Laboratory of the University of Leiden*.

[2] J. Watson. Growth of low disorder gaas/algaas heterostructures by molecular beam epitaxy for the study of correlated electron phases in two dimensions, 2015.

[3] H. Fujibayashi, G. Nakamine, K. Kinjo, S. Kitagawa, K. Ishida, Y. Tokunaga, H. Sakai, S. Kambe, Ai Nakamura, Y. Shimizu, Y. Homma, D. Li, F. Honda, and D. Aoki. Superconducting order parameter in UTe2 determined by knight shift measurement. *Journal of the Physical Society of Japan*, 91(5):053705, 2022.

[4] J. Jang, D. G. Ferguson, V. Vakaryuk, R. Budakian, S. B. Chung, P. M. Goldbart, and Y. Maeno. Observation of Half-Height Magnetization Steps in Sr2RuO4. *Science*, 331(6014):186–188, 2011.

[5] A. Pustogow, Y. Luo, A. Chronister, F. Jerzembeck, A. P. Mackenzie, C. W. Hicks, N. Kikugawa, S. Raghu, E. D. Bauer, and S. E. Brown. Constraints on the superconducting order parameter in Sr2RuO4 from oxygen-17 nuclear magnetic resonance. *Physical Review B*, 104(2):024501, 2021.

[6] A. Pustogow, Y. Luo, A. Chronister, Y. Su, D. A. Sokolov, F. Jerzembeck, A. P. Mackenzie, C. W. Hicks, N. Kikugawa, S. Raghu, E. D. Bauer, and S. E. Brown. Evidence for even parity unconventional superconductivity in Sr2RuO4. *Nature*, 574(7780):72–75, 2019.

[7] B. Roberts, R. Budakian, and M. Stone. Numerical study of the stability regions for half-quantum vortices in superconducting Sr2RuO4. *Physical Review B*, 88(6):064505, 2013.

[8] M. D. Bachmann. *Manipulating Anisotropic Transport and Superconductivity by Focused Ion Beam Microstructuring*. PhD thesis, University of St Andrews, 2019.

[9] D. van Delft and P. Kes. The discovery of superconductivity. *Physics today*, 63(9):38–43, 2010.

[10] H. K. Onnes. On the measurement of very low temperatures. xii. comparison of the platinum resistance thermometer with the gold resistance thermometer. *Proceedings of the Koninklijke Nederlandse Akademie van Wetenschappen, Series B*, 9:213–224, 1906. Accessed: 2025-04-22.

[11] J. L. Sengers. A gas that sinks in a liquid—the first helium experiment published by kamerlingh onnes. *Journal of physics. Condensed matter*, 21(16):164222–164222, 2009.

[12] W. Meissner and R. Ochsenfeld. Ein neuer effekt bei eintritt der supraleitfähigkeit. *Naturwissenschaften*, 21(44):787–788, 1933.

[13] A. M. Forrest. Meissner and ochsenfeld revisited. *European journal of physics*, 4(2):117–120, 1983.

[14] M. Tinkham. *Introduction to Superconductivity*. Dover Publications, Garden City, NY, 1996.

[15] F. London and H. London. The electromagnetic equations of the supraconductor. *Proceedings of the Royal Society of London. Series A, Mathematical and Physical Sciences*, 149(866):71–88, 1935.

[16] F. London. *Superfluids*. Dover Publications, Garden City, NY, 1951.

[17] J. C. Maxwell. *A Treatise on Electricity and Magnetism*. Oxford University Press, Oxford, 2nd edition, 1873.

[18] J. Bardeen, L. N. Cooper, and R. Schrieffer. Theory of superconductivity. *Physical Review*, 108(5):1175–1204, 1957.

[19] R. G. Chambers. The anomalous skin effect. *Proceedings of the Royal Society of London. Series A, Mathematical and Physical Sciences*, 215(1121):481–497, 1952.

[20] J. M. Ziman. *Principles of the Theory of Solids*. Cambridge University Press, New York, 1964.

[21] A. B. Pippard. An experimental and theoretical study of the relation between magnetic field and current in a superconductor. *Proceedings of the Royal Society*, 1952.

[22] T. E. Faber and A. B. Pippard. The penetration depth and high-frequency resistance of superconducting aluminium. *Proceedings of the Royal Society*, 1955.

[23] V. L. Ginzburg and L. D. Landau. On the theory of superconductivity. *Zhurnal Eksperimental'noi i Teoreticheskoi Fiziki*, 20:1064–1082, 1950. English translation in: L. D. Landau, *Collected Papers*, Pergamon Press, 1965, pp. 546–568.

[24] C. J. Gorter and H. B. G. Casimir. On supraconductivity. *Physica*, 1:306–320, 1934.

[25] F. London. On the problem of the molecular theory of superconductivity. *Physical Review*, 74(5):562–573, 1948.

[26] A. Sommerfeld. Atombau und spektrallinien. *Verhandlungen der Deutschen Physikalischen Gesellschaft*, 13:272–284, 1915.

[27] C. Kittel. *Introduction to Solid State Physics*. John Wiley & Sons, Hoboken, NJ, 9th edition, 2018.

[28] P. Mangin, R. Kahn, and T. Ziman. *Superconductivity : an introduction*. Springer eBook Collection. Springer, Cham, Switzerland, 2017.

[29] J. Bardeen, L. N. Cooper, and J. R. Schrieffer. Theory of superconductivity. *Physical Review*, 108(5):1175–1204, 1957.

[30] M. Sigrist and K. Ueda. Phenomenological theory of unconventional superconductivity. *Reviews of modern physics*, 63(2):239–311, 1991.

[31] S. Das Sarma, C. Nayak, and S. Tewari. Non-abelian statistics of half-quantum vortices in p-wave superconductors. *Physical Review B*, 73(22):220502, 2006.

[32] S. B. Chung, H. Bluhm, and E. Kim. Stability of half-quantum vortices in $p_x + ip_y$ superconductors. *Physical Review Letters*, 99(19):197002, 2007.

[33] A.A. Abrikosov. On the Magnetic Properties of Superconductors of the Second Group. *Soviet Physics JEPS*, 1957.

[34] S. J. Bending. Local magnetic probes of superconductors. *Advances in Physics*, 48(4):449–535, 1999.

[35] B. Raes. *Scanning Hall Probe Microscopy of Vortex Matter in Single- and Two-Gap Superconductors*. Phd thesis, Katholieke Universiteit Leuven, 2016. Available at KU Leuven Lirias repository.

[36] P. G. de Gennes. *Superconductivity of Metals and Alloys*. Westview Press, Boulder, CO, 1999.

[37] D. Morvic and D. Betko. Planar hall effect in InP/InGaAs heterostructure hall sensors. *Sensors and Actuators A: Physical*, 120(1):130–133, 2005.

[38] S. Giugni and T. L. Tansley. Comment on the compositional dependence of bandgap in algaas and band-edge discontinuities in algaas-gaas heterostructures. *Semiconductor Science and Technology*, 7(8):1113–1116, 1992.

[39] M. J. Manfra. Molecular beam epitaxy of ultra-high-quality AlGaAs/GaAs heterostructures: Enabling physics in low-dimensional electronic systems. *Annual Review of Condensed Matter Physics*, 5:347–373, 2014.

[40] A. Kindness, P. Palacios, T. DeTemple, and R. R. LaPierre. Enhanced optical absorption of GaAs near band edge transitions in GaAs/AlGaAs core shell nanowires: Implications for nanowire solar cells. *ACS Applied Nano Materials*, 6(2):1252–1259, 2023.

[41] R.H. Harrell, J.H. Thompson, D.A. Ritchie, M.Y. Simmons, G.A.C. Jones, and M. Pepper. Very high quality 2DEGs formed without dopant in GaAs/AlGaAs heterostructures. *Journal of crystal growth*, 201:159–162, 1999.

[42] G. Snider. Gregory Snider's webpage. https://www3.nd.edu/~gsnider/, 2025. Accessed: 2025-06-09.

[43] O. Göktaş, J. Weber, J. Weis, and K. von Klitzing. Alloyed ohmic contacts to two-dimensional electron system in AlGaAs/GaAs heterostructures down to submicron length scale. *Physica E: Low-dimensional Systems and Nanostructures*, 40(5):1579–1581, 2008.

[44] R.P. Taylor, R. Newbury, A.S. Sachrajda, Y. Feng, P.T. Coleridge, M. Davies, and J.P. McCaffrey. Investigation of the current injection properties of ohmic spikes in nanostructures. *Superlattices and microstructures*, 24(5):337–345, 1998.

[45] E. J. Koop, M. J. Iqbal, F. Limbach, M. Boute, B. J. van Wees, D. Reuter, A. D. Wieck, B. J. Kooi, and C. H. van der Wal. On the annealing mechanism of AuGe Ni Au ohmic contacts to a two dimensional electron gas in GaAs/AlxGa1 xAs heterostructures. *Semiconductor science and technology*, 28(2), 2013.

[46] T. Rudnikov-Keinan, V. Ezersky, N. Maman, S. Mishraki, and Y. Golan. Effect of gaas substrate micropatterning on threading dislocation density in solution-deposited lead sulfide thin films. *ACS applied electronic materials*, 6(6):4159–4166, 2024.

[47] M. J. Martinez, J. Clevenger, IV Austin, F. H., C. T. Sullivan, Gary A. Patrizi, K. Romero, R. P. Timon, P. S. Vigil, and A. J. Grine. Pre-photolithographic GaAs surface treatment for improved photoresist adhesion during wet chemical etching and improved wet etch profiles. *NA*, 2010.

[48] B. Wadja, D. Nawrocki, and L. Rattray. Bi-layer lift-off resist process optimization of insulator film for neural probe fabrication. In *2021 32nd Annual SEMI Advanced Semiconductor Manufacturing Conference (ASMC)*, pages 1–4. IEEE, 2021.

[49] D. J. Chadi and K. J. Chang. Energetics of DX-center formation in GaAs and AlxGa1-x alloys. *Phys. Rev. B*, 39:10063–10074, May 1989.

[50] S. C. Collins. A helium cryostat available to purchase. *Review of Scientific Instruments*, 18(3):157–160, March 1947.

[51] Mahadevappa M. and Peter B. B. The mri helium crisis: Past and future. *Journal of the American College of Radiology*, 13(12):1536–1537, December 2016. Published December 2016; PubMed PMID: 27916113.

[52] D. A. Shea and D. Morgan. The helium-3 shortage: Supply, demand, and options for congress. Technical Report R41419, Congressional Research Service, Library of Congress, Washington, D.C., September 2010. Updated December 22, 2010.

[53] D. J. Cole-Hamilton. Elements of scarcity. *Chemistry International*, 41(4):23–28, October 2019. Published October 31, 2019; CC BY-NC-ND4.0.

[54] Z. Cai, R. H. Clarke, B. A. Glowacki, W. J. Nuttall, and N. Ward. Ongoing ascent to the helium production plateau—insights from system dynamics. *Resources Policy*, 35(2):77–89, June 2010. Published June 2010; available in RePEc :contentReference[oaicite:0]index=0.

[55] K. Allweins, L. Qiu, and G. Thummes. Damping of intrinsic temperature oscillations in a 4 k pulse tube cooler by means of rare earth plates. In *AIP Conference Proceedings*, volume 985, page 109. American Institute of Physics, 2008.

[56] Cryomech Inc. Cryorefrigerator specification sheet: PT403 with CP830, 2013. Accessed: 2025-05-06.

[57] A. DeMann, S. Mueller, and S. B. Field. 1 k cryostat with sub-millikelvin stability based on a pulse-tube cryocooler. *Cryogenics*, 73:60–67, 2016.

[58] Lake Shore Cryotronics, Inc. Nrc-2 superinsulation installation instructions. https://www.lakeshore.com/docs/default-source/product-downloads/installation-instructions/f069-00-00.pdf. Accessed: 2025-05-07.

[59] NASA Commercial Technology Division. Reflective insulation for space and medicine. Technical report, NASA Spinoff, 1992. Describes the development and applications of NRC-2 superinsulation.

[60] D. A. Reay. Superinsulation materials for aerospace cryogenic systems. *Aircraft Engineering and Aerospace Technology*, 73(5):482–487, 2001. Includes discussion of NRC-2 properties and cryogenic applications.

[61] J. R. Smith and M. T. Jones. Super insulation systems for cryogenic test tanks. Technical Report NASA-TN-D-5362, NASA, 1969. Analyzes performance of NRC-2 and similar materials for long-term fluid storage in space.

[62] C. Day. Basics and applications of cryopumps. In *CERN Accelerator School: Vacuum in Accelerators*, CERN, Geneva, Switzerland, 2007. CERN. CAS, Bruges, Belgium, 18–27 June 2007.

[63] attocube systems AG. Cryogenic nanopositioning instruments. https://www.attocube.com/application/files/8716/2810/8696/brochure_nanopositioning-cyrogenic-instruments.pdf. Accessed: 2025-05-07.

[64] M. Hunstig, T. Hemsel, and W. Sextro. Piezoelectric inertia motors—a critical review of history, concepts, design, applications, and perspectives. *Actuators*, 6(1):7, 2017.

[65] J. Siegel, J. Witt, N. Venturi, and S. B. Field. Compact large-range cryogenic scanner. *Review of Scientific Instruments*, 66(3):2520–2523, 1995.

[66] K. H. Kuit, J. R. Kirtley, W. van der Veur, C. G. Molenaar, F. J. G. Roesthuis, A. G. P. Troeman, J. R. Clem, H. Hilgenkamp, H. Rogalla, and J. Flokstra. Vortex trapping and expulsion in thin-film YBa2Cu3O7 delta strips. *Physical review. B, Condensed matter and materials physics*, 77(13), 2008.

[67] G. Stan, S. B. Field, and J. M. Martinis. Critical field for complete vortex expulsion from narrow superconducting strips. *Physical review letters*, 92(9):097003–097003, 2004.

[68] K. Suzuki, Y. Li, T. Utagawa, and K. Tanabe. Magnetic imaging of ndba2cu3oy thin-film patterns with slots. *Applied physics letters*, 76(24):3615–3617, 2000.

[69] N. Kokubo, S. Okayasu, and T. Nojima. Finite-size effect of critical penetration of pearl vortices in narrow superconducting flat rings. *Journal of applied physics*, 125(22), 2019.

[70] S. B. Field, S. S. James, J. Barentine, V. Metlushko, G. Crabtree, H. Shtrikman, B. Ilic, and S. R. J. Brueck. Vortex configurations, matching, and domain structure in large arrays of artificial pinning centers. *Physical Review Letters*, 88(6):067003, 2002.

[71] S. B. Field, J. Witt, F. Nori, and X. Ling. Superconducting vortex avalanches. *Physical Review Letters*, 74(7):1206–1209, 1995.

[72] S. J. Bending. Scanning hall probe microscopy of vortex matter. *Physica C: Superconductivity and its Applications*, 470(19):754–757, October 2010. Received date here; revised date here; accepted date here.

[73] J. Gutierrez, B. Raes, A. V. Silhanek, L. J. Li, N. D. Zhigadlo, J. Karpinski, J. Tempere, and V. V. Moshchalkov. Scanning hall probe microscopy of unconventional vortex patterns in the two-gap MgB2 superconductor. *Physical Review B*, 85(9):094511, March 2012. Received 8 February 2012; published 22 March 2012.

[74] A. M. Chang, H. D. Hallen, L. Harriott, H. F. Hess, H. L. Kao, J. Kwo, R. E. Miller, R. Wolfe, J. van der Ziel, and T. Y. Chang. Scanning hall probe microscopy. *Applied Physics Letters*, 61(16):1974–1976, October 1992. Received 5 June 1992; accepted 18 August 1992.

[75] A. Oral, S. J. Bending, R. G. Humphreys, and M. Henini. Vortex imaging in superconducting films by scanning hall probe microscopy. *Journal of Low Temperature Physics*, 105(5-6):1135–1140, December 1996.

[76] T. Nishio, Q. Chen, W. Gillijns, K. De Keyser, K. Vervaeke, and V. V. Moshchalkov. Scanning hall probe microscopy of vortex patterns in a superconducting microsquare. *Physical Review B*, 77(1):012502, January 2008. Received 22 May 2007; published 23 January 2008.

[77] A.A.B. Brojeny and Clem J. Magnetic-field and current-density distributions in thin-film superconducting rings and disks. *Physical review. B*, 68(17), 2003.

[78] E. H. Brandt and Clem J. Superconducting thin rings with finite penetration depth. *Physical review. B*, 69(18):184509.1–184509.12, 2004.

[79] V. G. Kogan, J. R. Clem, and R. G. Mints. Properties of mesoscopic superconducting thin-film rings. London approach. *Physical Review B*, 69(6):064516, 2003.

[80] B. Abeles, R. Cohen, and G. Cullen. Enhancement of superconductivity in metal films. *Physical Review Letters*, 17:632–634, September 1966.

[81] R. Cohen and B. Abeles. Superconductivity in granular aluminum films. *Physical Review*, 168(2):444–450, 1968.

[82] A. Deshpande, J. Pusskeiler, C. Prange, U. Rogge, M. Dressel, and M. Scheffler. Tuning the superconducting dome in granular aluminum thin films. *Journal of applied physics*, 137(1), 2025.

[83] J. W. Ekin. Critical currents in granular superconductors. *Physical Review B*, 12(7):2676–2685, 1975.

[84] D. Davidovic, S. Kumar, D. Reich, J. Siegel, S. B. Field, R. Tiberio, R. Hey, and K. Ploog. Magnetic correlations, geometrical frustration, and tunable disorder in arrays of superconducting rings. *Physical Review B*, 55(10):6518–6531, 1997.

[85] E. Bronson, M. Gelfand, and S. B. Field. Equilibrium configurations of pearl vortices in narrow strips. *Physical Review B*, 73(14):144501, 2006.

[86] P. M. Morse and H. Feshbach. *Methods of Theoretical Physics*. McGraw-Hill, New York, 1953.

[87] M. Kato, Y. Niwa, and K. Maki. Quasi-particle spectrum around half-quantum vortices (hqvs) in triplet superconductors. *Journal of Physics: Conference Series*, 150(5):052103, 2009.

[88] D.A. Ivanov. Non-abelian statistics of half-quantum vortices in p-wave superconductors. *Physical review letters*, 86(2):268–271, 2001.

[89] S. Das Sarma, M. Freedman, and C. Nayak. Majorana zero modes and topological quantum computation. *npj Quantum Information*, 1:15001, 2015.

[90] C. W. J. Beenakker. Search for majorana fermions in superconductors. *Annual Review of Condensed Matter Physics*, 4:113–136, 2013.

[91] J. Alicea. New directions in the pursuit of majorana fermions in solid state systems. *Reports on Progress in Physics*, 75(7):076501, 2012.

[92] V. Crépel, B. Estienne, and N. Regnault. Variational ansatz for an abelian to non-abelian topological phase transition in v=1/2+1/2 bilayers. *Physical Review Letters*, 123(12):126804, 2019.

[93] M. Sato and Y. Ando. Topological superconductors: a review. *Reports on Progress in Physics*, 80(7):076501, 2017.

[94] S. Das Sarma, M. Freedman, and C. Nayak. Majorana zero modes and topological quantum computation. *npj Quantum Information*, 1:15001, 2015.

[95] C. Nayak, S. H. Simon, A. Stern, M. Freedman, and S. Das Sarma. Non-abelian anyons and topological quantum computation. *Reviews of Modern Physics*, 80(3):1083–1159, 2008.

[96] Yufan L., Xiaoying X., M. H. Lee, M. W. Chu, and C. L. Chien. Observation of half-quantum flux in the unconventional superconductor Bi2Pd. *Science*, 366(6462):238–241, 2019.

[97] P. E. Goa, H. Hauglin, A. A. F. Olsen, D. Shantsev, and T. H. Johansen. Direct observation of the dynamics of magnetic vortices in superconductors by time-resolved magneto-optical imaging. *Superconductor Science and Technology*, 16(5):538–544, 2003.

[98] E. Babaev. Vortices carrying an arbitrary fraction of magnetic flux quantum in two-gap superconductors. *Physical Review Letters*, 89(6):067001, 2002.

[99] V. Vakaryuk and A. J. Leggett. Spin polarization of half-quantum vortices in p-wave superconductors. *Physical Review Letters*, 103(5):057003, 2009.

[100] S. Ran, C. Eckberg, Q. P. Ding, Y. Furukawa, T. Metz, S. R. Saha, I. L. Liu, M. Zic, H. Kim, J. P., and N. P. Butch. Nearly ferromagnetic spin-triplet superconductivity. *Science*, 365(6457):684–689, 2019.

[101] S. Ran, I. L. Liu, Y. S. Eo, D. J. Campbell, P. M. Neves, W. T. Fuhrman, S. R. Saha, C. Eckberg, H. Kim, D. Graf, F. Balakirev, J. Singleton, J. Paglione, and N. P. Butch. Extreme magnetic field-boosted superconductivity. *Nature Physics*, 15(12):1250–1254, 2019.

[102] Y. Tokunaga, H. Sakai, S. Kambe, T. Hattori, N. Higa, G. Nakamine, S. Kitagawa, K. Ishida, A. Nakamura, D. Aoki, Y. Homma, Y. Shimizu, and Y. J. Sato. ^{125}Te-NMR study on a single crystal of heavy fermion superconductor UTe2. *Journal of the Physical Society of Japan*, 88(7):073701, 2019.

[103] D. Aoki, A. Nakamura, F. Honda, D. X. Li, Y. Homma, Y. Shimizu, Y. J. Sato, G. Knebel, J. P. Brison, and J. Flouquet. Unconventional superconductivity in heavy fermion UTe2. *Journal of the Physical Society of Japan*, 88(4):043702, 2019.

[104] S. M. Thomas, E. D. Bauer, F. Ronning, J. D. Thompson, G. Drachuck, K. Chen, J. Singleton, D. Aoki, G. Knebel, and J. Flouquet. Superconducting phase of UTe2 single crystals grown by the chemical vapor transport method. *Physical Review B*, 101(13):134521, 2020.

[105] Z. Li, C. M. Moir, S. M. Thomas, F. Ronning, Eric D. Bauer, D. Aoki, J. Ishizuka, M. Sigrist, D. F. Agterberg, T. Shibauchi, Y. Matsuda, A. P. Mackenzie, and K. A. Moler. Observation of odd-parity superconductivity in UTe2. *Science*, 371(6527):716–721, 2021.

[106] Y. Iguchi, H. Man, S. M. Thomas, F. Ronning, J. Ishizuka, M. Sigrist, P. F. S. Rosa, and K. A. Moler. Magnetic edge fields in UTe2 near zero background fields. *Physical Review B*, 110(21):214505, December 2024.

[107] X. Lu, Y. Huang, Y. Wang, P. F. S. Rosa, J. D. Thompson, and F. Ronning. Probing p-wave superconductivity in UTe_2 via point-contact junctions. *npj Quantum Materials*, 6(1):57, 2021.

[108] K. Yosida. Paramagnetic susceptibility in superconductors. *Physical Review*, 110(4):769–770, 1958.

[109] H. Matsumura, H. Fujibayashi, K. Kinjo, S. Kitagawa, K. Ishida, Y. Tokunaga, et al. Large reduction in the a-axis knight shift on UTe2 with Tc = 2.1 k. *Physical Review Letters*, 130(20):207001, May 2023.

[110] G. Nakamine, K. Kinjo, S. Kitagawa, K. Ishida, Y. Tokunaga, H. Sakai, S. Kambe, A. Nakamura, Y. Shimizu, et al. Anisotropic response of spin susceptibility in the superconducting state of UTe2 probed with ^{125}Te NMR measurement. *Journal of the Physical Society of Japan*, 90(7):073703, 2021.

[111] A. P. Mackenzie and Y. Maeno. The superconductivity of Sr2RuO4 and the physics of spin-triplet pairing. *Reviews of Modern Physics*, 75(2):657–712, 2003.

[112] K. I. Wysokiński, G. Litak, J. F. Annett, and B. L. Györffy. Spin triplet superconductivity in Sr2RuO4. *Philosophical Magazine*, 84(9):1017–1025, 2004.

[113] Kazushi K., Shingo Y., Y. Maeno, and T. Sakakibara. Searching for spin-triplet superconductivity in Sr2RuO4. *Journal of the Physical Society of Japan*, 87(9):093703, 2018.

[114] G. Knebel, W. Knafo, A. Pourret, Q. Niu, M. Vališka, D. Braithwaite, G. Lapertot, M. Nardone, A. Zitouni, S. Mishra, I. Sheikin, G. Seyfarth, J.-P. Brison, D. Aoki, and J. Flouquet. Field-reentrant superconductivity and hidden magnetism in UTe2. *Journal of the Physical Society of Japan*, 88(6):063707, 2019.

[115] A. M. Clogston. Upper limit for the critical field in hard superconductors. *Physical Review Letters*, 9(6):266–267, 1962.

[116] S. M. Anlage. *Microwave Superconductivity*. Springer, Cham, 2021.

[117] D. V. Shantsev, Y. M. Galperin, and T. H. Johansen. Scaling and exact solutions for the flux creep problem in a slab superconductor. *Physical Review B*, 65(18):184512, 2002.

[118] S. Sundar, M.K. Chattopadhyay, L.S. Chandra, and S.B. Roy. High-field paramagnetic meissner effect in MoRe alloys. *Journal of Superconductivity and Novel Magnetism*, 31(2):269–274, 2018.

[119] S. Fava, G. De Vecchi, G. Jotzu, et al. Magnetic field expulsion in optically driven YBa2Cu3O6. *Nature*, 601:123–126, 2024.

[120] W. A. Little and R. D. Parks. Observation of quantum periodicity in the transition temperature of a superconducting cylinder. *Physical Review Letters*, 9(1):9–12, 1962.

[121] W. Brenig. Comment on the quantization of magnetic flux in superconductors. *Physical Review Letters*, 7(9):337–337, 1961.

[122] N. Byers and C. N. Yang. Theoretical considerations concerning quantized magnetic flux in superconducting cylinders. *Physical Review Letters*, 7(2):46–49, 1961.

[123] S. Ran, I. L. Liu, P. Saraf, J. P. N. Paglione, and N. P. Butch. Comparison of two different synthesis methods of single crystals of superconducting uranium ditelluride. *Journal of Visualized Experiments*, 173:e62563, 2021.

[124] S. Yao, T. Li, C. Yue, X. Xu, B. Zhang, and C. Zhang. Controllable growth of centimetre-sized UTe2 single crystals by the chemical vapor transport method. *CrystEngComm*, 24:6262–6268, 2022.

[125] N. Li, Z. Chen, T. Li, C. Zhang, and B. B. Zhang. Superconducting phase UTe2 single crystals grown by the chemistry vapor transport method. *Crystal Growth & Design*, 25(3):833–837, 2025.

[126] H. Yoon, Y. S. Eo, J. Park, J. A. Horn, R. G. Dorman, S. R. Saha, Ian M. Hayes, I. Takeuchi, P. M. R. Brydon, and J. P. Paglione. Probing p-wave superconductivity in UTe2 via point-contact junctions. *npj Quantum Materials*, 9:91, 2024.

[127] I. Sutherland, E. Sheng, R.H. Bradley, and P.K. Freakley. Effects of ozone oxidation on carbon black surfaces. *Journal of Materials Science*, 31(21):5651–5655, 1996.

[128] Y. Wei, Y. Hu, P. Da, Z. Weng, P. Xi, and C. Yan. Triggered lattice-oxygen oxidation with active-site generation and self-termination of surface reconstruction during water oxidation. *Proceedings of the National Academy of Sciences*, 120(50):e2312224120, 2023.

[129] H. Joress, S. C. Barron, K. J. T. Livi, N. Aronhime, and T. P. Weihs. Self-sustaining oxidation initiated by rapid formation reactions in multilayer foils. *Applied Physics Letters*, 101(11):114102, 2012.

[130] K. Thürmer, E. D. Williams, and J. Reutt-Robey. Autocatalytic oxidation of lead crystallite surfaces. *Science*, 297(5589):2033–2035, 2002.

[131] Z. Du, Y. Lyu, S. Ran, T. Metz, S. R. Saha, N. P. Butch, and J. C. S. Davis. Detection of a pair density wave state in UTe2. *Nature*, 621:505–510, 2023.

[132] C. Riedl, B. Such, and A. Schwarz. Cleaving ionic crystals under uhv: A compact in situ cleaver for atomically defined surfaces. *Review of Scientific Instruments*, 93(5):053705, 2022.

[133] T. K. Das, F. Tassinari, R. Naaman, and J. Fransson. Temperature-dependent chiral-induced spin selectivity effect: Experiments and theory. *Journal of physical chemistry. C*, 126(6):3257–3264, 2022.

[134] R. Naaman, Y. Paltiel, and D. H. Waldeck. Chirality and spin: A new perspective on spintronics. *The Journal of Physical Chemistry Letters*, 11(9):3660–3666, 2020.

[135] V. Varade, T. Z. Markus, K. Vankayala, N. Friedman, M. Sheves, D. H. Waldeck, and R. Naaman. Bacteriorhodopsin based non-magnetic spin filters for biomolecular spintronics. *Physical Chemistry Chemical Physics*, 20(2):1091–1097, 2017.

[136] K. Michaeli, N. Kantor-Uriel, R. Naaman, and D. H. Waldeck. The electron's spin and molecular chirality—how are they related and how do they affect life processes? *Chemical Society Reviews*, 45(23):6478–6487, 2016.

[137] R. Naaman and D. H. Waldeck. Spintronics and chirality: Spin selectivity in electron transport through chiral molecules. *Annual Review of Physical Chemistry*, 66:263–281, 2015.

[138] R. Naaman and David H. Waldeck. Chiral-Induced Spin Selectivity Effect. *The Journal of Physical Chemistry Letters*, 3(16):2178–2187, 2012.

[139] M. Geyer, R. Gutierrez, and G. Cuniberti. Effective hamiltonian model for helically constrained quantum systems within adiabatic perturbation theory: Application to the chirality-induced spin selectivity (CISS) effect. *The Journal of Chemical Physics*, 158(20):204101, 2023.

[140] K. H. Huisman and J. M. Thijssen. CISS effect: A magnetoresistance through inelastic scattering. *Journal of Physical Chemistry C*, 125(42):23364–23369, 2021.

[141] M. S. Zöllner, S. Varela, E. Medina, V. Mujica, and C. Herrmann. Insight into the origin of chiral-induced spin selectivity from a symmetry analysis of electronic transmission. *Journal of Chemical Theory and Computation*, 16(5):2914–2929, 2020.

[142] Y. Liu, J. Xiao, J. Koo, and B. Yan. Chirality-driven topological electronic structure of dna-like materials. *Nature Materials*, 2021. Published online.

[143] L. H. Thomas. The motion of the spinning electron. *Nature (London)*, 117(2945):514–514, 1926.

[144] S. Yeganeh, M. A. Ratner, E. Medina, and V. Mujica. Chiral electron transport: Scattering through helical potentials. *The Journal of Chemical Physics*, 131(1):014707, July 2009.

[145] R. Gutierrez, E. Díaz, R. Naaman, and G. Cuniberti. Spin-selective transport through helical molecular systems. *Physical Review B*, 85(8):081404, 2012.

[146] E. Medina, F. López, Mark A. Ratner, and V. Mujica. Chiral molecular films as electron polarizers and polarization modulators. *Europhysics Letters*, 99(1):17006, 2012.

[147] W. H Pirkle. The nonequivalence of physical properties of enantiomers in optically active solvents. differences in nuclear magnetic resonance spectra. i. *Journal of the American Chemical Society*, 88(8):1837–1837, 1966.

[148] T. P. Yoon and E. N. Jacobsen. Privileged chiral catalysts. *Science*, 299(5613):1691–1693, 2003.

[149] E. N. Jacobsen, A. Pfaltz, and H. Yamamoto, editors. *Comprehensive Asymmetric Catalysis*. Springer, Berlin, Germany, 1999.

[150] I. Ojima, editor. *Catalytic Asymmetric Synthesis*. Wiley, New York, 2nd edition, 2000.

[151] D. M. Campbell and P. S. Farago. Electron optic dichroism in camphor. *Journal of Physics B: Atomic and Molecular Physics*, 20(19):5133, 1999.

[152] C. Nolting, S. Mayer, and J. Kessler. Electron dichroism - new data and an experimental cross-check. *Journal of Physics B: Atomic, Molecular and Optical Physics*, 30(23):5491, 1997.

[153] Z. Xie, T. Z. Markus, S. R. Cohen, Z. Vager, R. Gutierrez, and R. Naaman. Spin specific electron conduction through DNA oligomers. *Nano Letters*, 11(11):4652–4655, 2011.

[154] B. Göhler, V. Hamelbeck, T. Z. Markus, M. Kettner, G. F. Hanne, Z. Vager, R. Naaman, and H. Zacharias. Spin selectivity in electron transmission through self-assembled monolayers of double-stranded dna. *Science*, 331(6019):894–897, 2011.

[155] D. Mishra, P. C. Mondal, S. Pal, T. K. Das, V. Kiran, S. R. Cohen, Y. Mastai, R. Naaman, and G. Haran. Spin-dependent electron transmission through bacteriorhodopsin embedded in purple membrane. *Proceedings of the National Academy of Sciences*, 110(37):14872–14876, 2013.

[156] R. Gupta, A. Balo, R. Garg, A. K. Mondal, K. B. Ghosh, and P. Chandra Mondal. The chirality-induced spin selectivity effect in asymmetric spin transport: from solution to device applications. *Chemical science (Cambridge)*, 15(45):18751–18771, 2024.

[157] A. Inui, R. Aoki, Y. Nishiue, K. Shiota, Y. Kousaka, H. Shishido, D. Hirobe, M. Suda, J. I. Ohe, J. I. Kishine, H. M. Yamamoto, and Y. Togawa. Chirality-Induced Spin-Polarized State of a Chiral Crystal CrNb3S6. *Physical Review Letters*, 124(16):166602, 2020.

[158] M. I. Dyakonov and V. I. Perel. Possibility of orienting electron spins with current. *Soviet Journal of Experimental and Theoretical Physics Letters*, 13:467, 1971.

[159] T. Kimura, Y. Otani, T. Sato, S. Takahashi, and S. Maekawa. Room-temperature reversible spin hall effect. *Physical Review Letters*, 98(15):156601, 2007.

[160] S. O. Valenzuela and M. Tinkham. Direct electronic measurement of the spin hall effect. *Nature*, 442:176–179, 2006.

[161] E. Saitoh, M. Ueda, H. Miyajima, and G. Tatara. Conversion of spin current into charge current at room temperature: Inverse spin-hall effect. *Applied Physics Letters*, 88(18):182509, 2006.

[162] Ryuya Aoki, Yusuke Kousaka, and Yoshihiko Togawa. Anomalous Nonreciprocal Electrical Transport on Chiral Magnetic Order. *Physical Review Letters*, 122(5):057206, 2019.

[163] A. B. Pippard. *Magnetoresistance in Metals*. Cambridge University Press, Cambridge, 1989.

[164] K. Shiota, A. Inui, Y. Hosaka, R. Amano, Y. Ōnuki, M. Hedo, T. Nakama, D. Hirobe, J. I. Ohe, J. I. Kishine, H. M. Yamamoto, H. Shishido, and Y. Togawa. Chirality-induced spin polarization over macroscopic distances in chiral disilicide crystals. *Physical Review Letters*, 127(12):126602, 2021.

[165] P. Huang, Z. Xia, X. Gao, J. M. Rondinelli, X. Zhang, H. Zhang, K. R. Poeppelmeier, and A. Zunger. Ferri-chiral compounds with potentially switchable Dresselhaus spin splitting. *Physical Review B*, 102(23):235127, 2020.

[166] M. Todeschini, A. Bastos da Silva Fanta, F. Jensen, J. B. Wagner, and A. Han. Influence of ti and cr adhesion layers on ultrathin au films. *ACS Applied Materials & Interfaces*, 9(42):37374–37385, 2017.

[167] P. R. Munroe. The application of focused ion beam microscopy in the material sciences. *Materials Characterization*, 60(1), 01 2009.